JETP Letters, Vol. 82, No. 1, 2005, pp. 1–6. From Pis'ma v Zhurnal Éksperimental'noĭ i Teoreticheskoĭ Fiziki, Vol. 82, No. 1, 2005, pp. 3–7.

Singlet $VA\tilde{V}$ Correlator within the Instanton Vacuum Model¶

A. E. Dorokhov

Bogoliubov Laboratory of Theoretical Physics, Joint Institute for Nuclear Research, Dubna, Moscow region, 141980 Russia

Received May 30, 2005

The correlator of singlet axial-vector and vector currents in the external electromagnetic field is studied within the instanton liquid model of the QCD vacuum. In the chiral limit, we calculate the longitudinal $w_L^{(0)}$ and transversal $w_T^{(0)}$, with respect to the axial-vector index, invariant amplitudes at an arbitrary spacelike momentum transfer q. It is demonstrated how the anomalous longitudinal part of the correlator is renormalized at low momenta due to the presence of the $U_A(1)$ anomaly. © *2005 Pleiades Publishing, Inc.*

PACS numbers: 12.38.–t

1. INTRODUCTION

Consideration of the axial-vector A and vector V current–current correlator in the soft external electromagnetic field $\tilde{V}$ is an important part of the calculations of the complicated light-by-light scattering amplitude related to the problem of accurate computation of higher-order hadronic contributions to the muon anomalous magnetic moment.[1] In this specific kinematics, when one photon (V) with momentum $q_2 \equiv q$ is virtual and another one ($\tilde{V}$) with momentum q_1 represents the external electromagnetic field and can be regarded as a real photon with the vanishingly small momentum q_1, only two invariant functions survive in linear form in small q_1 approximation. It is convenient to parametrize the $VA\tilde{V}$ correlator (Fig. 1) in terms of longitudinal w_L and transversal w_T (with respect to the axial current index) Lorentz invariant amplitudes:

$$\tilde{T}_{\mu\nu\lambda}(q_1, q_2) = \frac{1}{4\pi^2}[w_T(q^2)(q_2^2 q_1^\rho \varepsilon_{\rho\mu\nu\lambda} - q_2^\nu q_1^\rho q_2^\sigma \varepsilon_{\rho\mu\sigma\lambda} + q_2^\lambda q_1^\rho q_2^\sigma \varepsilon_{\rho\mu\sigma\nu}) - w_L(q^2) q_2^\lambda q_1^\rho q_2^\sigma \varepsilon_{\rho\mu\sigma\nu}]. \quad (1)$$

Both Lorentz structures are transversal with respect to vector current; $q_2^\nu \tilde{T}_{\mu\nu\lambda} = 0$. As for the axial current, the first structure is transversal with respect to q_2^λ, while the second one is longitudinal and, thus, anomalous. The appearance of the longitudinal structure is a consequence of the Adler–Bell–Jackiw axial anomaly [3, 4].

For the nonsinglet axial current $A^{(3)}$, there are no perturbative [5] and nonperturbative [6] corrections to the axial anomaly and, as consequence, the invariant function $w_L^{(3)}$ remains intact when interaction with gluons is taken into account. It was shown in [7] that, in the nonsinglet channel, the transversal structure $w_T^{(3)}$ is also free from perturbative corrections. Nonperturbative nonrenormalization of the nonsinglet longitudinal part follows from the 't Hooft consistency condition [6], i.e., the exact quark–hadron duality realized as a correspondence between the infrared singularity of the quark triangle and the massless pion pole in terms of hadrons. However, for the singlet axial current $A^{(0)}$ due to the gluonic $U_A(1)$ anomaly, there is no massless state even in the chiral limit. Instead, the massive η' meson appears. So, one expects nonperturbative renormalization of the singlet anomalous amplitude $w_L^{(0)}$ at momenta below η' mass.

In [8], in the framework of the instanton liquid model [9], we have analyzed the nonperturbative prop-

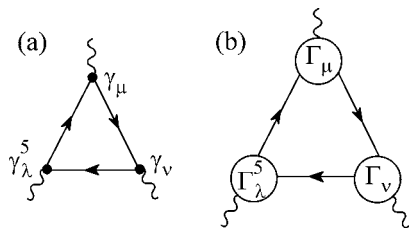

Fig. 1. Diagrammatic representation of the triangle diagram in the local perturbative theory (a) and in the instanton model with dressed quark lines and full quark-current vertices (b).

¶ This article was submitted by the author in English.

[1] See, e.g., [1, 2] and references therein.

0021-3640/05/8201-0001$26.00 © 2005 Pleiades Publishing, Inc.

erties of the nonsinglet triangle diagram in the kinematics specified above. We demonstrated how the anomalous structure $w_L^{(3)}$ is saturated within the instanton liquid model. We also calculated the transversal invariant function $w_T^{(3)}$ at arbitrary spacelike q and showed that, within the instanton model at large q^2, there are no power corrections to this structure. The nonperturbative corrections to $w_T^{(3)}$ at large q^2 have exponentially decreasing behavior related to the short-distance properties of the instanton nonlocality in the QCD vacuum.

The present work is devoted to the study of the $U_A(1)$ anomaly effect on the singlet $VA\tilde{V}$ correlator within the instanton liquid model. We calculate, in the chiral limit, the longitudinal $w_L^{(0)}$ and transversal $w_T^{(0)}$ invariant functions at an arbitrary spacelike momentum transfer q and demonstrate how the singlet anomalous part of the correlator $w_L^{(0)}$ is renormalized at low momenta due to presence of the $U_A(1)$ anomaly.

2. THE STRUCTURE OF THE $VA\tilde{V}$ CORRELATOR IN PERTURBATIVE APPROACH

The amplitude for the triangle diagram can be written as a correlator of the axial current j_λ^5 and two vector currents j_ν and $\tilde{j}_\mu$ (Fig. 1):

$$\tilde{T}_{\mu\nu\lambda} = -\int d^4x d^4y e^{iqx-iky}\langle 0|T\{j_\nu(x)\tilde{j}_\mu(y)j_\lambda^5(0)\}|0\rangle, \quad (2)$$

where, for light u and d quarks, one has, in the local theory,

$$j_\mu = \bar{q}\gamma_\mu V q, \quad j_\lambda^5 = \bar{q}\gamma_\lambda\gamma_5 A q,$$

the quark field q_f^i has color (i) and flavor (f) indices; $A^{(0)} = I, A^{(3)} = \tau_3$ are the flavor matrices of the axial current; and $V = \tilde{V} = \frac{1}{2}\left(\frac{1}{3} + \tau_3\right)$ are the charge matrices, with the tilted current being for the soft momentum photon vertex.

In the local perturbative theory, the one-loop result (Fig. 1a) for the invariant functions w_T and w_L for spacelike momenta $q(q^2 \geq 0)$ is

$$\begin{aligned} w_L^{1-\text{loop}} &= 2w_T^{1-\text{loop}} \\ &= 2N_c\mathrm{Tr}(AV\tilde{V})\int_0^1 \frac{d\alpha\alpha(1-\alpha)}{\alpha(1-\alpha)q^2 + m_f^2}, \end{aligned} \quad (3)$$

where N_c is the color number, and, for light quark masses, one takes $m_f \equiv m_u \approx m_d$. In the chiral limit, $m_f = 0$, one gets the result

$$w_L(q^2) = 2w_T(q^2) = \frac{2N_c}{q^2}\mathrm{Tr}(AV\tilde{V}). \quad (4)$$

3. THE INSTANTON EFFECTIVE QUARK MODEL

To study nonperturbative effects in the triangle amplitude $\tilde{T}_{\mu\nu\lambda}$ at low and intermediate momenta, one can use the framework of the effective approach based on the representation of the QCD vacuum as an ensemble of strong vacuum fluctuations of a gluon field, namely, instantons. Spontaneous breaking of the chiral symmetry and dynamical generation of a momentum-dependent quark mass are naturally explained within the instanton liquid model. The instanton fluctuations characterize the nonlocal properties of the QCD vacuum [10–12]. The interaction of light u and d quarks in the instanton vacuum can be described in terms of the effective 't Hooft four-quark action with a nonlocal kernel induced by quark zero modes in the instanton field. The gauged version of the model [13–15] meets the symmetry properties with respect to external gauge fields, and the corresponding vertices satisfy the Ward–Takahashi identities.

In the framework of this effective model, the nonsinglet V and A current–current correlators, the vector Adler function, and the pion transition form factor have been calculated for arbitrary current virtualities in [15–17]. In the same model, the topological susceptibility of the QCD vacuum, which is reduced to the singlet A current–current correlator, has been considered in [15, 18].

The spin–flavor structure of the nonlocal chirally invariant interaction of soft quarks is given by the matrix products[2]

$$\begin{aligned} &G(1\otimes 1 + i\gamma_5\tau^a \otimes i\gamma_5\tau^a), \\ &G'(\tau^a\otimes\tau^a + i\gamma_5\otimes i\gamma_5), \end{aligned} \quad (5)$$

where G and G' are the four-quark couplings in the isotriplet and singlet channels. For the interaction in the form of the 't Hooft determinant, one has the relation $G' = -G$. In general, due to repulsion in the singlet channel, the relation $G' < G$ is required.

Within the gauged instanton model, the dressed quark propagator in the chiral limit, $S(p)$, is defined as

$$S^{-1}(p) = i\hat{p} - M(p^2), \quad (6)$$

with the momentum-dependent quark mass

$$M(p^2) = M_q f^2(p^2) \quad (7)$$

found as the solution of the gap equation

$$M(p^2) = 4G_P N_f N_c f^2(p^2)\int \frac{d^4k}{(2\pi)^4} f^2(k^2)\frac{M(k^2)}{D(k^2)}, \quad (8)$$

where we denote

$$D(k^2) = k^2 + M^2(k^2).$$

[2] The explicit calculations below are performed in $SU_f(2)$ sector of the model.

The constant $M_q \equiv M(0)$ in (7) is determined dynamically from Eq. (8), and the function $f(p)$ defines the nonlocal kernel of the four-quark interaction. Within the instanton model, $f(p)$ describing the momentum distribution of quarks in the nonperturbative QCD vacuum is expressed through the quark zero-mode function. It is implied in [8, 11, 12] that the quark zero mode in the instanton field is taken in the axial gauge when the gauge-dependent dynamical quark mass is defined. In particular, it means that $f(p)$ for large arguments decreases like some exponential in p^2. To make the numerics simpler, we shall use the Gaussian form

$$f(p) = \exp(-p^2/\Lambda^2), \tag{9}$$

where the parameter Λ characterizes the size of nonlocal fluctuations in the QCD vacuum, and it is proportional to the inverse average size of an instanton.

The conserved vector vertex following from the instanton model is [14, 15] (Fig. 2a)

$$\Gamma_\mu(k, k') = \gamma_\mu + (k + k')_\mu M^{(1)}(k, k'), \tag{10}$$

where $M^{(1)}(k, k')$ is the finite-difference derivative of the dynamical quark mass, q is the momentum corresponding to the current, and k (k') is the incoming (outgoing) momentum of the quark: $k' = k + q$. The finite-difference derivative of an arbitrary function F is defined as

$$F^{(1)}(k, k') = \frac{F(k') - F(k)}{k'^2 - k^2}. \tag{11}$$

The nonlocal part of vertex (10) necessarily appears in order to fit the vector Ward–Takahashi identity.

Within the chiral quark model [14] based on the nonlocal structure of the instanton vacuum [11], the full singlet axial-vector vertex, including local and nonlocal pieces, is given by [15]

$$\Gamma_\mu^{5(0)}(k, k')$$

$$= \gamma_\mu\gamma_5 + \gamma_5(k + k')_\mu M_q \frac{(f(k') - f(k))^2}{k'^2 - k^2} \tag{12}$$

$$+ \gamma_5 \frac{q_\mu}{q^2} 2M_q f(k') f(k) \frac{G'}{G} \frac{1 - GJ_{PP}(q^2)}{1 - G'J_{PP}(q^2)},$$

where

$$J_{PP}(q^2) = \frac{8N_c}{M_q^2} \int \frac{d^4k}{(2\pi)^4} \frac{M_+M_-(k_+k_- + M_+M_-)}{D_+D_-}. \tag{13}$$

Here and below, we use the notations

$$k_+ = k, \quad k_- = k - q, \quad k_\perp^2 = k_+k_- - \frac{(k_+q)(k_-q)}{q^2},$$

$$M_\pm = M(k_\pm^2), \quad D_\pm = D(k_\pm^2), \quad f_\pm = f(k_\pm^2).$$

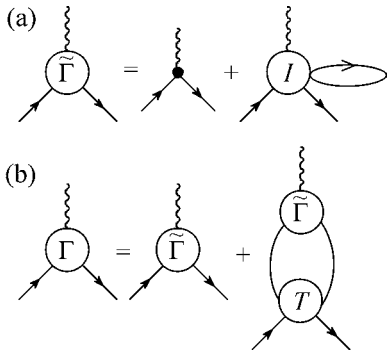

Fig. 2. Diagrammatic representation of the bare (a) and full (b) quark-current vertices.

Vertex (12) takes into account the quark–antiquark rescattering in the singlet axial channel (Fig. 2b). For completeness, we also present the vertex corresponding to the conserved isotriplet axial-vector current, which, in the chiral limit, is given by [14]

$$\Gamma_\mu^{5(3)}(k, k') = \tau_3 \Big[\gamma_\mu\gamma_5 + 2\gamma_5 \frac{q_\mu}{q^2} M_q f(k) f(k') + \gamma_5(k + k')_\mu M_q \frac{(f(k') - f(k))^2}{k'^2 - k^2} \Big]. \tag{14}$$

The isotriplet axial-vector vertex has a massless pole, $q^2 = 0$, that follows from the spontaneous breaking of the chiral symmetry in the limit of massless u and d quarks. Evidently, this pole corresponds to the massless Goldstone pion.

Singlet current (12) does not contain a massless pole due to the presence of the $U_A(1)$ anomaly. Indeed, as $q^2 \longrightarrow 0$, there is compensation between the denominator and numerator in (12):

$$\frac{1 - GJ_{PP}(q^2)}{-q^2} = G\frac{f_\pi^2}{M_q^2} \text{ as } q^2 \longrightarrow 0, \tag{15}$$

where f_π is the pion weak-decay constant. In cancellation of the massless pole, the gap equation is used. Instead, the singlet current develops a pole at the η'-meson mass:[3]

$$1 - G'J_{PP}(q^2 = -m_{\eta'}^2) = 0, \tag{16}$$

thus solving the $U_A(1)$ problem. Let us also remember that, in the instanton chiral quark model, the connection between the soft gluon and effective quark degrees of freedom is fixed by the gap equation. In particular, this means that the four-quark couplings G (G') are proportional to the gluon condensate.

[3] See previous footnote. Also, we neglect the effect of the axial–pseudoscalar mixing with the longitudinal component of the flavor singlet f_1 meson.

4. SINGLET $VA\tilde{V}$ CORRELATOR

In the effective instantonlike model, the nondiagonal correlator of vector current and singlet axial-vector current in the external electromagnetic field ($VA\tilde{V}$) is given by (Fig. 1b)

$$\tilde{T}_{\mu\nu\lambda}(q_1, q_2) = -2N_c \mathrm{Tr}(AV\tilde{V}) \int \frac{d^4k}{(2\pi)^4}$$

$$\times \mathrm{Tr}[\Gamma_\mu(k+q_1, k) S(k+q_1) \Gamma_\lambda^{5(0)}(k+q_1, k-q_2) \quad (17)$$

$$\times S(k-q_2) \Gamma_\nu(k, k-q_2) S(k)],$$

where the quark propagator, the vector, and the axial-vector vertices are defined by (6), (10), and (12), respectively. The structure of vector vertex (10) guarantees that the amplitude is transversal with respect to vector indices

$$\tilde{T}_{\mu\nu\lambda}(q_1, q_2) q_1^\mu = \tilde{T}_{\mu\nu\lambda}(q_1, q_2) q_2^\nu = 0$$

and the Lorentz structure of the amplitude is given by (1).

In [8], we found, for the nonsinglet axial current $\Gamma_\lambda^{5(3)}$, the expressions for the longitudinal amplitude,

$$w_L^{(3)}(q^2) = \frac{2N_c}{3} \frac{1}{q^2}, \quad (18)$$

and for the combination of invariant functions that shows up in the nonperturbative dynamics:

$$w_{LT}^{(3)}(q^2) \equiv w_L^{(3)}(q^2) - 2w_T^{(3)}(q^2)$$

$$= \frac{4N_c}{3q^2} \int \frac{d^4k}{\pi^2} \frac{\sqrt{M_-}}{D_+^2 D_-}$$

$$\times \left\{ \sqrt{M_-} \left[M_+ - \frac{2}{3} M_+' \left(k^2 + 2\frac{(kq)^2}{q^2} \right) \right] \right. \quad (19)$$

$$- \frac{4}{3} k_\perp^2 [\sqrt{M_+} M^{(1)}(k_+, k_-)$$

$$\left. - 2(kq) M_+' \sqrt{M}^{(1)}(k_+, k_-)] \right\},$$

where the prime means a derivative with respect to k^2: $M'(k^2) = dM(k^2)/dk^2$. Result (18), which is independent of the details of the nonlocal effective model, is in agreement with the statement about the absence of nonperturbative corrections to the nonsinglet longitudinal invariant function that follows from the 't Hooft duality arguments.

The calculations of the singlet $VA\tilde{V}$ correlator results in the following modification of the nonsinglet amplitudes:

$$w_L^{(0)}(q^2) = \frac{5}{3} w_L^{(3)}(q^2) + \Delta w^{(0)}(q^2), \quad (20)$$

$$w_{LT}^{(0)}(q^2) = \frac{5}{3} w_{LT}^{(3)}(q^2) + \Delta w^{(0)}(q^2), \quad (21)$$

where

$$\Delta w^{(0)}(q^2) = -\frac{5N_c}{9q^2} \frac{1 - G'/G}{1 - G' J_{PP}(q^2)} \int \frac{d^4k}{\pi^4} \frac{\sqrt{M_+ M_-}}{D_+^2 D_-}$$

$$\times \left[M_+ - \frac{4}{3} M_+' k_\perp^2 - M^{(1)}(k_+, k_-) \right. \quad (22)$$

$$\left. \times \left(\frac{4}{3} \frac{(kq)^2}{q^2} + \frac{2}{3} k^2 - (kq) \right) \right].$$

In [8], it was shown that, in the chiral limit, the nonsinglet transversal amplitude gets only exponentially suppressed at large momenta corrections. The reason is that the asymptotics of amplitude (19) is proportional to the vacuum nonlocality function $f(q)$; that is, it necessarily has exponentially decreasing asymptotics. The singlet amplitudes differ from the nonsinglet ones by term (22), which also has exponentially suppressed large q^2 asymptotics. Thus, within the instanton model, the singlet longitudinal and transversal parts have only corrections that are exponentially suppressed at large q^2, and all of the power corrections allowed by the operator product expansion cancel each other.

Figure 3 illustrates how the singlet longitudinal amplitude $w_L^{(0)}$ is renormalized at low momenta by the presence of the $U_A(1)$ anomaly. The behavior of $w_{LT}^{(0)}(q^2)$ is presented in Fig. 4. In both figures, the corresponding results for the nonsinglet case are also shown. The values of the model parameters used in the calculations were fixed earlier in [8, 16] as

$$M_q = 0.24 \text{ GeV},$$
$$\Lambda_P = 1.11 \text{ GeV}, \quad G_P = 27.4 \text{ GeV}^{-2}. \quad (23)$$

The coupling G' is fixed by fitting the meson spectrum. Approximately, one has $G' \approx 0.1G$ [13]. We also find numerical values of the invariant amplitudes at zero virtuality:

$$w_L^{(0)}(q^2 = 0) = 4.4 \text{ GeV}^{-2},$$
$$w_{LT}^{(0)}(q^2 = 0) = 0.6 \text{ GeV}^{-2}. \quad (24)$$

The precise form and even the sign of $w_{LT}^{(0)}(q^2)$ strongly depend on the ratio of couplings G'/G and have to be

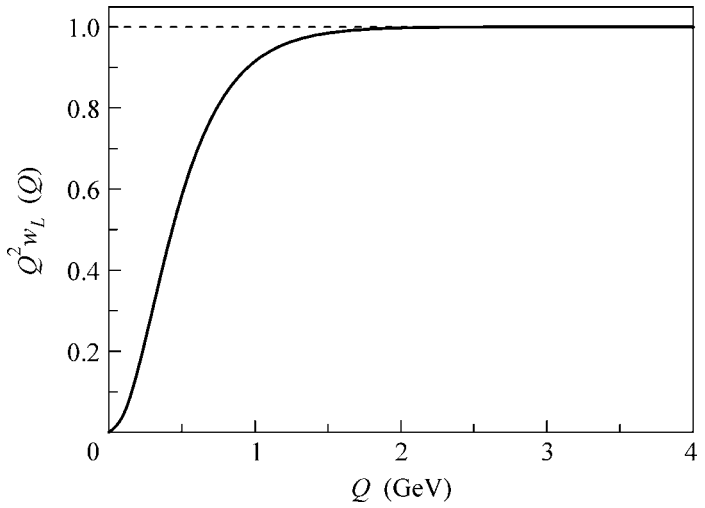

Fig. 3. Normalized w_L invariant function in the singlet case (solid line) and nonsinglet case (dashed line).

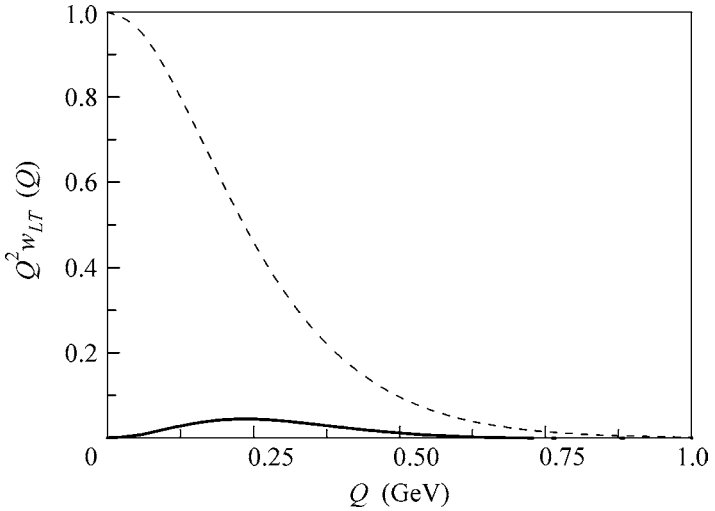

Fig. 4. Normalized w_{LT} invariant function versus Q predicted by the instanton model in the singlet case (solid line) and isotriplet case (dashed line).

defined in the calculations with a more realistic choice of model parameters.

5. CONCLUSIONS

In the framework of the instanton liquid model, we have calculated, for arbitrary momenta transfers, the nondiagonal correlator of the singlet axial-vector and vector currents in the background of a soft vector field. For this specific kinematics, we find that, in the chiral limit, the large momenta power corrections are absent for both longitudinal w_L and transversal w_T invariant amplitudes. These amplitudes have very similar behavior and are corrected only by exponentially small terms, which reflect the nonlocal structure of the QCD vacuum.

Within the instanton model, the renormalization of the singlet longitudinal $w_L^{(0)}$ amplitude occurring at low momenta due to the $U_A(1)$ anomaly is explicitly demonstrated. In the nonsinglet case, the behavior of w_L and w_T at low momenta is very different due to the contribution of the massless pion state. At the same time, in the singlet case, there is no massless state and the deflection of w_L from $2w_T$ amplitudes is rather small.

I am grateful to A.P. Bakulev, N.I. Kochelev, P. Kroll, S.V. Mikhailov, A.A. Pivovarov, and O.V. Teryaev for helpful discussions on the subject of the present work.

This work was supported in part by the Russian Foundation for Basic Research (project nos. 03-02-17291 and 04-02-16445) and the Heisenberg–Landau program.

REFERENCES

1. S. Groote, J. G. Körner, and A. A. Pivovarov, Eur. Phys. J. C **24**, 393 (2002).
2. A. Czarnecki, W. J. Marciano, and A. Vainshtein, Phys. Rev. D **67**, 073006 (2003).
3. S. L. Adler, Phys. Rev. **177**, 2426 (1969).
4. J. S. Bell and R. Jackiw, Nuovo Cimento A **60**, 47 (1969).
5. S. L. Adler and W. A. Bardeen, Phys. Rev. **182**, 1517 (1969).
6. G. 't Hooft, in *Recent Developments in Gauge Theories*, Ed. by G. 't Hooft *et al.* (Plenum, New York, 1980).
7. A. Vainshtein, Phys. Lett. B **569**, 187 (2003).
8. A. E. Dorokhov, Eur. J. Phys. C **42**, 309 (2005); hep-ph/0505007.
9. See for review, e.g., T. Schafer and E. V. Shuryak, Rev. Mod. Phys. **70**, 323 (1998).
10. S. V. Mikhailov and A. V. Radyushkin, Yad. Fiz. **49**, 794 (1989) [Sov. J. Nucl. Phys. **49**, 494 (1989)]; Phys. Rev. D **45**, 1754 (1992).
11. A. E. Dorokhov, S. V. Esaibegian, and S. V. Mikhailov, Phys. Rev. D **56**, 4062 (1997); A. E. Dorokhov, S. V. Esaibegyan, A. E. Maximov, and S. V. Mikhailov, Eur. Phys. J. C **13**, 331 (2000).
12. A. E. Dorokhov and L. Tomio, Phys. Rev. D **62**, 014016 (2000).
13. R. S. Plant and M. C. Birse, Nucl. Phys. A **628**, 607 (1998).
14. I. V. Anikin, A. E. Dorokhov, and L. Tomio, Fiz. Élem. Chastits At. Yadra **31**, 1023 (2000) [Phys. Part. Nucl. **31**, 509 (2000)].
15. A. E. Dorokhov and W. Broniowski, Eur. Phys. J. C **32**, 79 (2003).
16. A. E. Dorokhov, Phys. Rev. D **70**, 094011 (2004).
17. A. E. Dorokhov, Pis'ma Zh. Éksp. Teor. Fiz. **77**, 68 (2003) [JETP Lett. **77**, 63 (2003)]; I. V. Anikin, A. E. Dorokhov, and L. Tomio, Phys. Lett. B **475**, 361 (2000).
18. A. E. Dorokhov, Phys. Part. Nucl. Lett. **1**, 240 (2004).

JETP Letters, Vol. 82, No. 1, 2005, pp. 14–16. Translated from Pis'ma v Zhurnal Éksperimental'noĭ i Teoreticheskoĭ Fiziki, Vol. 82, No. 1, 2005, pp. 15–17.

Measurement of the Azimuthal Anisotropy Coefficient v_2 for the Emission of α Particles in Nucleus–Nucleus Collisions at Energies 1.88–10.6 GeV/nucleon

V. V. Dubinina, N. P. Egorenkova, V. I. Krotkova, E. A. Pozharova, and V. A. Smirnitskiĭ

Institute of Theoretical and Experimental Physics, ul. Bol'shaya Cheremushkinskaya 25, Moscow, 117218 Russia

Received March 9, 2005; in final form, June 1, 2005

The azimuthal anisotropy of the emission of α particles in collisions of the ^{22}Ne, ^{24}Mg, ^{56}Fe, and ^{197}Au nuclei with photoemulsion nuclei has been measured at projectile energies E_{pr} = 1.88–10.6 GeV/nucleon. The results are compared with similar measurements for protons. It has been found that the ratio of the azimuthal anisotropy coefficients v_2 for α particles and protons is equal to 6 ± 2 at low energies $E_{pr} \approx 2$ GeV/nucleon, whereas these coefficients coincide with each other for energies $E_{pr} \geq 4$ GeV/nucleon. This difference may indicate that, at low projectile energies, α particles are formed predominantly at the early stage of a collective flow. Formation of α particles for $E_{pr} \geq 4$ GeV/nucleon likely occurs at the stage of nuclear matter scattering. *© 2005 Pleiades Publishing, Inc.*

PACS numbers: 25.55.–e

Collision of relativistic nuclei allows the properties of strongly compressed nuclear matter at high temperature T and high nucleon density n, which arise at the instant of collision, to be analyzed under controlled laboratory conditions. A collective flow of nuclear matter (correlated emission of hadrons and mesons) has been observed in many experiments [1–5]. Investigation of so-called "ejection" or "squeeze-out" of nuclear matter in the direction perpendicular to the nuclear-reaction plane is of most interest [6–10]. This direction is the only direction in which particles may be emitted without interactions and collisions with the matter of the projectile and target nuclei. The emission of particles perpendicularly to the nuclear reaction plane can be determined by measurement of azimuthal anisotropy, which is described by the nuclear equation of state $\varepsilon(n, T)$ [1, 11, 12]. The anisotropic azimuthal distribution of particles is approximated by the second-order Legendre polynomial [8]

$$dN/d\varphi = a(1 + v_1\cos\varphi + v_2\cos 2\varphi),$$

where φ is the azimuth angle of particles in the plane perpendicular to the momentum of the projectile nucleus, v_1 is the coefficient characterizing asymmetry in the nuclear reaction plane or so-called *direct flow*, and v_2 is the azimuthal anisotropy parameter that determines the emission of particles in the direction perpendicular to the nuclear reaction plane or so-called elliptic flow. The in- to out-plane emission ratio is given by

$$R = [N(90°) + N(270°)]/[N(0°) + N(180°)] = (1 - v_2)/(1 + v_2).$$

If $v_2 < 0$, the dominant emission of particles is observed in the direction perpendicular to the nuclear reaction plane, whereas for $v_2 > 0$ the dominant flow is directed in the reaction plane. This phenomenon has been quantitatively described using various models [1, 3, 9, 12–14]. Azimuthal anisotropy for hadrons (parameter v_2) is theoretically described as a function of the energy of the projectile nucleus and, therefore, as a function of nucleon density and temperature in the collision zone. The results of measurement of the coefficient v_2 for relativistic particles in collisions of various nuclei with photoemulsion nuclei were given in [15] along with data from other works. The production of light nuclei in collisions of high-energy heavy ions through intermediate stages of fireball development was analyzed in [16], where detailed bibliography was also given.

Experiments with relativistic nuclei for projectile energies E_{pr} = 1–11 GeV/nucleon [1, 3] show that, for energy $E_{pr} = E_{tr} \approx 4$ GeV/nucleon, a change in the sign of the anisotropy parameter v_2 is observed for protons ($v_2 < 0$ for $E_{pr} < E_{tr}$ and $v_2 > 0$ for $E_{pr} > E_{tr}$). Anisotropy arising for the emission of fragments with the change number $Z \geq 2$ ($A \geq 4$) has not yet been systematically studied in this energy range. The dependence of the coefficient v_2 on the projectile energy is unknown for α particles, the energy E_{pr} at which v_2 changes sign has not yet been determined, and it is unknown whether E_{tr} values for protons and α particles are equal to each other. It was shown in [7] that the coefficient v_2 for a projectile energy of 0.4 GeV/nucleon for fragments with A = 4 depends on $P_\perp$ and it is four to five times larger than v_2 for A = 1. This result may be due to the fact that heavy particles are more sensitive to the collective energy: the heavier the particle, the higher its collective-motion momentum. For energies up to 1.6 GeV,

0021-3640/05/8201-0014$26.00

the dependence of v_2 on the projectile energy is measured in this experiment only for the sum $A = 1 + 2 + 3$. The dependence of the sign and magnitude of the anisotropy coefficient v_2 on E_{pr} and, therefore, on the density and temperature of nuclear matter is more efficiently observed in experiments with multicharged fragments.

In order to determine the dependence of the magnitude and sign of v_2 on the projectile energy and to estimate the E_{tr} value at which v_2 changes sign, we measured the azimuthal anisotropy of the emission of α particles in experiments on the interaction of various nuclei with photoemulsion nuclei in the range E_{pr} = 1.88–10.6 GeV/nucleon. We used nuclear photoemulsion irradiated by nuclei ^{56}Fe (E_{pr} = 1.88 GeV/nucleon), ^{22}Ne (E_{pr} = 3.25 GeV/nucleon), ^{24}Mg (E_{pr} = 3.85 GeV/nucleon), and ^{197}Au (E_{pr} = 10.6 GeV/nucleon). Nucleus–nucleus collisions were analyzed for semicentral interactions [4] corresponding to the impact parameter b in the range $0.20 \le b/b_{max} \le 0.70$. We selected events with no less than three α particles (we assumed that all particles with $Z = 2$ have $A = 4$). The nuclear reaction plane was determined for all interactions. Then, the reaction planes for all collisions were joined together for each projectile nucleus and the parameter v_2 was calculated. The procedure of event selection, determination of the nuclear reaction plane, and analysis of interactions was described in detail in [2, 17, 18].

The figure shows the measured azimuthal anisotropy coefficient v_2 for α particles as a function of E_{pr} along with the results of similar measurements for protons (for the same E_{pr} range) from [3]. As is seen, v_2 for both the proton and α particle changes sign at $E_{pr} \approx$ 4 GeV/nucleon. The calculation results for $\varepsilon(n, T)$ that describe the coefficient v_2 as a function of E_{pr} in the range from 1 to 11 GeV/nucleon and, therefore, as a function of nucleon density n and temperature T in the collision zone were given in [1]. The calculation was performed using the relativistic transport model based on the Landau theory of relativistic quasiparticles [12]. Measurements of a positive v_2 value at the HIC-BNL energy provide the fundamental conclusion that Landau hydrodynamics is applicable beginning with early stages of nuclear collisions [19]. The experimental data for protons that are shown in the figure are described for $E_{pr} < E_{tr}$ and $E_{pr} > E_{tr}$ by the stiff and soft nuclear equations of state, respectively [1, 3]. It is impossible to apply the theoretical calculation of those works to the comparison of the dependences of v_2 on E_{pr} for protons and α particles, because α-particle degrees of freedom were disregarded in that calculation.

Measurement of the dependence of v_2 on E_{pr} for α particles is important for understanding of the process of their formation in nucleus–nucleus collisions. The

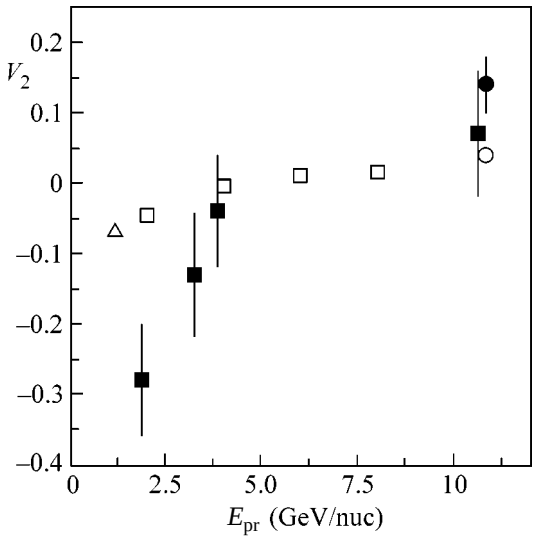

Azimuthal anisotropy coefficient v_2 vs. projectile energy E_{pr}: (■) our data for (α, A + Em), (●) (α, Au + Em) [5], (□) (p, Au + Au) [3] (E895 Collaboration), (△) (p, Au + Au) EOS Collaboration, and (○) (p, Au + Au) E866 Collaboration.

ratio of the azimuthal anisotropy coefficients v_2 for α particles and protons for $E_{pr} < E_{tr}$ is as follows:

$$v_2(E_{pr}(\alpha) = 1.88 \text{ GeV/n})/v_2(E_{pr}(p) = 1.15 \text{ GeV/n}) = 5.0 \pm 2.0;$$

$$v_2(E_{pr}(\alpha) = 1.88 \text{ GeV/n})/v_2(E_{pr}(p) = 2.0 \text{ GeV/n}) = 6.0 \pm 2.0.$$

The change in the sign and magnitude of v_2 as a function of the projectile energy in the indicated E_{pr} range (see figure) is possibly attributed to change in the mechanism of the production of light nuclei in ion collisions. The above data on the ratio of the azimuthal anisotropy coefficients imply that, for low energies $E_{pr} < 4$ GeV/nucleon, α particles are formed predominantly at the early stage of the collective flow and the matter of the projectile and target nuclei prevents their emission in the nuclear reaction plane. Since the cross section for interaction of α particles is much larger than the nucleon cross section, the inequality $|v_2(\alpha)| > |v_2(p)|$ is necessarily valid, as is observed in experiment. The direction perpendicular to the reaction plane is free for the emission of particles, and this property corresponds to a negative v_2 value. For energies $E_{pr} > E_{tr}$, $v_2(\alpha) \sim v_2(p)$ (see figure) and formation of α particles likely occurs at the stage of nuclear matter scattering, when spectator nucleons do not prevent the emission of α particles and, as a result, the equality of azimuthal anisotropy coefficients is observed.

We are grateful to V.V. Shamanov for assistance in the organization of computer processing of the experimental data.

REFERENCES

1. P. Danielewicz, R. A. Lacey, P. B. Gossiaux, *et al.*, Phys. Rev. Lett. **81**, 2438 (1998); C. Pinkenburg, N. N. Ajitanand, J. M. Alexander, *et al.*, Phys. Rev. Lett. **83**, 1295 (1999).
2. M. Adamovich, E. Basova, M. Chernyavskiĭ, *et al.*, Yad. Fiz. **60**, 1580 (1997) [Phys. At. Nucl. **60**, 1435 (1997)]; Eur. Phys. J. A **6**, 427 (1999).
3. G. Rai, N. Ajitanad, J. Alexander, *et al.* (E895 Collab.), Nucl. Phys. A **661**, 162 (1999).
4. D. Brill, W. Ahner, P. Baltes, *et al.*, Phys. Rev. Lett. **71**, 336 (1993).
5. A. Pylos, *European School of High-Energy Physics* (Geneva, 2004), CERN-2004-001; P. Jain, G. Singh, and A. Mukhopadyay, Phys. Rev. Lett. **74**, 1534 (1995); L. Chkhaidze, T. Djobava, L. Khakhelauri, *et al.*, Preprint No. E1-2002-255, OIYaI (Joint Inst. for Nuclear Research, Dubna, 2002).
6. H. Gutbrod, K. Kampert, B. Kolb, *et al.*, Phys. Rev. C **42**, 640 (1990).
7. A. Andronic (FOPI Collab.), Nucl. Phys. A **661**, 333 (1999).
8. P. Jain and G. Singh, Mod. Phys. Lett. A **9**, 1445 (1994).
9. S. Kiselev, Nucl. Phys. A **579**, 643 (1994).
10. S. Voloshin, Nucl. Phys. A **715**, 379 (2003); U. Heinz and M. N. Wong, Nucl. Phys. A **715**, 649 (2003); A. Wetzler, N. Borghin, P. M. Dinh, *et al.*, Nucl. Phys. A **715**, 583 (2003); S. Esumi (for the PHENIX Collab.), Nucl. Phys. A **715**, 599 (2003).
11. V. Aichelin, Phys. Rep. **202**, 233 (1991).
12. G. Baym and S. Chin, Nucl. Phys. A **262**, 527 (1976).
13. S. Belenkiy and L. Landau, Nuovo Cimento Suppl. **3**, 15 (1957).
14. H. Stöker, Phys. Rev. Lett. **44**, 725 (1980).
15. M. I. Adamovich, N. P. Andreeva, E. S. Basova, *et al.*, Yad. Fiz. **67**, 290 (2004) [Phys. At. Nucl. **67**, 273 (2004)].
16. B. L. Ioffe, I. A. Shushpanov, and K. N. Zyablyuk, Int. J. Mod. Phys. E **13**, 1157 (2004).
17. J.-Y. Ollitrault, Phys. Rev. D **48**, 1132 (1993); P. Danielewicz and G. Odyniec, Phys. Lett. B **157B**, 146 (1985); P. Danielewicz, H. Strobele, G. Odyniec, *et al.*, Phys. Rev. C **38**, 120 (1988).
18. V. V. Dubinina, N. P. Egorenkova, V. I. Krotkova, *et al.*, Yad. Fiz. **67**, 537 (2004) [Phys. At. Nucl. **67**, 518 (2004)].
19. U. W. Heinz, AIP Conf. Proc. **739**, 163 (2004); E. Shuryak, Prog. Part. Nucl. Phys. **53**, 273 (2004); P. Steinberg, in *Proceedings of 20th Winter Workshop on Nuclear Dynamics* (Trelawny Beach, Jamaica, 2004).

Translated by R. Tyapaev

JETP Letters, Vol. 82, No. 1, 2005, pp. 17–21. From Pis'ma v Zhurnal Éksperimental'noĭ i Teoreticheskoĭ Fiziki, Vol. 82, No. 1, 2005, pp. 18–22.

2D Laser Collimation of a Cold Cs Beam Induced by a Transverse *B* Field¶

M. D. Plimmer[1], N. Castagna[1], G. Di Domenico[1], P. Thomann[1], A. V. Taichenachev[2, 3], and V. I. Yudin[2, 3]

[1] *Observatoire Cantonal, 2000 Neuchâtel, Switzerland*

[2] *Novosibirsk State University, Novosibirsk, 630090 Russia*

[3] *Institute of Laser Physics, Siberian Division, Russian Academy of Sciences, Novosibirsk, 630090 Russia*

e-mail: Mark.Plimmer@ne.ch

Received April 26, 2005

We describe transverse collimation of a continuous cold cesium beam (longitudinal temperature 75 μK) induced by a two-dimensional, blue-detuned near-resonant optical lattice. The mechanism described for a lin-||-lin configuration is made possible by the application of a transverse magnetic field $B_\perp$. The phenomenon described differs from gray molasses, for which any small magnetic field degrades cooling, as well as from magnetically induced laser cooling in red-detuned optical molasses, where there are no dark states. The lowest transverse temperature is experimentally found to vary as $B_\perp^2$. The collimated flux density shows a dip as a function of $B_\perp$, the width of which is proportional to the cube root of the laser intensity, general features predicted by our semiclassical model. This technique provides a sensitive tool for canceling transverse magnetic fields *in situ* at the milligauss level. © *2005 Pleiades Publishing, Inc.*

PACS numbers: 32.60.+i

Continuous beams of cold atoms are useful for many physics experiments. Their flux density can be boosted by two-dimensional (2D) transverse laser collimation. Some schemes to achieve this with a 2D optical lattice (OL) use applied magnetic fields in addition to the lasers [1], while others should work better in zero field [2]. Both methods are designed to approach transverse temperatures close to the recoil limit (0.2 μK). The simplest approach is polarization gradient cooling (optical molasses (OM)) leading to temperatures of about 3 μK. With no polarization gradient, collimation can still be achieved if a transverse magnetic field ($B_\perp$) is applied. Conversely, one can use this technique to monitor transverse magnetic fields *in situ*. In this letter, we describe a study of laser collimation of a continuous cesium beam induced by a ($B_\perp$) for the $F = 3 \longrightarrow F' = 2$ component of the D_2 line and its implications for field cancellation.

For transitions of the type $J \longrightarrow J' = J$ or $J - 1$, cooling occurs for a laser tuned to the blue of the atomic resonance, while the presence of dark states in the ground hyperfine level leads to gray OM and, thereby, somewhat lower temperatures than those obtained with red-detuned OM ($J \longrightarrow J + 1$). In their study of the $F = 1$ to $F' = 1$ transition in ^{87}Rb in a 1D lin-θ-lin OM, Lucas *et al.* [3] measured temperature as a function of θ and concluded that the cooling observed near $\theta = 0$ arose from some residual polarization gradient. We have also investigated collimation as a function of θ in a 2D phase-stable power-recycling lattice [4]. To minimize θ, we adjusted the vertical input polarization of the input beam such that the extinction of the outgoing reflected beam, analyzed by a polarizing beam-splitter cube, was $<10^{-3}$. We still observed sub-Doppler temperatures but only when a transverse magnetic field was applied.

Although magnetically induced laser cooling (MILC) was described over a decade ago [5–8], most work has been on $J \longrightarrow J + 1$ transitions,[1] but published data on $J \longrightarrow J - 1$ transitions are rarer. Metcalf's group mentions results for the textbook case of 1D collimation of a ^{87}Rb beam on the $F = 1 \longrightarrow F = 0$ transition in a weak $B_\perp$ field with no polarization gradient (σ^+–σ^+ [9], lin-||-lin [10]). Nienhuis *et al.* [11] calculated a graph of reduced force versus reduced velocity for 1D cooling of a $J = 2 - J' = 1$ transition in a similar configuration but with a strong $B_\perp$ field and red detuning. The only work on Cs of which we are aware is by Valentin *et al.* [12–14], who studied the $F = 3 \longrightarrow F' = 2$ component of the D_2 line. There and in the experiments of Metcalf's group [5, 6], a thermal atomic beam was collimated in a 1D standing wave to sub-Doppler transverse temperatures in either strong magnetic fields

¶ This article was submitted by the authors in English.

[1] Indeed, we observe the effect for red-detuned molasses using the $F = 4 \longrightarrow F' = 5$ component of the Cs D_2 line.

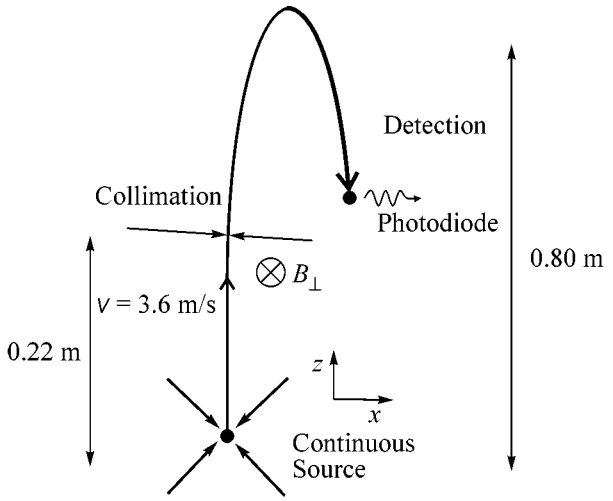

Fig. 1. Experimental setup for 2D collimation of a continuous Cs beam. The various lasers are tuned near hyperfine components of the D_2 line.

(Larmor frequency $\Omega_L \geq$ ground-state light shift Δ_{LS}) or weak ones ($\Omega_L < \Delta_{LS}$). In all of the above, the results describe cooling to zero transverse velocity $v_\perp$ in low fields and to $v_\perp \neq 0$ in high fields. All of the calculations were numerical simulations, and, to the best of our knowledge, no analytical expressions for the transverse temperature $T_\perp$ as a function of $B_\perp$ were given. Our own experiment is different in that it concerns 2D collimation of a continuous Cs beam using an OL with parallel linear polarization vectors; the magnetic fields are always weak ($B_\perp < 120$ mG), and the atoms, already cold to begin with (longitudinal temperature 75 μK, $T_\perp = 60$ μK), are transversely cooled to $T_\perp \approx 5$ μK.

In this letter, we present a detailed study of 2D MILC, including the influence of applied transverse magnetic fields on the atomic flux and final temperature for the case of an $F \longrightarrow F - 1$ transition. We show that, even if the mechanism appears on the blue side of the atomic resonance, it is different from usual gray molasses in two respects. First, gray molasses requires a polarization gradient, which is not the case here. Second, gray molasses is destroyed by a B field, be it transverse or longitudinal [15]. We outline the experimental arrangement and, then, present the results obtained, which show the striking contrast between the case of parallel polarizations (no polarization gradient, $\sin^2\theta < 10^{-3}$) and orthogonal ones (maximal gradient). Then, we compare our situation with gray molasses ($F \longrightarrow F$ or $F - 1$ with a polarization gradient). To gain some physical insight, we perform an extensive semiclassical analysis of MILC on $F \longrightarrow F - 1$ transitions in a linearly polarized standing wave. A qualitative picture of the Sisyphus cooling mechanism in the case under consideration is given. We find that, in a weak magnetic field, when the Zeeman splitting is less than the average light shift, the usually used slow-atom approximation fails due to a strongly nonlinear velocity dependence of the light force on the atom near $v = 0$. This can be qualitatively explained by high spatial gradients of the atomic density matrix and a small optical pumping rate near the field nodes. Instead, we obtain the nonlinear force dependence by numerical calculations, based on the expansion of the density matrix in a Fourier series that give results qualitatively similar to those found by experiment. Lastly, we present the transverse magnetic field cancellation procedure based on real-time measurement of the atomic flux.

The apparatus shown in Fig. 1 is akin to that of [1], where the z axis is vertical. Cs atoms from a moving OM are launched continuously in a parabolic flight with an initial velocity $v_z = 3.6$ m/s [16]. In a region above the source, the slow beam is collimated using a 2D linear-θ-linear OL with a $1/e^2$ intensity radius = 5.7 mm, truncated at a radius of 9 mm. We define I_1 as the average single-beam intensity in a circle of radius equal to the waist w. Here, a laser tuned 3γ above resonance with the $F = 3 - F' = 2D_2$ hyperfine component (where γ is the natural width of the excited state $6p\ ^2P_{3/2}$) is used in a phase-stable, power-recycling geometry with perpendicular, coplanar, counterpropagating beams [4]. These are reflected from gold-coated mirrors to maximize reflectivity ($R > 97\%$) and minimize birefringence; improvement is expected from silver ones [17]. We observed that, when there is no polarization gradient, no collimation occurs unless one applies a transverse B field (but not a longitudinal one). A weak repumping laser (0.1 mW/cm^2) tuned to the $F = 4 \longrightarrow F' = 3$ hyperfine component of the D_2 line is added to improve cooling efficiency in the lattice. At the end of the flight, the atomic flux is probed via laser-induced fluorescence of the $F = 4 \longrightarrow F' = 5$ transition of the D_2 line. By adding a repumping beam in the probe region tuned to the $F = 3 \longrightarrow F' = 4$ transition, we can detect the atoms arriving in both the $F = 3$ and $F = 4$ hyperfine levels. We measure transverse temperatures by laterally translating the whole detection system (probe and repumping lasers and detection optics) in the horizontal plane and recording flux as a function of displacement. The data are fitted to a Gaussian curve (collimated atoms) superimposed on a slope representing the wings of a much broader distribution of uncollimated atoms. Depending on the atomic flux, resolutions of 0.2 μK can be achieved.

We have studied the variation of $T_\perp$ as a function of the mutual angle of inclination θ of the laser polarization vectors when $B_x = B_y = B_z = 0$. For θ = 0, the light field is a 2D lattice with an intensity gradient but uniform polarization and the temperature curve exhibits a local maximum. Still, for θ = 0, we have measured $T_\perp$ and flux versus $B_\perp$ (≤120 mG) when the other field components were cancelled out to within a few milligauss. For $B_x = B_z = 0$, the flux density curve (Fig. 2) shows a characteristic dip as a function of B_y. Similar

results are observed when $B_y = B_z = 0$, and we vary B_x. The width ΔB of the dip varies as the cube root of the lattice laser power over a range 1 to 32 mW (Fig. 3). The intensity of the weak repumping laser has no observable influence upon this width. The corresponding temperature curves exhibit a central maximum, coinciding with the value of $B_\perp$ that gives the smallest flux. Away from this maximum, we find that $T_\perp$ rises as $B_\perp^2$. This behavior is in striking contrast with the variation of flux density with B_z ($B_x = B_y = 0$), where we observe no collimation whatsoever. There is also a dramatic contrast with the behavior of flux versus $B_\perp$ for $\theta = 90°$, i.e., gray molasses, which displays a local central *maximum* at $B_\perp = 0$.

Cooling mechanism. Figure 4 shows the calculated adiabatic potentials, i.e., the eigenvalues of the total Hamiltonian of an atom at rest, including both the optical shift operator and the Zeeman shift operator. The four potential curves correspond to the dressed states, which, for $B_\perp = 0$, coincide with Zeeman substates of the ground $F = 3$ hyperfine level with the magnetic quantum numbers $m_F = \pm 2$ and $m_F = \pm 3$. They apply to the case of a weak $B_\perp$ and a linearly polarized standing wave ($\theta = 0$). The contribution due to off-resonant coupling with $^2P_{3/2}F' = 3$ is also taken into account. The energies are in kilohertz for the average lattice intensity of our experiment, namely, 3.5 mW/cm^2. Level crossing near the nodes is avoided due to the B-field mixing (the corresponding Zeeman splitting is taken as 5.3 kHz). In a weak magnetic field, the whole cooling process of transitions between the coupled $F = 3$, $m_F = \pm 2$ and noncoupled $F = 3$, $m_F = \pm 3$ dressed states takes place in the vicinity of the nodes, where the Zeeman splitting is comparable with the optical shifts. Outside these regions, all slow atoms are in the noncoupled states and so dissipate no kinetic energy. Let us consider an atom initially moving in the positive direction in one of the noncoupled states. Near the node (say, when $kx = 0$), it is likely to be coupled by the transverse B field to the dressed states with $m_F = \pm 2$, to climb uphill, and to dissipate its kinetic energy. Later (e.g., at $kx = 0.3$), when the dressed states $m_F = \pm 2$ become strongly coupled with light, it is optically pumped back to the noncoupled states $m_F = \pm 3$. Thus, the kinetic energy dissipated per cycle is of order of the Zeeman energy.

The Sisyphus mechanism [18] breaks down at a very weak magnetic field when an atom moving at the recoil velocity $\hbar k/M$ passes too quickly through the region of efficient B mixing for optical pumping to occur. This qualitatively explains the peak in temperature and the dip in the flux near $B_\perp = 0$. Let us estimate the Zeeman splitting at which it happens. The spatial size x of the region where the B mixing works is defined by $\Omega_R^2/(\delta(kx)^2) \approx \Omega_Z$ (the optical energy shift is comparable with the Zeeman splitting), where $\Omega_R \sin kx \simeq$

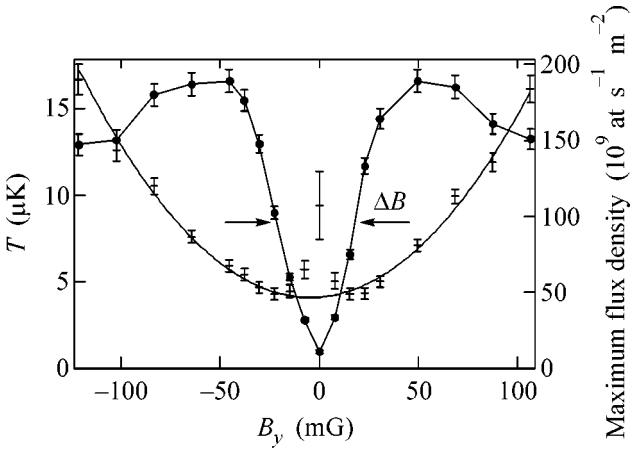

Fig. 2. 2D laser collimation using the Cs D_2 line in a lin-‖-lin lattice with $\theta = 0$, hyperfine component $F = 3 - F' = 2$, and detuning $+3\gamma$. Lattice laser power, 3.5 mW; repumping laser ($F = 4 - F' = 3$) power, 0.12 mW ($w = 5.7$ mm for both lasers). Variation of transverse temperature (+) and flux density (●) as a function of the transverse magnetic field B_y for $B_x = B_z = 0$. The polarization vectors of the lattice beams are along z, so there is no polarization gradient, and the other magnetic field components are cancelled. The solid line in the flux curve is to guide the eye; that in the temperature plot is a quadratic fit excluding the three central points.

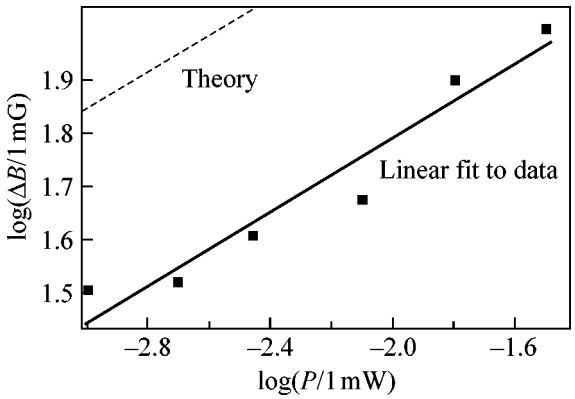

Fig. 3. Plot of the log of the width ΔB (mG) of Fig. 1 versus the log of lattice power P (mW) for $B_x = B_z = 0$. The slope of the linear fit (0.35(4)) suggests that $\Delta B \propto \sqrt[3]{P}$. The theoretical curve predicts the right slope and gives absolute values within a factor of two.

$\Omega_R kx$ is the local Rabi frequency in the vicinity of the well bottom averaged over the lattice volume and δ is the detuning. An atom with the recoil velocity crosses this region in a time $\tau = x(\hbar k/M)$. For efficient mixing in this time period, we need $\tau\Omega_Z \geq 1$, i.e., $\Omega_Z \geq [\omega_r^2\Omega_R^2/\delta]^{1/3}$, where ω_r is the recoil frequency. This power law is confirmed experimentally (Fig. 3) over a range of 30 in laser power. Note that, under our experi-

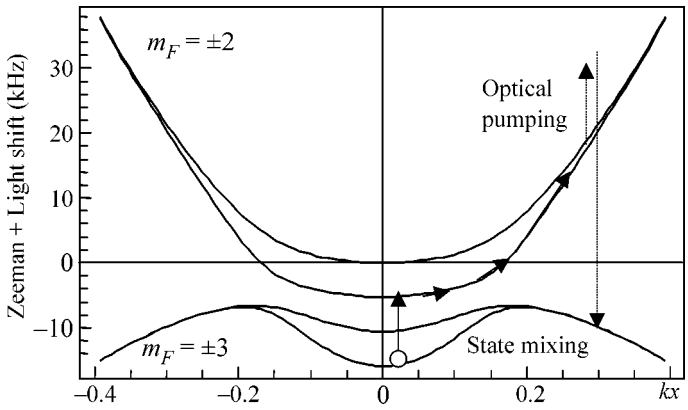

Fig. 4. Cooling principle in a weak magnetic field based on $F = 3 \longrightarrow F' = 2$ optical pumping between Zeeman sublevels of the $F = 3$ ground hyperfine level. Here, we show adiabatic potentials including both Zeeman and light shifts. The modulated light shift of the $m_F = \pm 3$ noncoupled levels arises from off-resonant coupling with the excited $F' = 3$, $m_{F'} = \pm 3$ levels. The value shown is for an average lattice laser intensity of 3.5 mW/cm^2.

mental conditions, the weak magnetic field regime always applies, since the Zeeman splitting is less than the average optical shift. However, in this limit, the condition for applicability of the usually used slow atom approximation is unusually stringent. Indeed, first, we require that

$$\frac{kv}{kx} \ll \gamma \frac{\Omega_R^2}{\delta^2}(kx)^2 \tag{1}$$

where γ is the spontaneous decay rate; i.e., the atom transit time through the region of efficient B-field mixing should significantly exceed the optical pumping time in the same region. In this region, the optical shift and Zeeman splitting are comparable:

$$\frac{\Omega_R^2}{\delta}(kx)^2 \simeq \Omega_Z \tag{2}$$

then

$$kx \simeq \sqrt{\frac{\Omega_Z \delta}{\Omega_R^2}} \ll 1. \tag{3}$$

Additionally, in order to neglect safely motional coupling between the dressed states, we also need

$$kv/kx \ll \mathscr{E} \simeq \Omega_Z, \tag{4}$$

where $\hbar\mathscr{E}$ is the energy separation between adiabatic potentials. Since the first condition is the more stringent, we have, finally,

$$kv \ll \Omega_Z \frac{\gamma}{\delta}\sqrt{\frac{\Omega_Z \delta}{\Omega_R^2}} \ll \Omega_Z. \tag{5}$$

If now we take $\delta = 3\gamma$, $\Omega_Z = 0.01\gamma$ (about 50 kHz), and $\Omega_R = \gamma$ (the corresponding intensity is about 8.8 mW/cm^2), we see that $kv < \gamma/100$; i.e., the corresponding velocity would be deeply subrecoil. Thus, in the weak magnetic field regime, there is hardly any room for the linear velocity approximation, estimates based upon which fail, and we need at least some kind of nonlinear theoretical estimates going beyond the slow-atom approximation. This led us to carry out a semiclassical numerical analysis of the problem.

Let us consider MILC in a linearly polarized monochromatic light field that excites a closed $F_g = F \longrightarrow F_e = F - 1$ transition. We approximate the actual field configuration by a 1D standing wave and neglect all other hyperfine levels. As the simplest model, we use a three-state system consisting of the noncoupled $|\mathrm{NC}\rangle$, coupled $|\mathrm{C}\rangle$, and excited $|\mathrm{E}\rangle$ states. Such a model reflects the main qualitative features of MILC on dark transitions. We take both the Doppler shift kv and Zeeman splitting Ω to be $\ll \gamma$ and assume that the laser field intensity and detuning correspond to the low-saturation limit:

$$S = \frac{1}{2}\frac{\Omega_R^2}{(\gamma/2)^2 + \delta^2} \ll 1. \tag{6}$$

There exist well-developed numerical methods to calculate the force and diffusion coefficient in an arbitrary 1D periodic light field. Typically, these are based on the expansion of the atomic density matrix in a Fourier series with subsequent numerical solution of a finite set of algebraic equations, obtained by the truncation of the original infinite set at some higher harmonic with number $n_{\max}$. An especially powerful tool for the force calculation is the continued fraction operator method, because, at each step, we need to invert a matrix of only low dimension whatever $n_{\max}$. The results for the spatially averaged force as a function of velocity are presented in Fig. 5. One can see a linear dependence very close to $v = 0$, a first Raman resonance at $kv \simeq \Omega_Z$ [6], and higher-order ones at $mkv \simeq \Omega_Z$ (with m an integer). The force behavior is qualitatively similar for the three-state model and for the $3 \longrightarrow 2$ transition studied experimentally.

One can evaluate the final momentum distribution $W(p)$ using the spatially averaged Fokker–Plank equa-

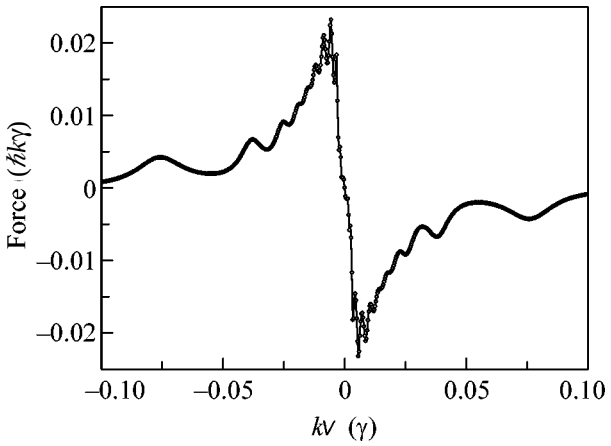

Fig. 5. Three-state model. The force in $\hbar k\gamma$ units versus kv/γ. The detuning $\delta = 3\gamma$, the Zeeman splitting $\Omega_Z = 0.01\gamma$, and the Rabi frequency $\Omega_R = \gamma$.

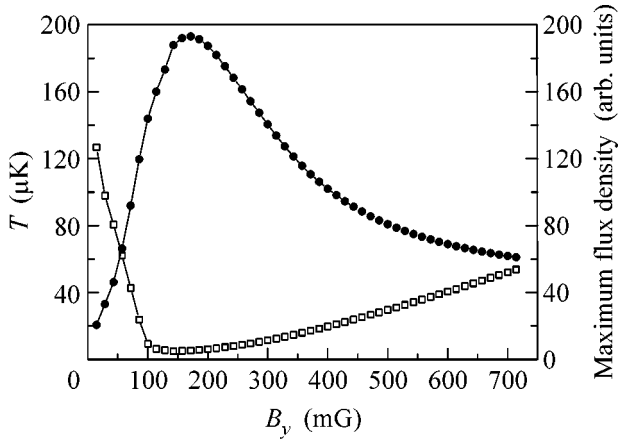

Fig. 6. Three-state model. Maximum flux density (●) in arbitrary units and the temperature (○) in microkelvin versus magnetic field in mG. The parameters are $\delta = 3\gamma$, $\Omega_R = \gamma$. There is qualitative agreement with experiment (Fig. 1, right-hand side).

tion. Typically, we observe non-Gaussian shapes and narrow double-peaked features near the zero momentum, which are gradually transformed into the peaks at nonzero velocities. To compare theory and experiment, we numerically calculate the Gaussian width w ($W(w) = W(0)/e$) and $W(0)$; the latter represents the maximal flux. We assume that $T \propto w^2$ and that $w = \hbar k$ corresponds to $T = 0.1$ μK. The results of such calculations, shown in Fig. 6, are qualitatively similar to experimental data. In particular, we see the "$B_\perp^2$" temperature dependence and a flux maximum offset slightly from the temperature minimum, as in Fig. 1. A detailed account of our theoretical models will be presented elsewhere.

Application: *in situ* compensation of $B_\perp$ fields. Three orthogonal pairs of Helmholtz coils provide the necessary static fields. The resolution of the current supplies leads to an uncertainty of ±2 mG for B_x and B_y and ±2.5 mG for B_z. Slow ambient fluctuations amount to ±0.2 mG for B_x and B_y and ±1.5 mG for B_z, and there subsist 50-Hz fields of <3 mG in all three directions. We start with 2D gray OM on the $F = 3 \longrightarrow F' = 2$ component of the D_2 line using a lin ⊥ lin configuration to provide the largest polarization gradient. Since any small magnetic field component leads to higher temperatures and lower flux, we adjust B_x, B_y, and B_z to *maximize* the flux. This first step is, thus, a bright-field technique. For a sensitivity <10 mG, we make the lattice polarization vectors parallel and vertical, so that B_x and B_y are the transverse fields. We then tune B_x and B_y to *minimize* the flux (dark-field method). To make B_z, the transverse field, the laser polarization should be horizontal. In 2D, this gives a polarization gradient and, thus, just gray molasses. However, by implementing a 1D lattice, one could also cancel B_z using MILC.

A.V.T. and V.I.Yu. are grateful to the Swiss National Science Foundation (FNRS) for financing an exchange visit. Their work is supported in part by the Russian Foundation for Basic Research (project nos. 05-02-17086 and 04-02-16488) and by INTAS (grant no. 01-0855). The authors thank D. Boiron and S. Pádua for supplying Ph. D. theses and C. Affolderbach and P. Berthoud for critical input. Experiments were partially supported by FNRS and METAS.

REFERENCES

1. G. Di Domenico *et al.*, Phys. Rev. A **69**, 063403 (2004).
2. A. V. Taichenachev *et al.*, Phys. Rev. A **63**, 033402 (2001).
3. D. M. Lucas, P. Horak, and G. Grynberg, Eur. Phys. J. D **7**, 261 (1999).
4. G. Di Domenico *et al.*, physics/0412072.
5. B. Sheehy *et al.*, Phys. Rev. Lett. **64**, 858 (1990).
6. P. van der Straten *et al.*, Phys. Rev. A **47**, 4160 (1993).
7. P. J. Ungar *et al.*, J. Opt. Soc. Am. B **6**, 2058 (1989).
8. D. S. Weiss *et al.*, J. Opt. Soc. Am. B **6**, 2072 (1989).
9. R. Gupta *et al.*, J. Opt. Soc. Am. B **11**, 537 (1994).
10. S. Pádua, PhD Thesis (SUNY, Stony Brook, 1993) (unpublished).
11. G. Nienhuis, P. van der Straten, and S.-Q. Shang, Phys. Rev. A **44**, 462 (1991).
12. C. Valentin *et al.*, Europhys. Lett. **19**, 133 (1992).
13. J. Yu *et al.*, IEEE Trans. Instrum. Meas. **42**, 109 (1993).
14. C. Valentin, PhD Thesis (Univ. de Paris-Sud, 1994) (unpublished).
15. C. Triché, P. Verkerk, and G. Grynberg, Eur. Phys. J. D **5**, 225 (1999).
16. P. Berthoud, E. Fretel, and P. Thomann, Phys. Rev. A **60**, R4241 (1999).
17. C. W. Goodwin, private communication (2004).
18. J. Dalibard and C. Cohen-Tannoudji, J. Opt. Soc. Am. B **6**, 2023 (1989).

JETP Letters, Vol. 82, No. 1, 2005, pp. 22–25. Translated from Pis'ma v Zhurnal Éksperimental'noĭ i Teoreticheskoĭ Fiziki, Vol. 82, No. 1, 2005, pp. 23–26.

Scale Invariance of the Structure upon Explosive Crystallization of Amorphous Films

L. I. Kveglis, V. A. Seredkin, and A. V. Kuzovnikov

Kirenskĭ Institute of Physics, Siberian Division, Russian Academy of Sciences, Akademgorodok, Krasnoyarsk, 660036 Russia

Received May 23, 2005

Experimental results that are obtained in the process of the explosive crystallization of x-ray amorphous films Fe_2Tb and CoPd with magnetic anisotropy perpendicular to the film plane are reported. The internal bending of thus obtained "single crystals" reaches 100 deg/μm. An explanation of the mechanism and kinetics of explosive crystallization in the Fe_2Tb and CoPd films is proposed in the framework of the shear transformation zone theory. © *2005 Pleiades Publishing, Inc.*

PACS numbers: 75.50.Kj

The problem of the microstructure of amorphous and nanocrystalline materials obtained under nonequilibrium conditions is an important unsolved problem of solid state physics. For this reason, experimental investigations of the structure formation in such materials are of decisive importance for revealing and understanding the general laws governing amorphous and nanocrystalline substances, as well as for determining their nature and new possibilities of using them in engineering. We study Fe–Tb and Co–Pd nanocrystalline films obtained under nonequilibrium conditions. Explosive crystallization initiated by a small thermal action of 0.1–0.2 kT_{melt} or mechanical impact is observed in these films.

This work is devoted to determination of the mechanism of explosive crystallization in amorphous films of alloys based on transition metals. The regular crystal lattice does not necessarily grow in film structures; i.e., the length and arrangement of short-range interatomic bonds do not always coincide with the length and arrangement of bonds in the regular structure, respectively. In this case, local regularity is combined with adaptability necessary for growth. This behavior is observed in twin structures and quasicrystals [1] obtained under ultrafast cooling conditions. If films are magnetically ordered, their saturation magnetization upon explosive crystallization usually decreases [2, 3].

One of the aims of this work is to analyze the physical nature of explosive crystallization and the corresponding features of structure formation (rotation shifts and internal bending of an atomic lattice that are as large as 100 deg/μm or larger) in the framework of the shear transformation zone (STZ) theory [4–6]. This theory is based on the concept that macroscopic deformation in amorphous materials is a result of local rearrangements due to the cooperative motion of molecules in mesoscopic domains [4]. Plastic flow is created due to the creation and annihilation of the transformation zone whose velocity depends linearly on load. A dynamic model of super-Arrhenius relaxation in glassy materials was recently developed in [5] and is based on a well-known liquid-like model [6]. The authors of [5] proposed a hypothetical mechanism that "might be visualized as a kinetic fluctuation that allows molecules to undergo small displacements along a force chain"—a string. Let the string length be equal to Nl, where N is an integer and l is a certain characteristic molecular length, and a domain with radius R arises around the STZ string. The expression for the total free energy of the system has the form

$$\Delta G(N, R) = \Delta G_\infty + Ne_0 - TS(N, R) + E_{int}(N, R), \quad (1)$$

where the first term is the activation energy for high temperatures, which is necessary for formation of a vacancy or a free gap. It is the Arrhenius activation energy. The remaining terms describe the string as a fluctuation in a solid glass: $T_0 \equiv e_0/\nu k_B$, where e_0 is the energy per step along the string and $\nu = \ln q$, where q is the number of paths possible for each transition. The number of such transitions is given by the expression

$$W(N, R) \approx \text{const} \times q^N \exp\left(-\frac{R^2}{2N\lambda^2}\right). \quad (2)$$

The entropy that is obtained by calculating the number of free transitions consisting of N steps in the radius R is written as

$$S(N, R) \approx \nu k_B N - k_B \frac{R^2}{2N\lambda^2}. \quad (3)$$

The repulsion energy is given by the expression

$$E_{\text{int}}(N, R) \approx k_{\text{B}}T_{\text{int}}\frac{N^2\lambda^d}{R^d}, \quad (4)$$

where $k_{\text{B}}T_{\text{int}}$ is the dimensionless repulsion energy and d is the dimension of space where the string exists.

An irreversible transition occurs between the internal states of an amorphous solid. Adam and Gibbs [7] divided the free energy of viscous-flow activation into two components: the energy of interatomic-bond changeover and the energy necessary for the rearrangement of a large group of atoms. The authors of [5] postulated "that, at temperatures low enough that most of the system is tightly jammed, localized molecular rearrangements might be entropically enabled by strings of small molecular displacements that distribute the disturbance throughout larger parts of the material."

The Fe_2Tb and CoPd films were obtained by deposition with a rate of 10 nm/s on glass substrates in a vacuum of 2×10^{-4} Pa and at room temperature. The thickness of the films under investigation was equal to about 50 nm. The films were separated from the substrates by etching in a 10% hydrofluoric-acid solution with the subsequent washing in distilled water. The microstructure and phase composition of the films were analyzed using a transmission electron microscope PREM-200.

The initial Fe_2Tb and CoPd films are x-ray amorphous, which is corroborated by the diffuse diffraction patterns. Electron-beam-induced crystallization occurs with a rate of about 1 cm/s with formation of dendrites. We noted that domains with similar structure to the single-crystal structure arose from the x-ray amorphous structure under the action of either an electron beam or mechanical load in a short time (~0.1 ms). Electron microdiffraction patterns (see Fig. 1a) obtained from these domains are similar to the diffraction pattern from a single crystal. Point reflections in the electron diffraction patterns are strongly dispersed, and no ring reflections are observed. Microphotographies of the "single crystals" (see Fig. 1b) exhibit bending contours in the form of dark fringes that testify to strong internal bending of "atomic planes," which reaches 100 deg/μm [9].

Since point reflections are strongly dispersed on electron diffraction patterns, interatomic distances vary within a range of 8%. For this reason, we think that the exited-atom model on which the STZ theory is based is applicable to such films. Atoms that can be shifted at a critical distance corresponding to the maximum interatomic attraction are called excited atoms [10].

Comparison of data obtained by x-ray and electron diffractometry indicates that single crystals without long-range order grow in the Fe_2Tb and CoPd films. Nanocrystallites with the [110] zone axis are oriented with respect to each other as blocks of a mosaic and imitate a single crystal. Investigations of the atomic structure of nonequilibrium phases arising after explosive crystallization in the Fe_2Tb and CoPd nanocrystalline films show that these films have the Frank–Kasper tetrahedral close packed structure (Laves cubic phase). Such a structure [11] is characteristic of the equilibrium state of Fe_2Tb films, but it is surprising for CoPd films. An important feature of such a structure is the possibility of compression–tension of its elementary volume by 30% [12].

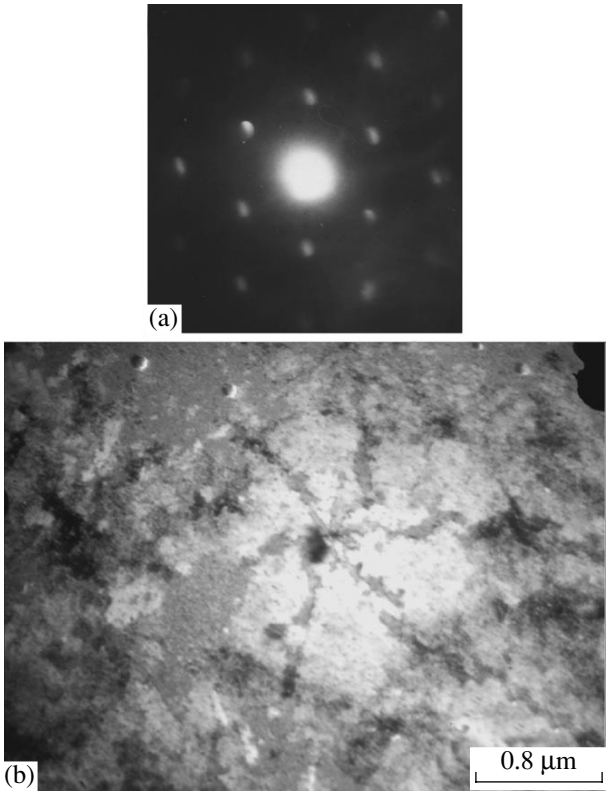

Fig. 1. (a) Electron microdiffraction pattern from a film section crystallized under the action of an electron beam at an accelerating voltage of 100 kV. (b) Microphotograph of the Fe_2Tb x-ray amorphous film with perpendicular magnetic anisotropy; diffuse dark points correspond to poles from which bending extinction contours diverge that testify to the strong internal bending of "atomic planes of the single crystal."

Crystallization may also begin in the process of sharp pressure on the sample edge in the Fe_2Tb films. Figure 2a shows an optical photograph of the Fe_2Tb x-ray amorphous film situated between crossed polarizers. The dark domain corresponds to the initial x-ray amorphous state with magnetization perpendicular to the film plane. Motley droplet-like regions are formed after crystallization initiated by the pressure of a glass cutter on the sample edge. Magnetic anisotropy in the Fe_2Tb films subjected to pressure is reoriented [13]. We attempted to find a correlation between the structural self-organization processes observed in the Fe_2Tb films and changes in their magnetic structure. Spontaneous deformation arising in nonequilibrium materials can lead to the redistribution of magnetization in local

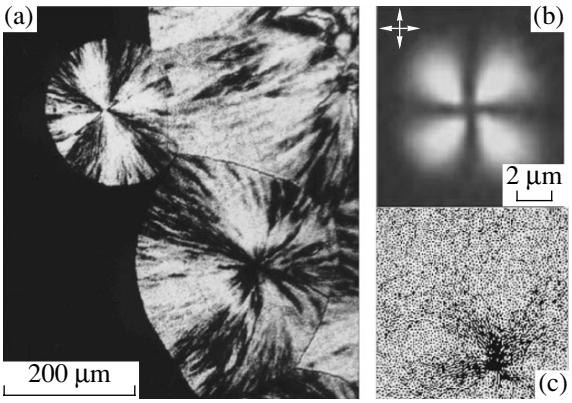

Fig. 2. (a) Optical photograph of the Fe_2Tb x-ray amorphous film situated between crossed polarizers; the dark domain corresponds to the magnetization perpendicular to the film plane. (b) Photograph of the spherical nematic droplet that was made in polarized light with crossed polarizers for the radial configuration of the director [14]. (c) Distribution of the force field for 4938 particles that is obtained by the molecular dynamics method [8].

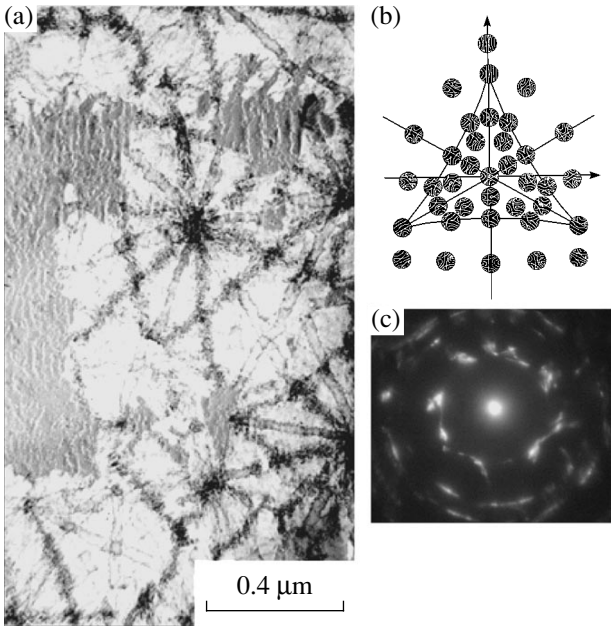

Fig. 3. (a) Microphotograph of the Co–Pd film after the electron-beam irradiation of the initial x-ray amorphous film. (b) Electron diffraction pattern from the Co–Pd sample. (c) Streamlines of a viscous liquid in the central zone of a six-roller mill [18].

domains [14]. Figure 2a shows the redistribution of magnetization in crystallized droplet-like domains.

The classification given in [15] for topologically stable defects in droplets of nematic liquid crystals indicates the radial ordering of the director with a point defect (hedgehog) in the droplet center. This property corresponds to a similar experimental observation of birefringence in crossed polarizers with a fourth order symmetry axis, which are shown in Fig. 2b.

The effective biaxiality arises in load-induced crystallization processes in the Fe_2Tb film that is deposited on a substrate and is subjected to compression–tension load. In this case, the repetition of structural units of the same type satisfies the same rules as in a liquid crystal. The initial state of the film consists of nanocrystallites with the second-order symmetry axis (the 110 orientation of the Laves cubic phase, as follows from the analysis of electron microdiffraction patterns). Owing to long-range forces acting in thin films [16], the dark and light sections on the pattern in different parts of the film are parallel to each other.

Figure 2c shows a similar distribution of stress fields that is obtained in the molecular dynamics simulation of the behavior of particles in a glass subjected to shear stress when investigating the plastic deformation of atomically disordered media [8]. Simulation was based on the STZ theory and yielded the distribution of the stress field in the figure plane. Comparison of experimental and theoretical results (see Fig. 2) shows that the distributions of stress fields at micro- and mesoscopic levels are scale-invariant.

For explosive crystallization with strong bending of the crystal lattice or plastic deformation with rotation effects, the model of super-Arrhenius relaxation is consistent with the model of the bifurcation of the atomic lattice that was proposed in catastrophe theory [17]. The symmetry of the single crystal with the sixth-order axis arises in the process of its growth under compression–tension load in the case where the film is separated from the substrate and is irradiated by an electron beam (see Fig. 1a). In this case, the initial state of the film consists of the same nanocrystallites with a second-order symmetry axis (the 110 orientation of the Laves cubic phase, as follows form analysis of the electron diffraction pattern). The direction of explosive crystallization is determined by the temperature gradient; i.e., it is directed from the center to the periphery of the circle. In this case, there is no orienting action of stresses from the substrate. However, conditions arise for the appearance of a third-order symmetry axis by analogy with the appearance of such symmetry in viscous liquid deformation geometry. Figure 3c [18] shows the streamlines of a viscous liquid in the central zone of a six-roller mill immersed in this liquid. The authors suppose the possibility of using such a model to study intermolecular interactions. In our opinion, the STZ theory provides the possibility of describing nonequilibrium processes in a disordered solid containing numerous excited atoms.

Structural elements (nanocrystallites with the second-order symmetry axis) are adaptable due to their mobility. As a result, symmetry with the sixth-order axis is efficiently generated and observed in experiment

(see Figs. 1 and 3). Such a structure is capable of reproducing itself and is an example of a dissipative structure relaxing to the equilibrium state.

In our opinion, there are sufficient reasons to conclude that the features of explosive crystallization processes in metal films with a nonequilibrium structure can be described in the framework of the modern STZ theory based on the excited-atom model.

This work was supported by the Russian Foundation for Basic Research (project no. 00-02-17358) and INTAS (grant no. 00-100).

REFERENCES

1. N. A. Bul'enkov and D. L. Tytik, Izv. Ross. Akad. Nauk, Ser. Khim., No. 1, 1 (2001).
2. V. S. Zhigalov, G. I. Frolov, and L. I. Kveglis, Fiz. Tverd. Tela (St. Petersburg) **40**, 2074 (1998) [Phys. Solid State **40**, 1878 (1998)].
3. Kazuaki Fukamichi, in *Physical Properties of Quasicrystals*, Ed. by Z. M. Stadnic (1999), Springer Ser. Solid-State Sci., Vol. 126, p. 295.
4. M. L. Falk and J. S. Langer, Phys. Rev. E **57**, 7192 (1998).
5. J. S. Langer and A. Lemaitre, cond-mat/0411038 (2004).
6. H. Z. Cummins, J. Phys.: Condens. Matter **11**, A95 (1999).
7. G. Adam and J. H. Gibbs, J. Chem. Phys. **43**, 139 (1965).
8. C. Maloney and A. Lemaitre, Phys. Rev. Lett. **93**, 195501 (2004).
9. V. Yu. Kolosov and A. R. Tholen, Acta Mater. **48**, 1829 (2000).
10. D. S. Sanditov, S. S. Badmaev, Sh. B. Tsydypov, and B. D. Sanditov, Fiz. Khim. Stekla **29**, 5 (2003) [Glass Phys. Chem. **29**, 2 (2003)].
11. L. I. Kveglis, S. M. Zharkov, and E. P. Popel, Fiz. Tverd. Tela (St. Petersburg) **44**, 1070 (2002) [Phys. Solid State **44**, 1117 (2002)].
12. W. B. Pearson, *The Crystal Chemistry and Physics of Metals and Alloys* (Wiley, New York, 1972; Mir, Moscow, 1977), Vols. 1, 2.
13. L. I. Kveglis and S. M. Zharkov, in *Abstracts of International Conference* (Krasnoyarsk, 1995), p. 172.
14. E. V. Gomonaj and V. M. Loctev, J. Phys.: Condens. Matter **14**, 3959 (2002).
15. A. V. Shabanov, V. V. Presnyakov, V. Ya. Zyryanov, *et al.*, Pis'ma Zh. Éksp. Teor. Fiz. **67**, 696 (1998) [JETP Lett. **67**, 733 (1998)].
16. B. V. Deryagin, N. V. Churaev, and V. M. Muller, *Surface Forces* (Nauka, Moscow, 1987) [in Russian].
17. J. M. T. Thompson, *Instabilities and Catastrophes in Science and Engineering* (Wiley, Chichester, England, 1982; Mir, Moscow, 1985).
18. T. Poston and I. Stewart, *Catastrophe Theory and Its Applications* (Pitman, London, 1978; Mir, Moscow, 1980).

Translated by R. Tyapaev

JETP Letters, Vol. 82, No. 1, 2005, pp. 26–29. Translated from Pis'ma v Zhurnal Éksperimental'noĭ i Teoreticheskoĭ Fiziki, Vol. 82, No. 1, 2005, pp. 27–30.

Giant Optical Nonlinearity of an Atomic Bose–Einstein Condensate and Low-Threshold Bistability

N. N. Rosanov and V. A. Smirnov

Research Institute of Laser Physics, St. Petersburg, 199034 Russia

e-mail: nrosanov@yahoo.com

Received May 11, 2004

The polarization of an atomic Bose–Einstein condensate weakly excited by laser radiation at a nearly resonance frequency is determined. The coefficient of nonlinearity (cubic in field) in the refractive index of the condensate is calculated for the slow decay mode due to the spontaneous emission of excited atoms, as well as for the stationary mode, when the loss of atoms is compensated by the injection of atoms into the trap. In both cases, the cubic nonlinearity coefficients of the condensate are several orders of magnitude larger than the corresponding values for known nonlinear media. The conditions for observing hysteresis in an interferometer containing the condensate in the stationary state in the presence of an incident laser beam are specified. © *2005 Pleiades Publishing, Inc.*

PACS numbers: 42.50.Rh, 67.40.–w

The response of an atomic Bose–Einstein condensate (BEC) to the action of laser radiation forms the basis of a number of methods of BEC analysis. In our opinion, the most interesting experimental and theoretical investigations are devoted to resonant excitation of the BEC [1–3]. However, under the conditions studied in these investigations, the action of light leads to almost complete decay of the condensate. Here, we study resonant excitation of the BEC under the conditions when the BEC changes slowly, exhibiting anomalously high optical nonlinearity.

For the case where the BEC interacts with an electromagnetic field ($Ee^{-i\omega t} + E^*e^{i\omega t}$), the equations relating the wave functions of the condensate and atoms in the excited electronic state (the material wave function $\Phi = \Phi_g e^{-iE_g t/\hbar} + \Phi_e e^{-iE_e t/\hbar}$) have the form [4–7]

$$\begin{aligned} i\hbar\partial_t\Phi_g &= -\frac{\hbar^2}{2M}\Delta\Phi_g \\ -\frac{1}{2}(ed)E^*\Phi_e e^{i\delta t} &+ \frac{4\pi\hbar^2 a}{M}|\Phi_g|^2\Phi_g, \end{aligned} \tag{1}$$

$$\begin{aligned} i\hbar\partial_t\Phi_e &= -\frac{\hbar^2}{2M}\Delta\Phi_e \\ -\frac{1}{2}(ed)E\Phi_g e^{-i\delta t} &- i\hbar\frac{\gamma}{2}\Phi_e. \end{aligned} \tag{2}$$

Here, the subscripts g and e correspond to the ground and excited states of an atom, M is the atomic mass, Δ is the Laplace operator, e is the elementary charge, d is the matrix element of the dipole moment of the atomic transition, $\delta = \omega - \omega_a$ is the laser frequency detuning from the atomic transition frequency, a is the scattering length, and γ is the spontaneous luminescence rate. At the initial time, $\Phi_e = 0$ and the normalization condition has the form $\int|\Phi_g|^2 d^3r = N$, where N is the number of atoms in the condensate.

The propagation equation for slowly varying field amplitude E in the scalar approximation has the form

$$\frac{2i\omega}{c^2}\partial_t E = -\Delta E - k^2 E - 4\pi k^2 P. \tag{3}$$

Here, k is the wavenumber of laser radiation, the linear part of the permittivity is $\varepsilon_0 \approx 1$, and polarization $P = (ed)\Phi_g^*\Phi_e e^{i\delta t}$ is introduced. The momentum k_r acquired by an atom after absorption of light is much larger than the momenta of atoms in the condensate. Consequently, in Eq. (2) we can set

$$\frac{\hbar^2}{2M}\Delta\Phi_e \approx -\frac{\hbar^2}{2M}k_r^2\Phi_e.$$

Integrating Eq. (2) with respect to time, we obtain

$$\begin{aligned} \Phi_e &= \frac{i(ed)}{2\hbar}e^{-i\delta t}\int_0^t E\Phi_g \\ &\times \exp\left[-\frac{\gamma}{2}(t-t') + i\left(\frac{\hbar k_r^2}{2M} + \delta\right)(t-t')\right]dt'. \end{aligned} \tag{4}$$

The time variation in the wave function of the condensate must be slower than its stabilization, which is determined by the time between atomic collisions ($\tau_c \approx$ 1 ms). The real part of the polarization is determined by

the imaginary part of the exponent in the integrand of expression (4). It is maximal for $\delta \sim \gamma/2$. It should be noted that the characteristic value of γ is on the order of 10^8 s^{-1}. In the case of excitation of, e.g., a lithium condensate by visible light, we have $\hbar k_r^2/2M \approx 5 \times 10^5$ s$^{-1} \ll \gamma/2$. Consequently, we can set

$$\Phi_e = \frac{\delta - i\gamma/2}{\delta^2 + \gamma^2/4}\frac{edE}{2\hbar}e^{-i\delta t}\Phi_g,$$
$$P = \frac{(ed)^2 E}{2\hbar}\frac{\delta - i\gamma/2}{\delta^2 + \gamma^2/4}|\Phi_g|^2, \quad (5)$$

and

$$i\hbar\partial_t\Phi_g = -\frac{\hbar^2}{2M}\Delta\Phi_g + \frac{\hbar}{4}\frac{\delta - i\gamma/2}{\delta^2 + \gamma^2/4}\nu_R^2\Phi_g + \frac{4\pi\hbar^2 a}{M}|\Phi_g|^2\Phi_g, \quad (6)$$

where $\nu_R = |edE|/\hbar$ is the Rabi frequency. If the laser beam width is much larger than the BEC size, the second term on the right-hand side of Eq. (6) is almost independent of coordinates. In this case, this term is responsible not only for an insignificant phase factor but also for a decrease in the wave function amplitude:

$$|\Phi_g|^2 \longrightarrow |\Phi_g|^2 \exp\left(-\frac{\gamma/2}{\delta^2 + \gamma^2/4}\frac{\nu_R^2}{2}t\right). \quad (7)$$

Then the expression for polarization includes a term cubic in the field:

$$P = \frac{(ed)^2 E}{2\hbar}\frac{\delta - i\gamma/2}{\delta^2 + \gamma^2/4}\left(1 - \frac{\nu_R^2}{2}\frac{\gamma/2}{\delta^2 + \gamma^2/4}t\right)|\Phi_g|^2. \quad (8)$$

It follows from this expression that the cubic (Kerr) nonlinearity coefficient is given by

$$\varepsilon_2 = \frac{\pi(ed)^4}{2\hbar^3}\frac{\delta\gamma}{(\delta^2 + \gamma^2/4)^2}|\Phi_g|^2 t. \quad (9)$$

This quantity is a linear function of time and its sign is determined by the sign of detuning δ. Setting $|\delta| \approx \gamma/2$, $\gamma \approx 10^8$ s^{-1}, $ed \approx 2.5 \times 10^{-18}$ CGS unit, and $|\Phi_g|^2 = N_c$ ($N_c = 10^{13}$ cm^{-3} is the atomic concentration [1]), we can estimate ε_2 as

$$\varepsilon_2 \approx 10^7 t \text{ CGS unit}. \quad (10)$$

Accordingly, the Kerr nonlinearity coefficient reaches $\varepsilon_2 \approx 10^4$ CGS unit in a stabilization time of $t = 10^{-3}$ s. However, such a giant nonlinearity is observed under the action of a very weak field. The time of condensate variation must be longer than the time of its stabilization. It follows from estimate (10) that the radiation intensity must satisfy the condition

$$|E|^2 < 10^{-7} \text{ CGS unit} \sim 2.4 \times 10^{-5} \text{ W/cm}^2. \quad (11)$$

The BEC nonlinearity determined here is essentially unsteady. To pass from the pulsed to continuous excitation, the excited atoms leaving the condensate must be compensated by their injection in the ground state. A consistent analysis of this problem requires the employment of the density matrix, because the loss and recovery of the condensate can be rigorously taken into account only in this way. For a 1D condensate [8] in the absence of spontaneous decay and atomic pumping, the following equations hold:

$$i\hbar\partial_t\Phi_g = -\frac{\hbar^2}{2M}\frac{\partial^2\Phi_g}{\partial z^2} - \frac{1}{2}(ed)E^*\Phi_e e^{i\delta t} + \frac{4\pi\hbar^2 a}{Ms}|\Phi_g|^2\Phi_g, \quad (12)$$

$$i\hbar\partial_t\Phi_e = -\frac{\hbar^2}{2M}\frac{\partial^2\Phi_e}{\partial z^2} - \frac{1}{2}(ed)E\Phi_g e^{-i\delta t}. \quad (13)$$

In this case, polarization is $P_1 = (ed)\Phi_g^*\Phi_e e^{i\delta t}/s$, where s is the cross-sectional area of the condensate. We can phenomenologically introduce dissipative terms into the set of equations for the density matrix of such a system:

$$\frac{\partial|\Phi_g|^2}{\partial t} = i\frac{ed}{2\hbar}E^*\Phi_g^*\Phi_e e^{i\delta t} + \text{c.c.} + p,$$
$$\frac{\partial|\Phi_e|^2}{\partial t} = i\frac{ed}{2\hbar}E\Phi_g\Phi_e^* e^{-i\delta t} + \text{c.c.} - \gamma|\Phi_e|^2,$$
$$\frac{\partial(\Phi_g^*\Phi_e)}{\partial t} = i\frac{ed}{2\hbar}Ee^{-i\delta t}(|\Phi_g|^2 + |\Phi_e|^2) + i\frac{4\pi\hbar a}{Ms}|\Phi_g|^2\Phi_g^*\Phi_e - \gamma_T(\Phi_g^*\Phi_e). \quad (14)$$

Here, p is the pumping rate for atoms in the BEC and γ and γ_T are the longitudinal and transverse relaxation rates, respectively, which are approximately identical. The terms containing second derivatives with respect to z are omitted in Eqs. (14), because even the recoil velocities of atoms absorbing photons, which are much higher than the velocities of atoms in the condensate, do not affect the kinetics of the interaction of the BEC with light (see above). Under steady-state conditions, we have $\partial|\Phi_g|^2/\partial t = \partial|\Phi_e|^2/\partial t = \partial P_1/\partial t = 0$. Setting

$\Phi_g^* \Phi_e = \mu e^{-i\delta t}$ in Eqs. (14), we arrive at the algebraic expressions

$$p = \gamma|\Phi_e|^2 = -i\frac{ed}{2\hbar}(E^*\mu - \text{c.c}),$$
$$\mu = -\frac{ed}{2\hbar}E(|\Phi_g|^2 - |\Phi_e|^2)/\left(\delta + \frac{4\pi\hbar a}{Ms}|\Phi_g|^2 + i\gamma_T\right). \quad (15)$$

The second term in the denominator of Eq. (15) is on the order of 10^3–10^4 $s^{-1} \ll \gamma$; consequently, we can omit this term in the subsequent analysis. It follows from Eq. (15) that

$$p = \frac{2\gamma_T}{\gamma_T^2 + \delta^2}\left(\frac{ed}{2\hbar}\right)^2|\Phi_g|^2|E|^2,$$
$$P_1 = i\frac{(ed)^2}{2\hbar}\left(1 - \frac{2\gamma_T/\gamma}{\gamma_T^2 + \delta^2}\nu_R^2\right)\frac{|\Phi_g|^2/s}{\gamma_T - i\delta}E. \quad (16)$$

The imaginary part of the polarization determines the exponential decay of the field amplitude with the decay rate

$$\alpha = \frac{\pi k(ed)^2\gamma_T}{\hbar(\gamma_T^2 + \delta^2)s}|\Phi_g|^2. \quad (17)$$

Setting $k = 1.2 \times 10^5$ cm^{-1}, $ed = 2.5 \times 10^{-18}$ CGS units, $\gamma_T = 10^8$ s^{-1}, $\delta \approx \pm\gamma_T$, and $|\Phi_g|^2/s = N_c = 10^{12}$ cm^{-3}, we obtain $\alpha = 10$ cm^{-1} ($\alpha L = 0.1$ for a condensate of length $L \sim 100$ μm). The correction to the real part of the permittivity is given by

$$\Delta\varepsilon = \Delta\varepsilon_0 + \varepsilon_2|E|^2,$$
$$\Delta\varepsilon_0 = \frac{2\pi(ed)^2\delta}{\hbar(\gamma_T^2 + \delta^2)s}|\Phi_g|^2 \approx \pm\frac{\pi(ed)^2N_c}{\hbar\gamma_T} = \pm 1.6 \times 10^{-4}, \quad (18)$$
$$\varepsilon_2 = \Delta\varepsilon_0\frac{8\pi(ed)^2}{\hbar^2(\gamma_T^2 + \delta^2)} \approx \pm 0.1 \text{ CGS unit}.$$

In this case, $\nu_R^2/\gamma_T^2 < 1$, i.e., $|E|^2 < 1.6 \times 10^{-3}$ CGS unit ~ 0.4 W/cm^2. Thus, the limiting nonlinear corrections to the permittivity of the medium in the stationary and nonstationary cases are close to each other.

An example of the application of giant optical nonlinearity of the BEC is the scheme of the Fabry–Perot interferometer (two-mirror resonator) filled with a BEC and excited by external monochromatic laser radiation with amplitude A_{in} [9, 10]. In the plane-wave approximation, setting $E = A\exp(ikz)$, where A is the field amplitude in the resonator, we can write

$$\tau A_{in} = A(1 - re^{-2\alpha L + i\theta}). \quad (19)$$

Here, τ is the amplitude transmittance of the input mirror and r is the product of the amplitude reflectivities of the two mirrors. The phase acquired by light passing in two directions in the resonator is $\theta = \theta_0 + \theta_2 I$. The detuning of θ_0 can be varied over a wide range by changing the resonator length L within a wavelength and $I = A^2$ is the intensity of light. Setting $\rho = r\exp(-2\alpha L)$ and assuming that $\theta^2 \ll 1$, we obtain

$$TI_{in} = I|1 - \rho e^{i\theta}|^2$$
$$= I\left[(1-\rho)^2 + 4\rho\sin^2\frac{\theta}{2}\right] \approx I[(1-\rho)^2 + \rho\theta^2]. \quad (20)$$

Here, $T = |\tau|^2$ is the intensity transmittance of the input mirror. Introducing $J = \theta_2 I$ and $J_{in} = T\theta_2 I_{in}$, we arrive at the relation

$$J_{in} = J[(1-\rho)^2 + \rho(\theta_0 + J)^2]. \quad (21)$$

This equation, which is cubic in J, determines the dependence of J on J_{in}. The inflection points of the corresponding hysteresis loop are defined by the equation

$$\frac{\partial J_{in}}{\partial J} = 3\rho J^2 + 4\rho\theta_0 J + [(1-\rho)^2 + \rho\theta_0^2] = 0. \quad (22)$$

This equation has real roots under the necessary condition of bistability $\theta_0^2 > 3(1-\rho)^2/\rho$. Let the resonator contain a BEC of length $L = 50$ μm. Then, $2\alpha L = 0.1$ and $|\theta_0| > 0.17$. The roots of Eq. (22) are

$$\theta_2 I_{1,2} = -\frac{2\theta_0}{3} \pm \sqrt{\left(\frac{2\theta_0}{3}\right)^2 - \frac{[(1-\rho)^2 + \rho\theta_0^2]}{3\rho}}, \quad (23)$$
$$\theta_0\theta_2 < 0.$$

The coefficient of the nonlinear phase increment for double passage through the BEC is

$$\theta_2 = \frac{8\pi\delta kL(ed)^4}{\hbar^3(\gamma_T^2 + \delta^2)^2}\frac{|\Phi_g|^2}{s} \approx \pm 10^2 \text{ CGS unit } (\delta \approx \pm\gamma_T). \quad (24)$$

Setting $\theta_0 = 0.2$, choosing a negative detuning for definiteness, and assuming that the intensity transmittance of the input mirror is $T = 0.01$ and $\rho = 0.896$, we obtain from relation (23) the switching intensities $I_{1,2} = 1.5 \times 10^{-3}$, 1.1×10^{-3} CGS unit or 0.37, 0.27 W/cm^2, respectively. The corresponding intensities of the field incident on the interferometer are $I_{in1,2} = 4.5$, 2.6 W/cm^2, respectively. In this case, the curve describing the dependence of J on J_{in} is S-shaped. As the external field intensity increases to 4.5 W/cm^2, a hysteretic jump in intensity is observed both in the resonator and in transmitted and reflected radiation. When the intensity decreases, the jump to the lower branch takes place at an intensity of 2.6 W/cm^2.

Thus, when low-intensity laser radiation propagates in the BEC, the latter behaves as a nonlinear medium with an anomalously large Kerr nonlinearity coefficient whose sign is determined by the sign of radiation frequency detuning from resonance. By optimizing the detuning, it is possible to achieve a comparatively small absorption. In contrast to a standard two-level system, spontaneous emission leads to irreversible loss of atoms from the condensate. For this reason, the BEC nonlinearity is much stronger than for all known nonlinear media, especially in the case of a slow decay of the condensate due to spontaneous emission from excited atoms. In the case of the soliton state of the BEC [8], optical nonlinearity is additionally enhanced due to the effective decrease in scattering length a. Under steady-state conditions, when spontaneous decay is compensated by material pumping, the large value of optical nonlinearity is associated with the low rate of transverse relaxation of ultracold atoms. This circumstance makes it possible to observe many nonlinear effects (including self-focusing) at rather low levels of intensity of cw laser radiation. The possibility of observing a low-threshold hysteresis when an interferometer containing a BEC is excited by a laser beam has also been demonstrated. According to the above results, transverse modulation instability, switching waves, and dissipative solitons in a wide-aperture interferometer filled with a BEC will also have a low threshold [10].

This study was supported by INTAS, grant no. 211-855.

REFERENCES

1. W. Ketterle, Usp. Fiz. Nauk **173**, 1339 (2003).
2. E. D. Trifonov, Zh. Éksp. Teor. Fiz. **120**, 1117 (2001) [JETP **93**, 969 (2001)].
3. D. Schneble, Y. Torri, M. Boyd, *et al.*, Science **300**, 475 (2003).
4. J. Javanianen, Phys. Rev. Lett. **75**, 1927 (1995).
5. G. Lens, P. Meystre, and E. M. Wright, Phys. Rev. Lett. **71**, 3271 (1993).
6. K. V. Krutitsky, F. Burgbacher, and J. Audretsch, Phys. Rev. A **59**, 1517 (1999).
7. M. Saffman and D. V. Skryabin, in *Spatial Solitons*, Ed. by S. Trillo and W. Torruellas (Springer, Berlin, 2001).
8. N. N. Rozanov, Yu. V. Rozhdestvenskiĭ, V. A. Smirnov, and S. V. Fedorov, Pis'ma Zh. Éksp. Teor. Fiz. **77**, 89 (2003) [JETP Lett. **77**, 84 (2003)].
9. H. Gibbs, *Optical Bistability: Controlling Light with Light* (Academic, New York, 1985; Mir, Moscow, 1988).
10. N. N. Rosanov, *Spatial Hysteresis and Optical Patterns* (Nauka, Moscow, 1997; Springer, Berlin, 2002).

Translated by N. Wadhwa

JETP Letters, Vol. 82, No. 1, 2005, pp. 30–33. Translated from Pis'ma v Zhurnal Éksperimental'noĭ i Teoreticheskoĭ Fiziki, Vol. 82, No. 1, 2005, pp. 31–35.

Vibrational Density of States of Hen Egg White Lysozyme

S. G. Lushnikov[1], A. V. Svanidze[1], and I. L. Sashin[2]

[1] *Ioffe Physicotechnical Institute, Russian Academy of Sciences, Politekhnicheskaya ul. 26, St. Petersburg, 194021 Russia*

[2] *Frank Laboratory of Neutron Physics, Joint Institute for Nuclear Research, Dubna, Moscow region, 141980 Russia*

Received April 4, 2005; in final form, May 12, 2005

Incoherent inelastic neutron scattering on hen egg white lysozyme has been measured at temperatures 200, 280, and 311 K. Using the experimental results, the vibrational density $G(\omega)$ of states of hen egg white lysozyme has been determined. Both the Debye regime and section of $G(\omega)$ with a spectral dimension of $\tilde{d} = 1.58$, which corresponds to the fracton regime, have been observed in the low-frequency part of the density of states for all temperatures. © *2005 Pleiades Publishing, Inc.*

PACS numbers: 61.12.Ex, 63.50.+x, 87.14.Ec, 87.15.He

At present, the vibrational spectra of macromolecules, primarily proteins, are intensively studied using optical and neutron spectroscopy [1–6], as well as numerical simulation methods [7–12]. The reason is that to understand mechanisms of the functions of proteins it is necessary also to understand not only the structure but also the dynamics of a protein molecule. It is important to analyze the low-frequency part of the vibrational spectrum of the protein molecule that reveals slow collective motions involving the entire macromolecule and ensembles of macromolecules.

At the same time, there is no commonly accepted point of view on contributions from various processes to the low-frequency part of the vibrational spectrum of proteins. Researches agree that relaxation processes, which are manifested as a relaxation mode in the inelastic scattering of light and neutrons, are substantial for energies $E < 2$ meV [2, 3, 6]. Moreover, an acoustic-like excitation that is characteristic of disordered systems (glasses, overcooled liquids, etc.) called the boson peak is observed in the light and neutron scattering spectra of a number of proteins [2, 4–6]. The boson peak is centered at about 4 meV in the vibrational spectrum of lysozyme at a temperature near 200 K. The boson peak might originate from the topological disorder of the system and is caused by scattering on delocalized low-frequency vibrations [6].

One of the characteristic features of a protein macromolecule is that it can be considered as a fractal object. Such an approach was proposed in [13] and developed in numerical simulation of the vibrational spectrum of various proteins [8, 9, 11]. If the fractal approach is applicable to the description of the properties of proteins, the vibrational spectrum necessarily contains an excitation realized on fractals, i.e., fracton (the properties of this excitation were reviewed in detail in [14]). Ben-Avraham [8] numerically determined the fractal and fracton dimensions of G-actin and attributed the features of the low-frequency dynamics of proteins to the fractality of their structure. We emphasize that experiments for revealing fractons in the vibrational spectrum of proteins have not been yet carried out.

The aim of this work is to analyze the features of the low-frequency dynamics of proteins (with lysozyme as an example) and its change with temperature using incoherent inelastic neutron scattering (IINS).

We used a 3-ml powder sample of hen egg white lysozime (Fluka), which was lyophilized before neutron scattering experiments.

The IINS spectra were obtained on an inverse-geometry KDSOG-M time-of-flight spectrometer, which was placed in the tenth channel of the IBR-2 high-flux pulsed reactor (JINR, Dubna, Russia). Measurements were carried out simultaneously for eight scattering angles (30°, 50°, 70°, 80°, 90°, 100°, 120°, and 140°) in the neutron energy-loss regime sequentially at temperatures 280, 311, and 200 K. The resolution for zero energy transfer was equal to 0.6 meV. After the subtraction of background from the sample holder and cryostat, the experimental data were processed in the single-phonon incoherent approximation. In this case, the generalized vibrational density of states was calculated by the formula

$$G(\omega) = \frac{\omega}{n(\omega)+1}\frac{\mathbf{k}_0}{\mathbf{k}_1}\frac{1}{Q^2}\left(\frac{d^2\sigma}{d\Omega d\omega'}\right)_{\text{incoh}}, \qquad (1)$$

where $\mathbf{k}_0$ and $\mathbf{k}_1$ are the wavevectors of the incident and scattered neutrons, respectively; $\mathbf{Q} = \mathbf{k}_0 - \mathbf{k}_1$; $\hbar\omega'$ is the scattered-neutron energy; $(d^2\sigma/d\Omega d\omega')_{\text{incoh}}$ is the double differential cross section for incoherent scattering; and $n(\omega)$ is the Bose–Einstein factor.

The resulting IINS spectra were analyzed in an energy transfer range of 1.5–20 meV. According to esti-

mates made in [7], the multiphonon scattering contribution is insignificant in this energy range. To analyze the low-frequency part of the density of states of lysozyme, we use the power approach, which separates the contributions from different processes. We take into account that the vibrational spectrum of lysozyme can contain a fracton whose dispersion law differs from that for phonons. From the dynamical point of view, differences in the structural properties at different scales are manifested in the existence of a certain crossover frequency ω_{co}. For frequencies $\omega \ll \omega_{co}$, the well-known Debye law is satisfied,

$$G(\omega) \propto \omega^{d-1}. \quad (2)$$

which characterizes the density of acoustic states. For frequencies $\omega \gg \omega_{co}$, the vibrational density of states of fractons is characterized by the spectral dimension $\tilde{d}$ [14, 15]:

$$G(\omega) \propto \omega^{\tilde{d}-1}. \quad (3)$$

Thus, analysis of the exponent for the low-frequency part of the vibrational density of states provides the separation of contributions from different processes.

Let us discuss the results obtained when investigating the vibrational spectrum of lysozyme by means of IINS. Figure 1 shows the generalized vibrational density of states of hen egg white lysozyme for T = 280 K in an energy range of 1.5–250.0 meV. The inset shows a low-frequency range of 1.5–25 meV in the log–log scale. The generalized density of states in a wide frequency range will be discussed elsewhere, and we here focus on the low-frequency part of $G(\omega)$. The log–log scale allows the separation of sections with different power dependences in the generalized vibrational density of states. The linear approximation of experimental points was made by the least squares method. Two sections with different power dependences, which correspond to two straight lines with different slopes in the inset in Fig. 1, are separated in $G(\omega)$. The low bound of the first section in $G(\omega)$ is attributed to the features of the experiment, and the upper bound, to deviation from linearity. Thus, the exponent is equal to 2.82 in the low-frequency range 1.5–3.5 meV of the energy transfer. A similar exponent was obtained in IINS investigations of the low-frequency part of $G(\omega)$ for lead magnoniobate relaxor ferroelectric [16]. This result is consistent with the Debye model for the density of states of acoustic modes of solid matter; i.e., $G(\omega) \propto \omega^2$ in this energy range.

The next linear section (as is clearly seen in the inset in Fig. 1) is in the transfer energy range from 7 to 14 meV. This section is characterized by an exponent of $\tilde{d}$ = 1.58. This spectral dimension corresponds to the exponent of the function $G(\omega)$ in the fracton regime of classical fractal systems [14]. Change in the boundaries of the section under consideration by ±1 meV led to change in the exponent from 1.44 to 1.65; i.e., error was

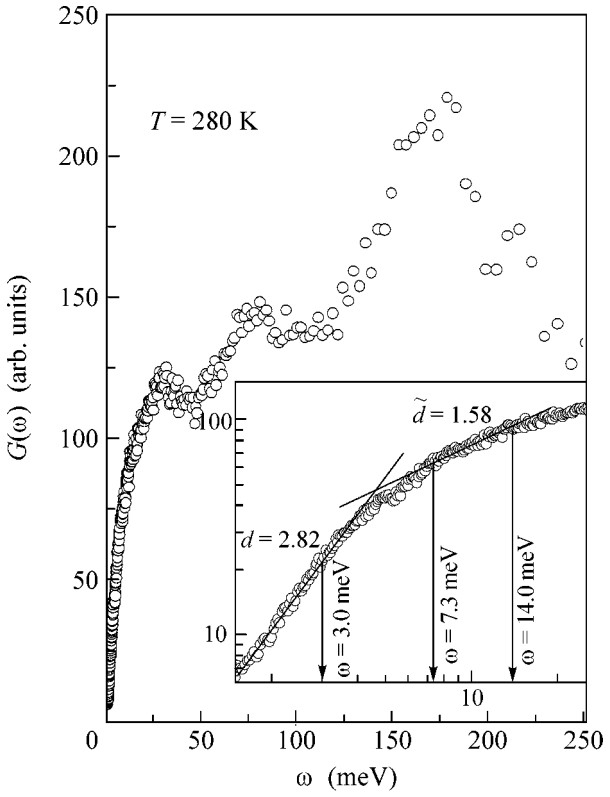

Fig. 1. Generalized vibrational density of states of hen egg white lysozyme for a temperature of 280 K. The inset is drawn in the log–log scale.

about 10% of the initial spectral dimension. The inclusion of error in the determination of boundaries does not change the fracton character of the exponent, because various estimates for the fracton dimension $\tilde{d}$ lie in the range $1 < \tilde{d} < 2$ [8, 9, 11]. The spectral dimensions $\tilde{d}$ of classical fractal objects also lie in this range [15].

We emphasize that the published data on the low-frequency Raman spectra of globular protein crystals (e.g., for lysozyme [1]) exhibit two wide peaks with maxima at frequencies ~4 and 10 meV (1 meV = 8.06 cm^{-1}) [1]. These excitations are also observed in low-frequency Raman spectra of aqua solutions of lysozyme, β lactoglobulin, and other proteins [3]. The mode centered at about 4 meV is associated in a number of works with the boson peak observed in experiments on inelastic neutron scattering at low temperatures [3, 6]. At the same time, the nature of the second (10-meV) excitation has not yet discussed.

Comparing the results of our investigations of the vibrational spectrum of lysozyme with reference data, we found that the second (10-meV) mode in the Raman spectra corresponds to the section of the generalized density of states in the energy range from 7 to 14 meV with a spectral dimension of $\tilde{d}$ = 1.58 (Fig. 1). There-

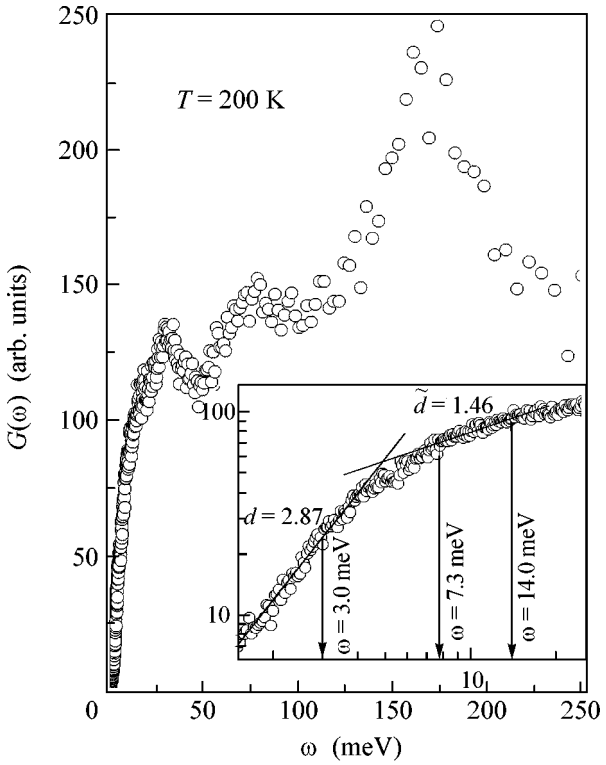

Fig. 2. Same as in Fig. 1 but for a temperature of 200 K.

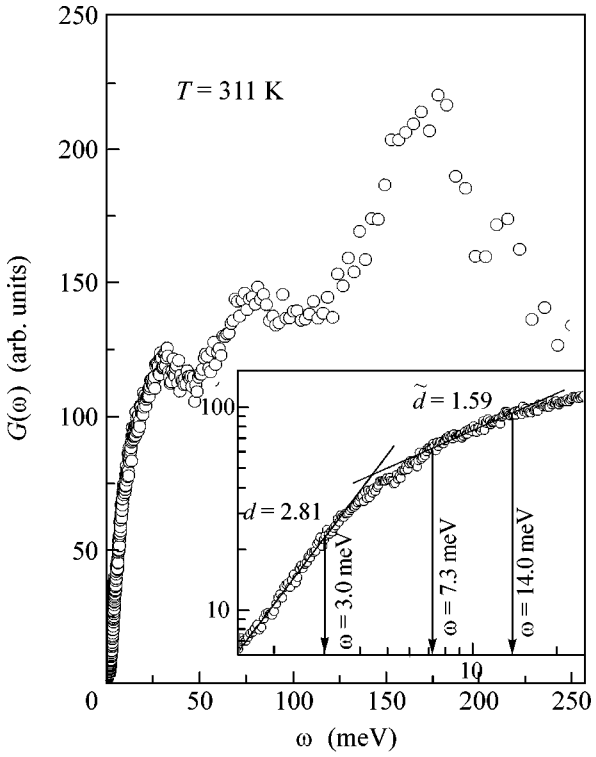

Fig. 3. Same as in Fig. 1 but for a temperature of 311 K.

fore, the 10-meV mode is likely a fracton. Using the expression $L \sim vh/E$, where $v \approx 2.3$ km/s is the speed of sound [17], h is Planck's constant, and E is the energy at which the fracton is observed, we qualitatively estimate the scale at which this excitation occurs. As a result of this calculation, we obtain $L \approx 10$ Å, whereas the sizes of a lysozyme molecule are estimated as $28.0 \times 28.0 \times 39.9$ Å [18]. Thus, the observed excitation is indeed realized at a length scale on the order of the sizes of the lysozyme macromolecule.

We point to the existence of crossover between two sections corresponding to the contributions from phonons and fractons in the vibrational density $G(\omega)$ of states. The frequency that can be taken as ω_{co} is determined from the intersection point of two straight lines of the linear approximation for the above-discussed sections of the density of states of lysozyme (at T = 280 K, $\omega_{co} \approx 4.5$ meV). The problem of crossover is a subject of special investigation and is not discussed in this paper.

Spectral dimensions of the phonon and fracton regimes for various temperatures

T, K	Phonon regime, meV	$D = d - 1$	Fracton regime, meV	$\tilde{d}$
200	1.5–3.0	2.9	7.8–14.0	1.46
280	1.5–3.0	2.8	7.3–14.0	1.58
311	1.5–3.0	2.8	7.3–14.0	1.59

To study the change in the fracton and phonon regimes with temperature, we analyze the low-frequency part of the vibrational density $G(\omega)$ of states for temperatures 280, 200, and 311 K (Figs. 1–3, respectively). We note that both phonon and fracton regimes are identified in all three cases. For temperatures 280 and 311 K, the corresponding spectral exponents d and $\tilde{d}$ are nearly unchanged (see table). For T = 200 K, certain changes are observed in $G(\omega)$ which correspond to a very small increase in the exponent d and decrease in the fracton dimension $\tilde{d}$ (Fig. 2). These changes likely occur because proteins undergo a transition to the glassy phase when temperature decreases [19].

Comparing the form of the vibrational densities of lysozyme states that were obtained in experiments for various temperatures (Figs. 1–3), we point to an additional feature of the function $G(\omega)$. The function $G(\omega)$ increases when temperature decreases, which is likely attributed to the temperature dependence of the Debye–Waller factor.

In this work, the vibrational density of states of hen egg white lysozyme has been obtained experimentally and analyzed. As a result, two power-dependence sections have been separated in the vibrational density of states. The first of these sections corresponds to the phonon regime and the second to the fracton regime.

The corresponding spectral dimensions have been determined for these regimes. Temperature changes in the vibrational density of states of lysozyme have also been investigated. It has been revealed that there are a small decrease in the fracton dimension at 200 K and an increase in the vibrational density of states with increasing temperature from 311 K through 280 K to 200 K.

We are grateful to S.N. Gvasaliya for stimulating discussions. This work was supported by the Council of the President of the Russian Federation for Support of Young Russian Scientists and Leading Scientific Schools (project no. NSh-2168.2003.2); the Russian Foundation for Basic Research (project no. 05-02-17822); and the Division of Physical Sciences, Russian Academy of Sciences.

REFERENCES

1. L. Genzel, F. Keilmann, T. P. Martin, *et al.*, Biopolymers **15**, 219 (1976); S. E. May Colaianni and O. Faurskov Nielsen, J. Mol. Struct. **347**, 267 (1995).
2. H. Leyser, W. Doster, and M. Diehl, Phys. Rev. Lett. **82**, 2987 (1999).
3. Hisako Urabe, Yoko Sugaware, Mitsuo Ataka, and Allan Rupprecht, Biophys. J. **74**, 1533 (1998); G. Galiskan, A. Kisliuk, A. M. Tsai, *et al.*, J. Chem. Phys. **118**, 4230 (2003).
4. E. Balog, T. Becker, M. Oettl, *et al.*, Phys. Rev. Lett. **93**, 028 103 (2004).
5. Gerard Giraud, Jan Karolin, and Klaas Wynne, Biophys. J. **85**, 1903 (2003).
6. J. Perez, J.-M. Zanotti, and D. Durand, Biophys. J. **77**, 454 (1999); A. R. Bizzarri, A. Paciaroni, C. Arcangeli, and S. Cannistraro, Eur. Biophys. J. **30**, 443 (2001).
7. J. Smith, S. Cusack, B. Tidor, and M. Karplus, J. Chem. Phys. **93**, 2974 (1990).
8. Daniel ben-Avraham, Phys. Rev. B **47**, 14 559 (1993).
9. M. Nollmann and P. Etchegoin, Phys. Rev. E **60**, 4593 (1999).
10. M. Tarek and D. J. Tobias, J. Chem. Phys. **115**, 1607 (2001).
11. Turkan Haliloglu, Ivet Bahar, and Burak Erman, Phys. Rev. Lett. **79**, 3090 (1997).
12. N. Rathore, T. A. Knotts IV, and J. J. de Poblo, J. Chem. Phys. **118**, 4285 (2003).
13. J. S. Helman, Antonio Coniglio, and Constantino Tsallis, Phys. Rev. Lett. **53**, 1195 (1984).
14. Tsuneyoshi Nakayama, Kousuke Yakubo, and Raymond L. Orbach, Rev. Mod. Phys. **66**, 381 (1994).
15. R. Vacher, E. Courtens, and J. Pelous, Recherche **21**, 426 (1990).
16. S. N. Gvasaliya, S. G. Lushnikov, I. L. Sashin, and I. G. Siniĭ, Kristallografiya **44**, 284 (1999) [Crystallogr. Rep. **44**, 250 (1999)].
17. S. Speziale, F. Jiang, C. L. Caylor, *et al.*, Biophys. J. **88**, 3202 (2003).
18. Arunan Nadarajah and Marc L. Pusey, Acta Crystallogr. D **52**, 983 (1996).
19. I. E. Iben, D. Braunstein, W. Doster, *et al.*, Phys. Rev. Lett. **62**, 1916 (1989).

Translated by R. Tyapaev

JETP Letters, Vol. 82, No. 1, 2005, pp. 34–38. From Pis'ma v Zhurnal Éksperimental'noĭ i Teoreticheskoĭ Fiziki, Vol. 82, No. 1, 2005, pp. 36–40.

Magnetic Phase Transitions in $TbNi_5$ Single Crystal: Bulk Properties and Neutron Diffraction Studies¶

S. Lee[1], A. A. Podlesnyak[2], K. Prokes[3], V. E. Sikolenko[3], A. S. Ermolenko[4], E. G. Gerasimov[4], Yu. A. Dorofeev[4], A. P. Vokhmyanin[4], J.-G. Park[1, 5], and A. N. Pirogov[1, 4]

[1] *Department of Physics, Institute of Basic Science, SungKyunKwan University, Suwon 440-746, South Korea*
[2] *Laboratory for Neutron Scattering, ETH Zurich & Paul Scherrer Institute, Villigen, 5232 PSI, Switzerland*
[3] *BENSC, Hahn-Meitner Institute, Berlin D-14109, Germany*
[4] *Institute of Metal Physics, Russian Academy of Sciences, Yekaterinburg, 620219 Russia*
[5] *Center for Strongly Correlated Materials Research, Seoul National University, Seoul 151-742, South Korea*
Received May 23, 2005

Magnetic susceptibility, heat capacity, and neutron diffraction measurements have been carried out in order to study the unusual magnetic ordering of $TbNi_5$ using a single crystal over the temperature region of 2–30 K. Two spontaneous magnetic transitions have been observed: one is a second-order transition from a paramagnetic state to an incommensurate structure (T_p = 24 K), and the other, a first-order transition from the incommensurate structure to a lock-in phase (T_f^c = 10 K). We also found an irreversible magnetic field–induced transition from the modulated structure to the ferromagnetic collinear one. © *2005 Pleiades Publishing, Inc.*

PACS numbers: 75.25.+z, 75.30.Kz, 61.12.–q

1. INTRODUCTION

The exchange interaction and crystal field splitting of rare-earth intermetallic RNi_5 compounds have been the subject of great interest, largely because of their simple crystal and magnetic structures. Their magnetic properties are determined mainly by rare-earth ions [1]. The rare-earth elements occupy 1a positions of the $CaCu_5$-type lattice (space group *P*6/*mmm*), and their magnetic moment values are found to be close to that of free rare-earth ions. The Ni atoms occupy 2b and 3d positions with ordered magnetic moments less than 0.2 μ_B. Most of these RNi_5 intermetallics have been studied in detail by various experimental methods. In particular, $TbNi_5$ has been extensively studied using several experimental techniques: magnetic measurements [2], heat-capacity measurements [3], elastic and inelastic neutron scattering [4–6], positive μSR spectroscopy [7], and spin–echo NMR [8] studies. The results of these investigations appeared to be in good agreement with the ferromagnetic model of the magnetic structure, and there seemed to be no reason whatsoever to suspect otherwise until quite recently.

However, recent electrical resistance [9], ac susceptibility, and magnetization [10, 11] data indicated that the magnetic state of $TbNi_5$ might be more subtle than the proposed simple ferromagnetic structure. According to [9], the resistance, when measured along the *a* axis (the magnetic easy direction), exhibits characteristic behavior for a ferromagnet with Curie temperature T_C = 23 K, while that measured along the *c* axis (the magnetic hard direction) shows an anomalous peak below T_C: these peaks were observed at 17.4 and 21.2 K for cooling and heating curves, respectively. The authors of [10, 11] also observed anomalies in the temperature and field dependence of their ac susceptibility. For example, the temperature dependence of the ac susceptibility shows two peaks, namely, at T_f = 16.5 K and T_p = 23.5 K. The authors of [11] then proposed that the $TbNi_5$ compound is a helimagnetic antiferromagnet between T_f and T_p under an external magnetic field smaller than H_c = 0.45 kOe and becomes ferromagnetic for $T < T_p$ with increasing field above H_c.

In order to understand the true nature of the magnetic transitions of $TbNi_5$, we have recently performed a high-resolution powder neutron diffraction study of $TbNi_5$ and found new magnetic satellites, which were not seen previously and which we interpreted as evidence of a modulated magnetic structure [12]. We have described our new results in terms of a fanlike structure with two wave vectors ($\mathbf{k}_1 = 0$ and $\mathbf{k}_2 \approx (2\pi/c)(0, 0, 0.019)$). In this model, the magnetic moments of Tb ions have mutually orthogonal ferromagnetic (μ_f) and modulated (μ_{mod}) basal-plane components. The magnetic satellites of our neutron diffraction pattern were observed over the whole temperature region of 2–23 K, in contrast with the original explanation of [11]. Moreover, we did not observe a clear anomaly in the temperature dependence of the intensities of both ferromag-

¶ This article was submitted by the authors in English.

netic peaks and satellites at 16.5 K, where a ferromagnet–helimagnet transition is expected to occur according to [10, 11]. It should also be mentioned that, in our previous studies [12], we did not investigate the effects of an external magnetic field on the magnetic structure of $TbNi_5$, although the field dependence of the magnetic structure may be important in better understanding the experimental observations of [10, 11].

Although our previous high-resolution powder diffraction studies elucidated some interesting aspects of the magnetic transition, in order to have full understanding of it, we need additional detailed and careful studies of the magnetic structure of $TbNi_5$ using a single-crystal sample and, especially, of its field dependence. Therefore, we have performed neutron diffraction experiments on a $TbNi_5$ single crystal at temperatures of 2–30 K under magnetic fields. The measurements were carried out while both heating and cooling. In addition, we made ac susceptibility, magnetization, and heat-capacity measurements in order to compare the bulk properties of our single crystal with the results published earlier [9–11].

2. EXPERIMENTAL DETAILS

Our $TbNi_5$ alloy was prepared from high-purity starting materials in an induction furnace using an Al_2O_3 crucible under argon atmosphere. Subsequent heat treatment of the alloy was made at 1100°C for 8 h. The single crystal was then cut out from a grain of an ingot and, subsequently, ground to a sphere approximately 2 mm in diameter. The remaining part of the ingot was used for heat-capacity measurements and powder X-ray diffraction studies to confirm the single-phase structure of the $CaCu_5$ type. The lattice parameters were determined to be a = 4.8986(4) and c = 3.9606(4) Å at room temperature.

Rocking curves (ω scans) around the (100), (001), (101), and (002) reflections were measured with the double-axis E-4 diffractometer at the BENSC, Hahn-Meitner Institute. The incident neutron wavelength was 2.44 Å. The (002) reflection with a large nuclear intensity was used for an intermittent check of the orientation of the sample while varying the temperature and/or the magnetic field. A horizontal magnetic field was applied along the a or c axes. The data analysis was done using the FULLPROF package [13].

The magnetization and ac susceptibility of the single crystal were taken by using a SQUID magnetometer at the Institute of Metal Physics of the Russian Academy of Sciences. The ac susceptibility was measured in an alternating field of 10 Oe at a frequency of 90 Hz. The specific heat was studied by a PMC device at the Paul Scherrer Institute.

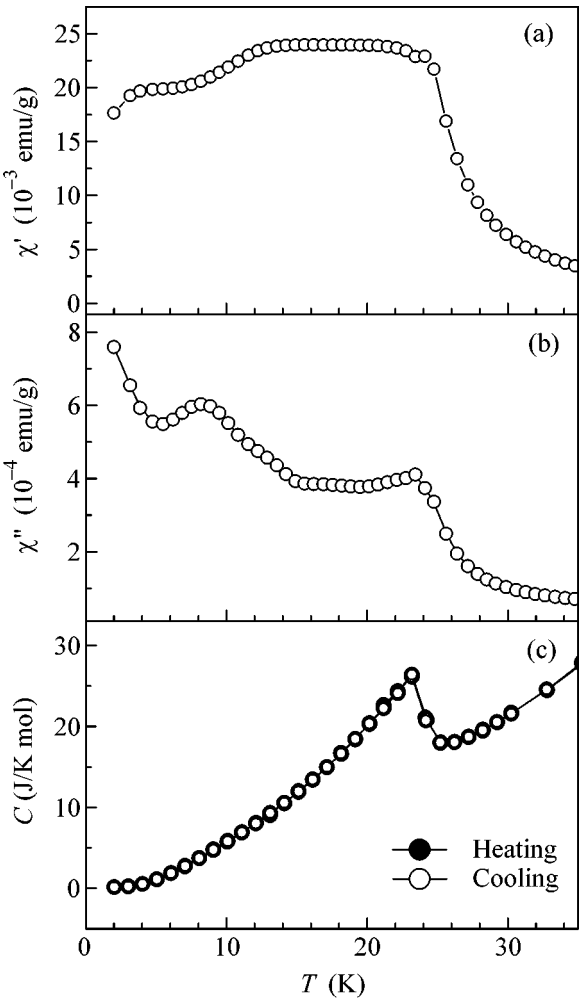

Fig. 1. Temperature dependence of (a) real and (b) imaginary parts of ac susceptibility and (c) heat capacity, measured while heating (closed symbols) and cooling (open symbols).

3. EXPERIMENTAL RESULTS AND DISCUSSION

Figure 1 shows the thermal variation of the real and imaginary parts of the ac susceptibility measured with a field parallel to the a axis of the $TbNi_5$ single crystal. The temperature dependence of the heat capacity is also presented in Fig. 1c for both cooling and heating curves. All of the data exhibit a distinct maximum at $T \approx 23$ K, which evidences an order–disorder transition. On the other hand, we note that the imaginary susceptibility has another anomaly at $T \approx 8$ K.

Figure 2 shows the neutron diffraction data scanned around the (001) reflection while cooling from room temperature to 2 K. The (001) reflection is a pure nuclear peak at temperatures above 25 K. The magnetic contributions to the (001) reflection and the $(001)^{\pm}$ magnetic satellites begin to appear at T_p = 24 K, and

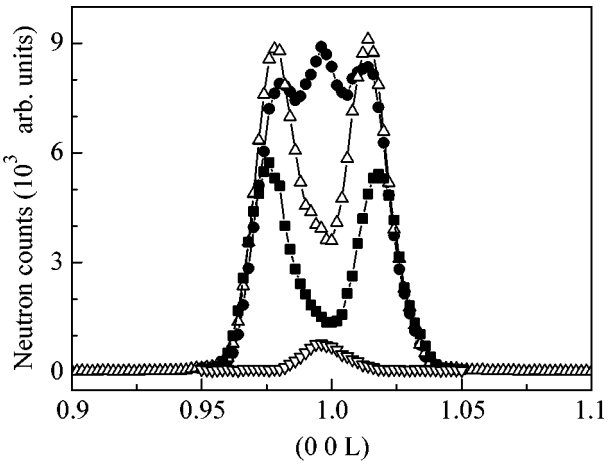

Fig. 2. Neutron diffraction spectra around the (001) reflection scanning along the [00L] direction taken at (●) 1.7, (△) 10.0, (■) 20.1, and (▽) 25.1 K while cooling.

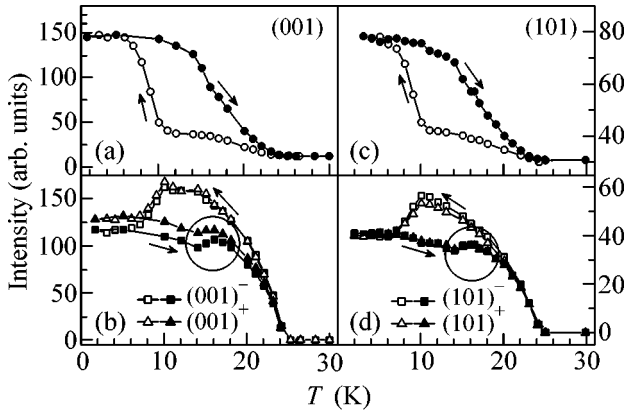

Fig. 3. Temperature dependence of the integrated intensities of (a) (001) and (c) (101) reflections and (b) $(001)^{\pm}$ and (d) $(101)^{\pm}$ satellites. Open and closed symbols are for data taken while cooling and heating, respectively. Squares and triangles are for minus and plus satellites, respectively.

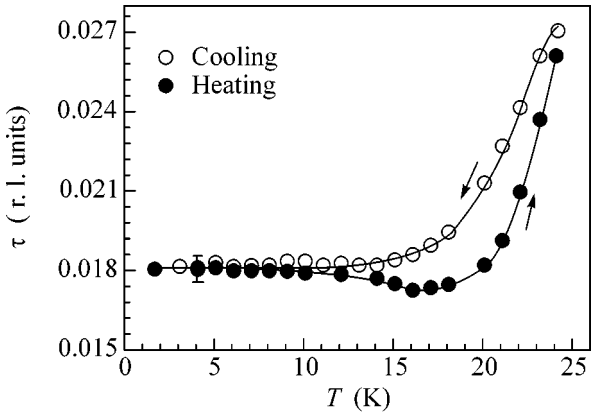

Fig. 4. Temperature dependence of the wave vector $\mathbf{k}_2$.

their intensities increase upon cooling down to $T_f^c \approx 10$ K. A further cooling to 7 K produces a sharp increase of the (001) reflection intensity and simultaneous decrease of both satellites. This behavior is clearly seen from the temperature dependence of the integrated intensities of the (001) reflection and the $(001)^{\pm}$ satellites shown in Fig. 3. Similar curves were also obtained for the (100) and (101) reflections, as well as for their $(100)^{\pm}$ and $(101)^{\pm}$ satellites.

Upon heating, there is a relatively slow decrease in the intensities of the (100), (001), (101) reflections and $(100)^{\pm}$, $(001)^{\pm}$, $(101)^{\pm}$ satellites over the region of 2.2–14 K before they all decrease sharply at temperatures of 16–23 K (see Fig. 3). However, the main reflections and satellites exhibit different behavior over the temperature region of 14–16 K: the main reflections decrease continuously with temperature, while the satellites increase slightly, as marked by the circles in Figs. 3b and 3d. A comparison of the heating and cooling curves of the intensities clearly shows the existence of large thermal hysteresis.

A similar hysteresis is also observed in the temperature dependence of the wave vector $\mathbf{k}_2$. We determined $\mathbf{k}_2$ from the distance between the positions of $(101)^{\pm}$ satellites, and the results are presented in Fig. 4. As one can see in the figure, the $\mathbf{k}_2$ vector has different values for the heating and cooling curves at $T > 10$ K. Below 10 K, the wave vector becomes almost the same for both curves within the resolutions of our experiments with $\mathbf{k}_2 \approx (2\pi/c)0.0181$, indicating that a lock-in transition occurs at $T \simeq 10$ K.

Thus, the $TbNi_5$ compound undergoes two magnetic transitions. One is the order–disorder type transition at $T_p = (24 \pm 1)$ K for both cooling and heating. When the temperature decreases, a low-temperature transition is observed at $T_f^c \approx 10$ K as a sharp change in the intensities of the main reflections and satellites. One of the features of this low-temperature transition is the large thermal hysteresis, evidence of the first-order transition. Taking into account the temperature dependence of the $\mathbf{k}_2$ vector below 10 K, we speculate that a lock-in structure occurs at $T < 10$ K; its wave vector is estimated to be $\mathbf{k}_2 \approx (2\pi/c)0.0181 \approx 1/55$ rlu (reciprocal lattice units) below 10 K.

We believe that the most probable source of the transition at T_f^c is the magnetic anisotropy of Tb ions. When the temperature decreases, the magnetic anisotropy increases and tends to orient the magnetic moments of Tb ions along the easy direction (the *a* axis). This causes an increase in the *a* axis ferromagnetic component (μ_f, parallel to the *a* axis) and, simultaneously, a decrease in the modulated one (μ_{mod}, perpendicular to the *a* axis) over the temperature interval of 7–10 K. The changes of μ_f and μ_{mod} below 10 K are calculated from the (101) reflection intensity, and we

have obtained $\Delta\mu_f = 1.9\mu_B$ and $\Delta\mu_{mod} = -1.3\mu_B$, respectively. The value of the total magnetic moment of a Tb ion remains almost the same, as expected in this temperature range.

Another feature of the low-temperature transition is the absence of a clear anomaly in the thermal variation of the heat capacity at T_f^c (see Fig. 1). Similar behavior was previously found in the cooling measurements of some RGa_2 compounds [14]. An absence of such a peak in the heat capacity data implies that there is a very small difference between the free energies of the two magnetic phases above and below T_f^c. In such a case, one can expect that a small magnetic field can transform the modulated phase into the ferromagnetic one.

In fact, this is exactly what we found in our field measurements. Figure 5 shows the scans measured around the (101) reflection under magnetic fields. Magnetic fields were applied along the *a* axis at 2 K. It is clearly seen in Fig. 5 that the magnetic field suppresses the satellites significantly and induces a collinear ferromagnetic state at $\mu_0 H_c \approx 3.5$ kOe. Interestingly enough, with increasing magnetic field, not the position but the intensity of the satellite peaks changes. It should be mentioned as well that the induced ferromagnetic state remains stable even when the external field is switched off (see Fig. 6). As one can see from the insert of Fig. 6, the Tb-ion magnetic moment reaches the value of $\mu_f = 7.3 \pm 0.1\mu_B$ at the field-induced ferromagnetic state. This value is in good agreement with the results of the magnetic measurements. However, the critical field value H_c determined by us is larger by a factor of 8 than that found in [11]. It is not clear to us at the moment what causes such a big difference in the two estimates of H_c values.

The aforementioned increase of the (101) reflection intensity by an external field is an expected and natural result, because a magnetic field was applied along the easy magnetization direction. What is surprising, however, is that the intensity increases even when a magnetic field is applied along the hard magnetization direction (i.e., the *c* axis). This is clearly seen from the bottom part of Fig. 6, where the field dependence of the (101) reflection and $(101)^{\pm}$ are presented for field applied to the *c* axis at 10 K. In a simple case, the (101) intensity should decrease with increasing field along the *c* axis, because the field tends to rotate a magnetic moment to the *c* axis and, therefore, decreases a moment projected onto the scattering plane. In our case, the (101) intensity increases when a field increases to the maximal value of 10 kOe. Furthermore, the field-induced magnetic state remains stable even after the fields were switched off. Thus, an external field for any direction transforms the modulated magnetic structure to the collinear ferromagnetic one, which is very unusual.

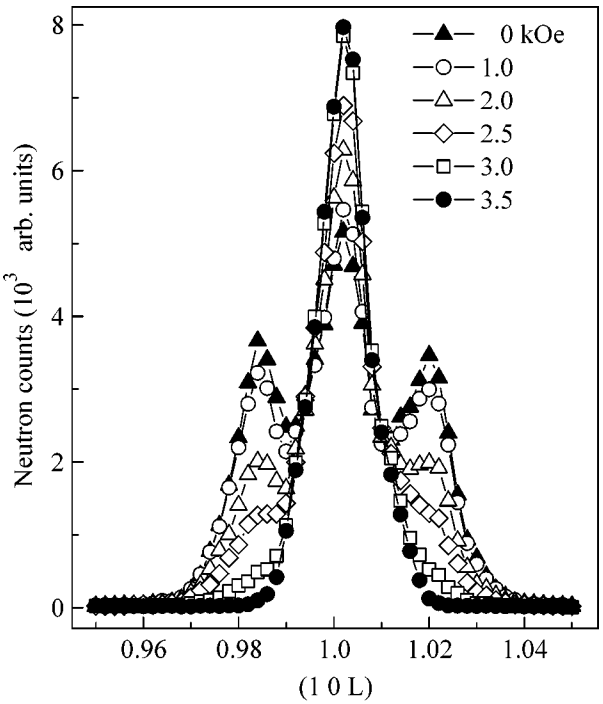

Fig. 5. Neutron spectra around the (101) reflection scanning along the [00L] direction at 2 K by varying magnetic fields.

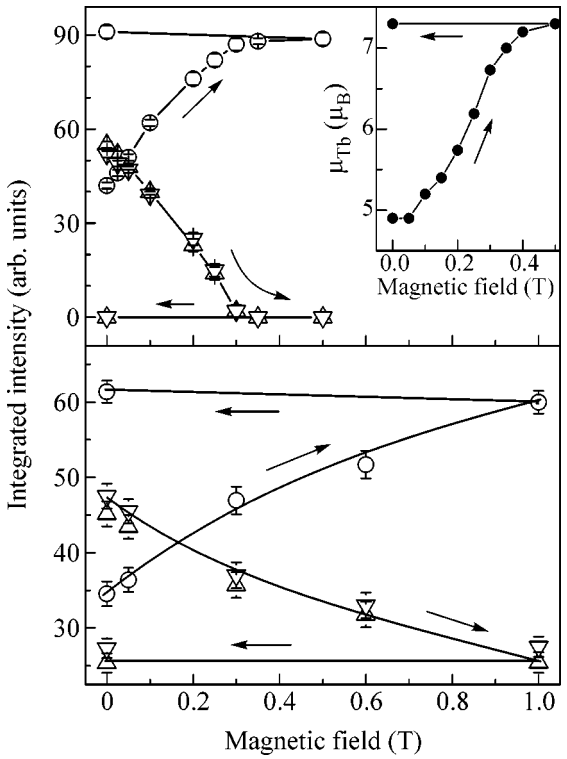

Fig. 6. Field dependence of the integrated intensities of the (101) reflection (circles) and $(101)^{\pm}$ satellites (up and down triangles) at (top) 2 K and (bottom) 10 K. The field was applied along the *a* axis at 2 K and along the *c* axis at 10 K. The insert shows the field dependence of the ferromagnetic component of the Tb-ion magnetic moment obtained at 2 K.

Taking into account our data, we can now understand the as yet unexplained results of μSR measurements [7]. It was found that the temperature dependence of a damping rate exhibits a jump near 15 K when a crystal was heated. Our results presented here indicate that the decrease in the ferromagnetic component may cause the observed jump in the μSR damping rate.

4. CONCLUSIONS

On the basis of our results, we can conclude that two spontaneous transitions occur in the $TbNi_5$ compound. One (T_p = 24 K) is the second-order transition from the paramagnetic state to the incommensurate structure. Another one (T_f^c = 10 K) is the first-order transition from the incommensurate structure to the lock-in structure. The external magnetic field of $\mu_0 H_c \approx 3.5$ kOe is enough to irreversibly transform the modulated structure into the collinear ferromagnetic one. All of these results indicate that the modulated structure is weakly stable against a magnetic field.

We are grateful for the hospitality at BENSC HMI. Financial support was provided by the Russian Foundation for Basic Research (project no. Ural 04-02-96082p2004). A.N.P. acknowledges the support of the CSCMR through the SRC program of KOSEF of Korea. Work at SungKyunKwan University was supported by the CNRF project of the KAERI.

REFERENCES

1. J. J. France and R. J. Radwanski, in *Ferromagnetic Materials*, Ed. by K. H. J. Buschow (North-Holland, Amsterdam, 1993), Vol. 7, p. 307.
2. D. Gignoux, A. Nait-Saada, and R. Perrier de la Bäthie, J. Phys. C5 **40**, 188 (1979).
3. P. Svoboda, J. Vejpravova, N.-T. H. Kim-Ngan, and F. Kaysel, J. Magn. Magn. Mater. **272–276**, 595 (2004).
4. R. Lemaire and D. Paccard, C. R. Acad. Sci., Paris **270**, 1131 (1970).
5. E. A. Goremychkin, E. Muehle, P. G. Ivanitskii, *et al.*, Phys. Status Solidi B **121**, 623 (1984).
6. D. Gignoux and J. J. Rhyne, J. Magn. Magn. Mater. **54–57**, 1267 (1986).
7. P. Dalmas de Réotier, A. Yaouanc, P. C. M. Gubbens, *et al.*, J. Magn. Magn. Mater. **104–107**, 1267 (1992).
8. C. Carboni, D. Gignoux, and A. Tari, Phys. Rev. B **52**, 9486 (1995).
9. J. A. Blanco, D. Gignoux, D. Schmitt, *et al.*, J. Phys.: Condens. Matter **6**, 4335 (1994).
10. V. M. T. Barthem and E. A. M. da Gamma, J. Phys.: Condens. Matter **9**, 7609 (1997).
11. V. M. T. Barthem, H. S. Amorim, D. Schmit, and D. Gignoux, J. Magn. Magn. Mater. **208**, 97 (2000).
12. Seongsu Lee, A. N. Pirogov, J.-G. Park, *et al.*, Europhys. Lett. **63**, 350 (2003).
13. J. Rodriguez-Carvajal, Physica B (Amsterdam) **192**, 55 (1993).
14. A. R. Ball, D. Gignoux, and D. Schmitt, J. Magn. Magn. Mater. **119**, 96 (1993).

JETP Letters, Vol. 82, No. 1, 2005, pp. 39–43. From Pis'ma v Zhurnal Éksperimental'noĭ i Teoreticheskoĭ Fiziki, Vol. 82, No. 1, 2005, pp. 41–45.

Ground-State Properties of a One-Dimensional System of Dipoles¶

A. S. Arkhipov[1], G. E. Astrakharchik[1, 2], A. V. Belikov[1], and Yu. E. Lozovik[1]

[1] *Institute of Spectroscopy, Russian Academy of Sciences, Troitsk, Moscow region, 142190 Russia*

[2] *Dipartimento di Fisica, Universitá di Trento, and BEC–INFM, I-38050 Povo, Italy*

e-mail: lozovik@isan.troitsk.ru

Received May 30, 2005

A one-dimensional (1D) Bose system with dipole–dipole repulsion is studied at zero temperature by means of a quantum Monte Carlo method. It is shown that, in the limit of small linear density, the *bosonic* system of dipole moments acquires many properties of a system of noninteracting *fermions.* At larger linear densities, a variational Monte Carlo calculation suggests a crossover from a liquidlike to a solidlike state. The system is superfluid on the liquidlike side of the crossover and is normal deep on the solidlike side. Energy and structural functions are presented for a wide range of densities. Possible realizations of the model are 1D Bose atomic systems, with permanent dipoles or dipoles induced by static field or resonance radiation; or indirect excitons in coupled quantum wires; etc. We propose parameters of a possible experiment and discuss manifestations of the zero-temperature quantum crossover. © *2005 Pleiades Publishing, Inc.*

PACS numbers: 61.20.Ja, 64.30.+t, 67.40.Hf, 68.65.La

Up until now, Bose–Einstein condensation has been realized in many different atom and molecule species with short-range interactions. At low temperatures, such an interaction can be described by an *s*-wave scattering length and is commonly approximated by a contact pseudopotential. In contrast, some recent work has focused on the realization of dipole condensates [1–5]. In these systems, the dipole–dipole interaction extends to much larger distances, and significant differences in the properties (such as the phase diagram and correlation functions) are expected. Another appealing aspect of a system of dipole moments is the relative ease of tuning the effective strength of interactions [6], which makes the system highly controllable. Dipole particles are also considered to be a promising candidate for the implementation of quantum-computing schemes [7–9].

On the theoretical side, dipole condensates have been mainly studied on a semiclassical (Gross–Pitaevskii) [10] or Bogoliubov [11] level. A model Bose–Hubbard Hamiltonian has been used to describe a dipole gas in optical lattices, and a rich phase diagram was found [5, 12]. So far, there have been no full quantum microscopic computations of the properties of a homogeneous system.

Recently, the Monte Carlo method was used to study helium and molecular hydrogen in nanotubes [13]. Such a geometry, which is effectively one-dimensional, leads to completely different properties compared to a three-dimensional sample.

We consider N repulsive dipole moments of mass M located on a line. The Hamiltonian of such a system is given by

$$\hat{H} = -\frac{\hbar^2}{2M}\sum_{i=1}^{N}\frac{\partial^2}{\partial z_i^2} + \frac{C_{dd}}{4\pi}\sum_{i<j}\frac{1}{|z_i - z_j|^3}. \qquad (1)$$

We keep in mind two different possible realizations.

(i) Cold bosonic atoms, with induced or static dipole momenta, in a transverse trap so tight that excitations of the levels of the transverse confinement are not possible and the system is dynamically one-dimensional (1D). The dipoles themselves can be either induced or permanent. In the case of dipoles induced by an electric field E, the coupling has the form $C_{dd} = E^2\alpha^2$, where α is the static polarizability. For permanent magnetic dipoles aligned by an external magnetic field, one has $C_{dd} = m^2$, where m is the magnetic dipole moment. The interaction between the atoms, apart from the dipole forces, contains a short-range scattering part that is conveniently described by the *s*-wave scattering length a. Usually, this contribution is large compared to the dipole force, but recent progress in applying Feshbach resonance techniques to tune a, and even to make it zero, opens exciting prospects of obtaining a system with purely dipole–dipole interactions. The strength of the effective coupling C_{dd} can be tuned by changing the electric field in the case of induced dipoles, and the special technique of fast rotation of the electric or magnetic field can be applied to permanent dipoles [6].

(ii) Spatially indirect excitons in two coupled quantum wires. A quantum wire is a semiconductor nano-

¶ This article was submitted by the authors in English.

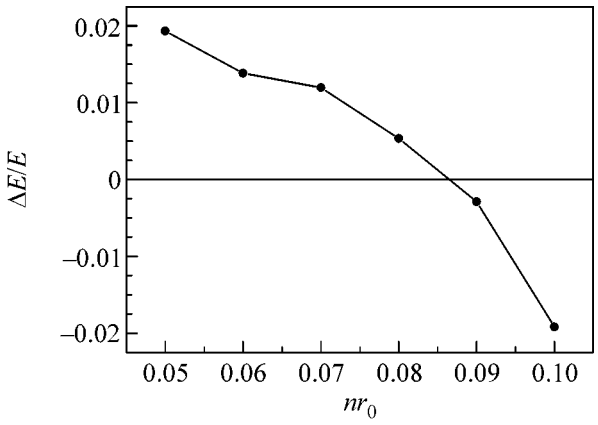

Fig. 1. Difference between energy calculated using liquidlike and solidlike wavefunctions $(E_{\text{solid}} - E_{\text{liquid}})/E$ as a function of the dimensionless density.

structure where an electron or a hole is allowed to move only in one direction and excitations of the transverse quantization levels are negligible. In two parallel quantum wires, one containing only holes and the other only electrons, holes and electrons couple, forming indirect excitons. If such a system is dilute enough, it constitutes a 1D set of dipoles. In this case, $C_{dd} = e^2D^2/\varepsilon$, where e is an electron charge, ε is the dielectric constant of the semiconductor, and D is the distance between the centers of the quantum wires. This system is the 1D counterpart of the 2D indirect exciton system in coupled quantum wells, which was extensively studied both theoretically [5, 14–17] and experimentally [18]. The properties of 1D and 2D systems differ essentially (see below about the Tonks–Girardeau regime, etc.); thus, an experimental study of the 1D system is of great importance.

Hamiltonian (1) can be written in dimensionless form by expressing all distances $\tilde{z} = z/r_0$ in units of $r_0 = MC_{dd}/2\pi\hbar^2$ and energies in units of $\mathscr{E}_0 = \hbar^2/Mr_0^2$. All properties of such a system are defined by the dimensionless parameter nr_0, with $n = N/L$ being the linear density and L the size of the system.

Our aim is to determine the ground-state energy in a wide range of densities and to check the evidence of a possible quantum crossover. In order to define the structural properties, we calculate the pair distribution function (PDF). In terms of the many-body ground-state wavefunction of the system Ψ_0, the PDF is written as

$$g_2(|z_1 - z_2|) = \frac{N(N-1)}{n^2}\frac{\int|\Psi_0(z_1, \ldots, z_N)|^2 dz_3 \ldots dz_N}{\int|\Psi_0(z_1, \ldots, z_N)|^2 dz_1 \ldots dz_N}. \quad (2)$$

The static structure factor is directly related to the pair distribution function:

$$S(k) = 1 + n\int e^{ikz}[g_2(z) - 1]dz. \quad (3)$$

The technique of Bragg scattering provides access to the static structure factor in experiments on bosonic atoms. For the system of indirect excitons, measurements of the spatial structure of photoluminescence can give information about possible crystallization, etc.

We apply the diffusion Monte Carlo (DMC) method, which is one of the most efficient theoretical tools for investigating the zero-temperature properties of quantum systems [19]. We choose the many-body guiding trial wavefunction Ψ_T in the Bijl–Jastrow form consisting of one- and two-body terms:

$$\Psi_T(z_1, \ldots, z_N) = \prod_{i=1}^{N} f_1(z_i)\prod_{j<k} f_2(|z_j - z_k|). \quad (4)$$

To describe the liquidlike side of the crossover, it is sufficient to have only the term describing pair correlations. We choose it in the form $f_2(|z|) = \exp\{-[A/(n|z|)]^B\}$, where A and B are variational parameters that we optimize by minimizing variational energy via carrying out a variational Monte Carlo (VMC) calculation. As will be discussed below, in the low-density limit, the wavefunction asymptotically approaches the Tonks–Girardeau gas wavefunction $f_2^{TG}(|z|) = |\sin(\pi z/L)|$ [20, 21]. We checked that, in this regime, there is no large difference between using $f_2^{TG}(|z|)$ and $f_2(|z|)$ even on a variational level. Thus, our choice of a two-body term is well suited to describing a liquid even in the strong mean-field regime (see [21]).

We account for the spatial quasicrystalline order by considering Gaussians with width C for each particle near a corresponding lattice site $f_1(z_i) = \exp\{-[n(z_i - z_i^c)]^2/2C^2\}$. The sites z_i^c are equally spaced by a distance n^{-1}, and the variational parameter C is defined by VMC optimization. For the simulation at high density, we keep the same type of two-body term f_2 as on the liquidlike side of the crossover, although the values of the optimal parameters may differ.

In Fig. 1, we show a comparison of the VMC energy of the liquidlike and solidlike wavefunctions in the $nr_0 = 0.01$–0.1 density range. In this region, the optimal parameters are $A = 1.6$, $B = 0.4$, and $C = 1.16$. We discover that, for densities smaller than $n_c \approx 0.085r_0^{-1}$, the liquidlike wave function description is energetically favorable, although, at larger densities, the ground state of the system is better described by a solidlike *ansatz*. Contrary to 3D and 2D liquid–solid phase transitions, the energetic difference in a 1D system is very small. This suggests that the transition in a 1D system at zero temperature is of a crossover type.

At a very small density, one expects the following: (i) in the process of two-body collisions, particles always get reflected back due to the repulsive interaction, which is very intense at short distances; (ii) particles stay far apart most of the time, so that the potential energy of the interaction is small compared to the kinetic energy. From the above, it follows that the system is equivalent to a gas of impenetrable bosons (Tonks–Girardeau gas). It was shown in [20] that the wavefunction of such a Bose system can be mapped onto the wavefunction of a system of noninteracting spinless *fermions*. The bosonic system acquires many fermionlike properties (fermionization): the energy is the Fermi energy $E^{TG}/N = \mathscr{E}_0\pi^2(nr_0)^2/6$, and the pair distribution function exhibits Friedel-like oscillations $g_2^{TG}(z) = 1 - \sin^2(\pi nz)/(\pi nz)^2$.

We present the dependence of the energy per particle on the density in Fig. 2. At small density $nr_0 \ll 1$, the energy is the same as that of the Tonks–Girardeau gas E^{TG}, which signals fermionization of the system in this regime. At large density, the particles are localized at lattice sites, with the potential energy $E^{\text{str.int}}/N = \mathscr{E}_0\zeta(3)(nr_0)^3$ being dominant. In this regime, the density dependence of the energy is very strong. Indeed, it is cubic, in contrast to the linear dependence on the mean field for the pseudopotential interaction and the quadratic dependence for an exactly solvable model with a $1/z^2$ interaction [22]. This strong dependence comes from the diverging short-range behavior of the dipole–dipole interaction. Although, in 3D, the dipole–dipole interaction is long-range, this is no longer true in the 1D case (see, for example, [23]), and no special techniques like Ewald summation are required.

We studied the dependence of the energy on the size of the system. The energy has two contributions: one coming from summation over pairs separated by a distance smaller than $L/2$ (this contribution is a direct output of the Monte Carlo calculation) and a tail energy, which is estimated by approximating the density at $L/2$ by the asymptotic bulk value. We find that the energy per particle as a function of the system size quickly saturates to its thermodynamic value and the results obtained for $N = 50, 100, 200$ particles agree within the statistical accuracy present in our calculation. We also find that the "tail energy" contribution is smaller than 0.2% of the total energy. All reported results are obtained using $N = 100$ particles.

The pair distribution function (Eq. (2)) is presented in Fig. 3 for a range of densities covering all the regions of interest. In a dilute system, we find that amplitude of the oscillation decays rapidly, which is characteristic for a liquid. In particular, at the density $nr_0 = 10^{-3}$, it is almost impossible to distinguish the pair distribution function from that of spinless fermions, which is in agreement with the arguments given above. By increasing the density, the oscillation becomes more pronounced. Around the critical density $n_c r_0 \approx 0.08$, we enter the solidlike side of the crossover. Further, at larger densities $nr_0 = 1, 10$, we see manifestations of the localization of particles near lattice sites.

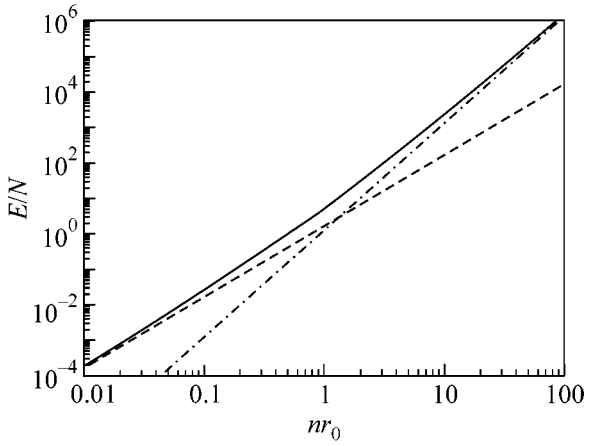

Fig. 2. Energy per particle as a function of the dimensionless density (solid line), energy E^{TG} of the Tonks–Girardeau limit (dashed line), potential energy in the strongly interacting limit (dash–dotted line). Everything is measured in units of $\hbar^2/mr_0^2$.

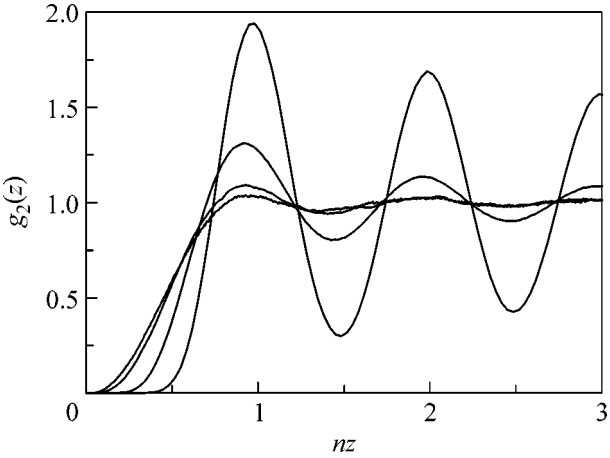

Fig. 3. Pair distribution function (2) obtained from a DMC calculation for densities $nr_0 = 10^{-3}$, 0.1, 1, 10 (larger densities have higher peaks).

By performing Fourier transformation (3), we obtain the static structure factor from the pair distribution function. Knowledge of $S(k)$ is of high importance, as it can be accessed experimentally by using Bragg spectrometry. At small densities, the low-momentum region has a linear form that is related to the speed of sound c by the Feynman relation $S(k) = \hbar|k|/2Mc$. In particular, in the Tonks–Girardeau limit, the static structure factor takes an extremely simple form: the linear growth matches the asymptotic constant at the wave vector $|k| = 2\pi n$. Increasing the density leads to the for-

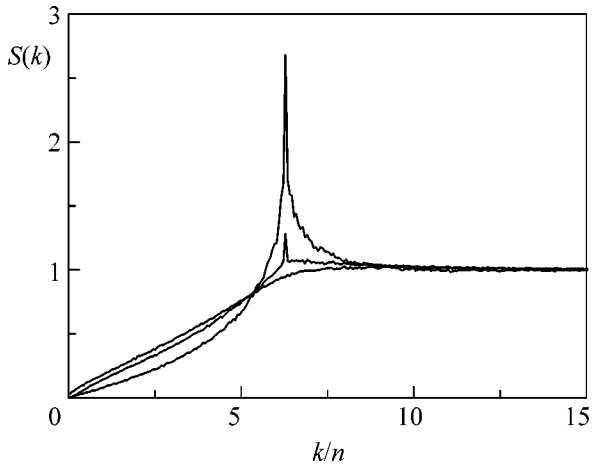

Fig. 4. Static structure factor obtained from a DMC calculation for densities $nr_0 = 10^{-3}$, 0.1, 1. A higher first peak corresponds to a higher density.

mation of a peak structure. The presence of the peak in the $S(k)$ is a consequence of the dipole–dipole interaction, as the peak is absent in a system with only *s*-wave scattering [24]. In the regime of large density, we see several peaks at integer multiples of $2\pi n$.

In order to test the superfluidity of the system, we use the winding-number technique [25]. The superfluid fraction is given by the ratio of the imaginary time diffusion constants of the center of mass and of a free particle [26]. In contrast to the calculation of the energy, here the symmetry of the trial wavefunction is crucial. We restore symmetry in the trial wavefunction in the solidlike region by performing a summation over all sites $f_1(z_i) = \sum_j \exp\{-[n(z_i - z_j^c)]^2/2C^2\}$. We see negligible differences in the energy (similar to that found in ^{4}He simulations [27]), which justifies our previous choice of Ψ_T. We find that the system is superfluid on the liquidlike side of the crossover and is normal deep on the solidlike side.

We argue that the critical densities of the quantum crossover can be readily reached in experiments with interacting indirect excitons in two quantum wires. Let us take the GaAs parameters ($\varepsilon = 12.5$, electronic mass $m_e = 0.07m_0$, hole mass $m_h = 0.15m_0$, with m_0 being the free electron mass) for reference. Then, the mass of an exciton is $0.22m_0$. Using quantum wires with a separation between their axes, D, equal to 5 nm, we obtain $r_0 \approx 10^{-6}$ cm and $\mathscr{E}_0 \approx 3$ meV. Then, the dimensionless density $nr_0 = 0.08$–0.09 corresponds to an achievable linear excitonic density $n \approx 10^5$ cm^{-1}. The liquidlike and solidlike regions and the crossover between them should be realized by changing the density of excitons in the quantum wires.

Interactions between chromium atoms can be efficiently tuned as proposed in [6]. Chromium has the advantage of having a large permanent magnetic moment compared to the other alkali atoms. Research into achieving Bose condensation in chromium is now a hot topic [1–4]. In permanent dipole chromium atoms, the ratio between the strength C_{dd} of the dipole–dipole interaction and the *s*-wave coupling constant is 0.27 for ^{52}Cr. Manipulation of induced electric dipoles is more difficult; although, in such a system, a ratio of the order of 10^2 can be reached, leading to the realization of an almost pure dipole system.

In conclusion, we have investigated the ground-state properties of a system of dipole moments by means of a quantum Monte Carlo method. We have found the presence of a quantum crossover: at small linear densities nr_0, the system stays liquidlike and superfluid, although, in a more compressed system, the solidlike description is energetically favorable. We have calculated the experimentally accessible pair distribution function and the static structure factor for a wide range of densities. In the dilute limit, this bosonic system becomes similar to a system of spinless fermions (fermionization), and the properties of the system are those of a Tonks–Girardeau gas. On the liquidlike side of the crossover, the system is superfluid, although it is normal deep on the solid side.

Finally, we have pointed out that the critical density of the quantum crossover can be achieved in current experiments with interacting excitons in wires and have proposed the parameters of a possible experimental setup.

We would like to thank F. Pederiva for useful discussions. G.E.A. acknowledges support by MIUR. Yu.E.L. is grateful to INTAS and the Russian Foundation for Basic Research for support. We thank B. Jackson for reading the manuscript.

REFERENCES

1. P. O. Schmidt, S. Hensler, J. Werner, *et al.*, Phys. Rev. Lett. **91**, 193201 (2003).
2. J. M. Doyle, R. deCarvalho, C. I. Hancox, and J. M. Doyle, Phys. Rev. A **65**, 021604 (2002).
3. J. Stuhler, P. O. Schmidt, S. Hensler, *et al.*, Phys. Rev. A **64**, 031405 (2001).
4. C. C. Bradley *et al.*, Phys. Rev. A **61**, 053407 (2000).
5. Yu. E. Lozovik, S. Y. Volkov, and M. Willander, JETP Lett. **79**, 473 (2004); Yu. E. Lozovik, S. A. Verzakov, and M. Willander, Phys. Lett. A **260**, 405 (1999); A. I. Belousov, S. A. Verzakov, and Yu. E. Lozovik, Zh. Éksp. Teor. Fiz. **114**, 322 (1998) [JETP **86**, 146 (1998)].
6. S. Giovanazzi, A. Görlitz, and T. Pfau, Phys. Rev. Lett. **89**, 130401 (2002).
7. D. Jaksch, J. I. Cirac, P. Zoller, *et al.*, Phys. Rev. Lett. **85**, 2208 (2000).
8. G. K. Brennen, I. H. Deutsch, and C. J. Williams, Phys. Rev. A **65**, 022313 (2002).
9. D. DeMille, Phys. Rev. Lett. **88**, 067901 (2002).
10. P. M. Lushnikov, Phys. Rev. A **66**, 051601 (2002).

11. D. H. J. O'Dell, S. Giovanazzi, and C. Eberlein, Phys. Rev. Lett. **92**, 250 401 (2004).
12. K. Göral, L. Santos, and M. Lewenstein, Phys. Rev. Lett. **88**, 170406 (2002); M. Baranov, L. Dobrek, K. Goral, *et al.*, Phys. Scr. **102**, 74 (2002).
13. E. Krotscheck and M. D. Miller, Phys. Rev. B **60**, 13038 (1999); M. C. Gordillo, J. Boronat, and J. Casulleras, Phys. Rev. B **61**, R878 (2000); M. C. Gordillo, J. Boronat, and J. Casulleras, Phys. Rev. Lett. **85**, 2348 (2000).
14. O. L. Berman, Yu. E. Lozovik, D. W. Snoke, and R. D. Coalson, Phys. Rev. B **70**, 235310 (2004); Yu. E. Lozovik, I. V. Ovchinnikov, R. P. Ostroumov, and K. L. Wang, Phys. Status Solidi B **241**, 85 (2004); Yu. E. Lozovik, I. V. Ovchinnikov, and V. A. Sharapov, JETP **98**, 582 (2004); Yu. E. Lozovik, O. L. Berman, and V. G. Tsvetus, Phys. Rev. B **59**, 5627 (1999); Yu. E. Lozovik and O. K. Berman, JETP Lett. **64**, 573 (1996); Yu. E. Lozovik, O. L. Berman, and A. M. Ruvinskii, JETP Lett. **69**, 616 (1999); Yu. E. Lozovik and A. V. Poushnov, Phys. Lett. A **228**, 399 (1997); Yu. E. Lozovik, O. L. Berman, and M. Willander, J. Phys. C **14**, 12457 (2002).
15. Yu. E. Lozovik and V. I. Yudson, JETP Lett. **22**, 11 (1975); Sov. Phys. JETP **44**, 389 (1976); Solid State Commun. **21**, 211 (1977); Physica A (Amsterdam) **93**, 493 (1978).
16. Xu. Zhu, P. B. Littlewood, M. S. Hybertsen, and T. M. Rice, Phys. Rev. Lett. **74**, 1633 (1995); S. Conti, G. Vignale, and A. H. MacDonald, Phys. Rev. B **57**, R6846 (1998); M. A. Olivares-Robles and S. E. Ulloa, Phys. Rev. B **64**, 115 302 (2001).
17. S. De Palo, F. Rapisauda, and G. Senatore, Phys. Rev. Lett. **88**, 206401 (2002).
18. A. A. Dremin, V. B. Timofeev, A. V. Larionov, *et al.*, JETP Lett. **76**, 450 (2002); R. Rapaport, G. Chen, D. Snoke, *et al.*, Phys. Rev. Lett. **92**, 117405 (2004); L. V. Butov, L. S. Levitov, A. V. Mintsev, *et al.*, Phys. Rev. Lett. **92**, 117404 (2004); V. V. Krivolapchuk, E. S. Moskalenko, and A. L. Zhmodikov, Phys. Rev. B **64**, 045313 (2001).
19. For details on the DMC method see, for example, J. Boronat and J. Casulleras, Phys. Rev. B **49**, 8920 (1994).
20. M. Girardeau, J. Math. Phys. **1**, 516 (1960).
21. G. E. Astrakharchik and S. Giorgini, Phys. Rev. A **66**, 053614 (2002).
22. B. Sutherland, J. Math. Phys. **12**, 246 (1971); F. Calogero, J. Math. Phys. **10**, 2191 (1969); J. Math. Phys. **10**, 2197 (1969).
23. *Dynamics and Thermodynamics of Systems with Long-Range Interactions*, Ed. by T. Dauxois, S. Ruffo, E. Arimondo, and M. Wilkens (Springer, Berlin, 2002).
24. E. H. Lieb and W. Liniger, Phys. Rev. **130**, 1605 (1963).
25. E. L. Pollock and D. M. Ceperley, Phys. Rev. B **36**, 8343 (1987); S. Zhang, N. Kawashima, J. Carlson, and J. E. Gubernatis, Phys. Rev. Lett. **74**, 1500 (1995).
26. G. E. Astrakharchik, J. Boronat, J. Casulleras, and S. Giorgini, Phys. Rev. A **66**, 023603 (2002).
27. D. M. Ceperley and M. H. Kalos, in *Monte Carlo Methods in Statistical Physics*, Ed. by K. Binder (Springer, Berlin, 1979; Mir, Moscow, 1982).

JETP Letters, Vol. 82, No. 1, 2005, pp. 44–48. Translated from Pis'ma v Zhurnal Éksperimental'noĭ i Teoreticheskoĭ Fiziki, Vol. 82, No. 1, 2005, pp. 46–51.

Atomic Structure of GaAs(001)-c(8 × 2) and Adsorption Sites of Iodine Atoms at Low Coverage

A. A. Vedeneev and K. N. Eltsov

Natural Science Research Center, Prokhorov Institute of General Physics, Russian Academy of Sciences, Moscow, 119991 Russia

e-mail: eltsov@kapella.gpi.ru

Received May 31, 2005

Atomically resolved scanning tunneling microscopy images observed by us correspond to the ζ model of GaAs(001)-c(8 × 2) atomic structure. At low coverage (θ < 0.1), iodine atoms occupy sites above vacation rows between arsenic atoms located in the upper layer. *© 2005 Pleiades Publishing, Inc.*

PACS numbers: 07.79.Cz, 68.35.Bs, 68.47.Fg, 71.55.Eq

Atomic scale study of polar (001) and (111) GaAs faces is difficult because there are no ultrahigh vacuum (UHV) methods to prepare the surface with the desired enrichment and reconstruction. This is usually done in molecular beam epitaxy (MBE) facilities, where the molecular fluxes of gallium and arsenic can be controlled to form GaAs surfaces of required atomic structure. Standard ion bombardment followed by annealing does not solve the problem because for a binary compound, the surface is always enriched with only one component—gallium for GaAs(001). UHV studies [1, 2] of the effect of molecular halogens on GaAs(001) showed that iodine could be used to create an arsenic-rich surface because at low temperatures (240–300°C) [2] iodine helps to selectively remove the upper layer of gallium atoms (without affecting arsenic atoms) from the initial GaAs(001)-c(8 × 2). In this case, the surface is not etched because the adsorption of iodine stops as a monolayer is saturated [1, 2].

Deep insight into the initial GaAs(001)-c(8 × 2) surface is critical for a successful and detailed study of iodine interaction with GaAs(001), notably the determination of the adsorption sites and the atomic structure of the adsorbate layer. Experimental data for the surface—first of all, scanning tunneling microscopy (STM) images—do not correspond to models usually applied to arsenic-rich GaAs(001) with the similar atomic structure c(2 × 8). The recent study [3] proposed and theoretically substantiated a ζ model for GaAs(001)-c(8 × 2) (Fig. 1) and presented calculated STM images for filled and empty states on the surface with certain features observed in earlier experiments [4–6]. High-quality STM images of empty states obtained later in [7] matched well those calculated in [3].

The main goal of this work was to determine adsorption sites for iodine atoms on GaAs(001)-c(8 × 2) at low coverage. In the only two STM studies of the initial stages of halogen (chlorine) adsorption on this surface [8, 9] that we are aware of, the β2 model [10] was used, within which iodine atoms were shown to adsorb on gallium dimers. Later calculations of adsorption energy for chlorine within the ζ model [11] confirmed that most energy-favorable adsorption sites for chlorine are gallium dimers (*D*), with gallium atoms in the sp^2 state (*p*) being slightly less favorable. As will be shown below, the experimental data presented in this work disprove the conclusions made in [8, 9, 11].

Experiments were performed in a multichamber ultrahigh vacuum setup equipped with a cylindrical

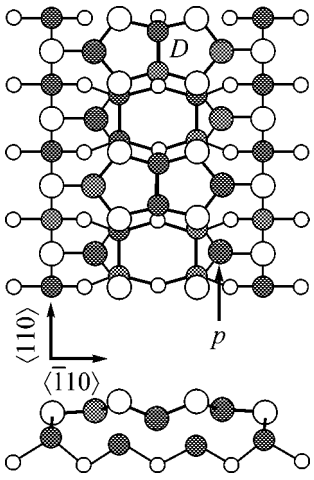

Fig. 1. Scheme of the ζ model describing the atomic structure of GaAs(001)-c(8 × 2) [3]. Two (4 × 2) cells are shown. The c(8 × 2) structure can be obtained by translating a (4 × 2) cell in the ⟨1̄10⟩ direction with a simultaneous shift by a_{GaAs} (4.0 Å) along the ⟨110⟩ direction. Large filled (unfilled) circles designate Ga (As) atoms of the upper layer, respectively; small filled (unfilled) circles designate Ga (As) atoms of the lower layers, respectively.

0021-3640/05/8201-0044$26.00

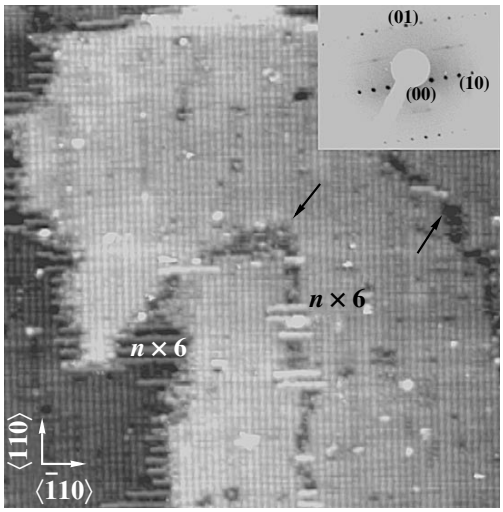

Fig. 2. Panoramic STM image of clean GaAs(001)-c(8 × 2) (1200 × 1200 Å, sample voltage U_s = +3 V, the tunnel current I_t = 0.8 nA). Arrows show the boundaries of the c(8 × 2) domains. An arsenic-rich ($n \times 6$) structure is observed at the edges of atomic steps and at domain boundaries. The inset shows a low-energy electron diffraction pattern recorded at E_p = 65 eV.

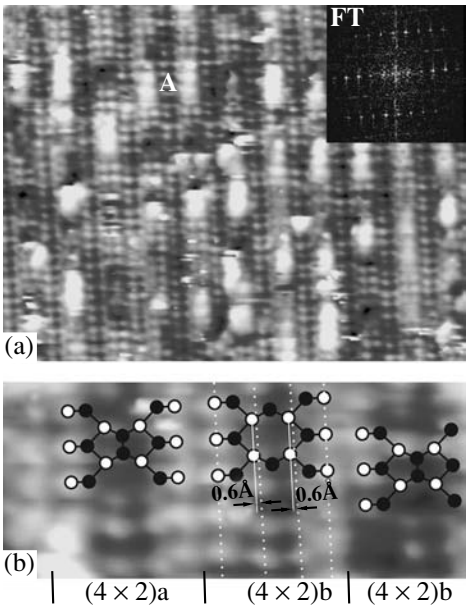

Fig. 3. (a) Atomically resolved STM image (180 × 140 Å), U_s = –2.7 V, I_t = 0.08 nA, filled electron states) of GaAs(001)-c(8 × 2) covered by iodine atoms (θ ≈ 0.05). The inset shows a Fourier transform (FT) of the STM image that matches well the diffraction pattern in Fig. 2; (b) fragment of the STM image superposed on the atomic structure of the upper layer in the ζ model. The "|" signs indicate the boundaries of the (4 × 2)a and (4 × 2)b structures. Dashed lines are drawn through atomic arsenic rows.

mirror analyzer for Auger electron spectroscopy (Riber OPC 100), a quadrupole mass spectrometer (Riber QMM-17), three-grid optics for low energy electron diffraction (LEED) (VG RVL/17), a scanning tunneling microscope (Sigma Scan GPI-300), and a gas inlet system with computer-driven piezoceramic leak valves. The base pressure in the system did not exceed 1×10^{-10} Torr. The $5 \times 5 \times 0.5$ mm samples were cut out of an *n*-type epiready GaAs(001) wafer (Si, 7×10^{17} cm^{-3}; the disorientation angle was less than 0.5°). Programmed heating was performed to remove oxides after the sample was placed in vacuum. After the removal of gallium oxide (Ga_2O) as a sharp peak in the thermal desorption spectrum at $T \approx 590$°C, a small amount of carbon remained on the surface and was detected in the Auger spectrum. Complete surface cleaning was achieved by Ar^+ ion etching (400 eV); the crystal structure was rebuilt by annealing at $T \approx 550$°C. This allowed us to obtain high-quality c(8 × 2) LEED patterns and STM images with 1000–2000 Å atomic terraces (Fig. 2). Molecular iodine was inlet into the analytical chamber containing Auger and mass spectrometers through a capillary at 22 mm from the sample surface. The pressure of molecular iodine in the beam near the surface was about 10^{-8} Torr.

The gas was introduced, and the elemental composition and the surface structure were analyzed, at room temperature. Ga $M_{2,3}M_{4,5}M_{4,5}$ (55 eV), As $M_{4,5}VV$ (31 eV), and I $M_{4,5}VV$ (510 eV) lines were analyzed in the Auger spectra. All the presented STM images were obtained at constant tunnel current. Temperature drift distortions of the STM images were restored as described in [12] and by comparing the Fourier transforms of atomically resolved STM frames with LEED patterns. The initial calibration of the scanner was also performed using the procedure mentioned above [12]. STM tips obtained by overetching in an electrochemical cell were cleaned and sharpened in an Ar^+ ion beam (Riber CI-10, 600 eV, 5 μA, 60 min) directly in the vacuum system [13]. After each series of measurements, the surface was restored by means of ion etching (400 eV) followed by annealing (550°C).

Figure 3a shows an STM image of GaAs(001)-c(8 × 2) for the filled electron states localized on arsenic atoms [3] at small iodine coverage. The coverage θ measured by the intensity of the Auger I $M_{4,5}VV$ peak (the saturation of the peak intensity corresponds to a (1 × 1) iodine atomic lattice) did not exceed 5% of the monolayer (θ < 0.05). The Fourier transform (FT) of the STM image is shown in the inset. Remarkably, the FT image matches well the LEED pattern in Fig. 2. In Fig. 3, the atomic structure of the substrate—the arrangement of arsenic atoms on the surface—is shown as an alternating pattern in which different intensities of pairs of twin stripes correspond to two different arrangements of arsenic atoms in the upper layer in the ζ model with respect to their positions in the bulk GaAs lattice (see Fig. 1). The FT image distinctly shows double atomic periodicity in the ⟨110⟩ direction, demonstrating the

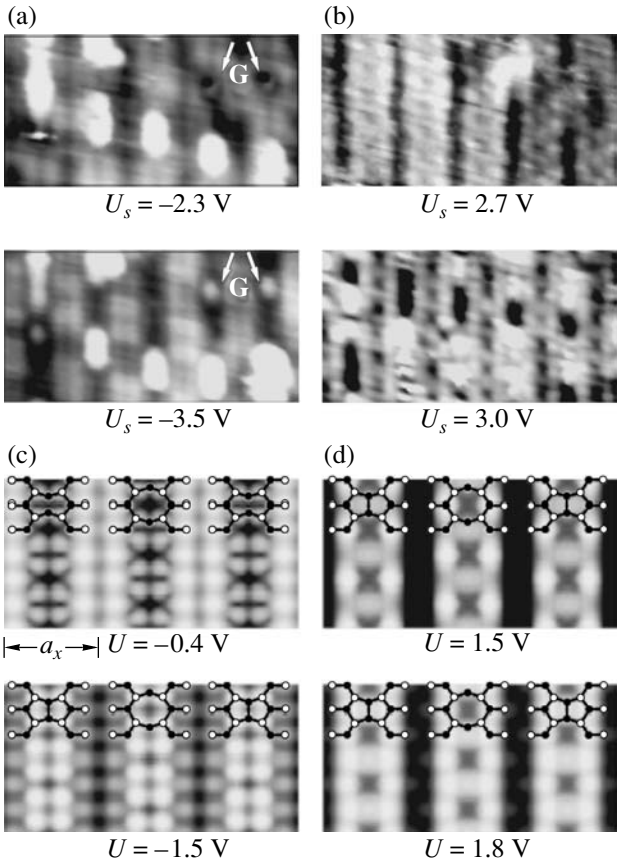

Fig. 4. (a, b) Experimental and (c, d) calculated [3] STM images of the (a, c) filled and (b, d) empty states of GaAs(001)-c(8 × 2). (a) Iodinated surface (θ ≈ 0.05); (b) U_S = +2.7 V, clean surface; U_S = +3.0 V, θ ≈ 0.07. The sample voltages indicated in (c) and (d) are referenced to the valence band top.

asymmetry in the positions of arsenic atoms around a row of gallium dimers in the upper atomic layer in the ζ model (see Fig. 1). The spots in the LEED and FT images, corresponding to the (8 × 2) periodicity, are much weaker than the (4 × 1) spots. This leads us to believe that a structure with period $4a_{GaAs}$ (a_{GaAs} = 4.0 Å) in the $\langle \bar{1}10 \rangle$ direction [14] is the basic one. Detailed analysis of the structure is possible if a fragment of this image is superposed on the scheme of the ζ model, as shown in Fig. 3b. First, one can see in the STM image that the rows with double atomic periodicity along the row correspond to the rows of arsenic atoms with a row of gallium dimers inside. This unambiguously identifies more intensive twin atomic rows with single atomic periodicity (4.0 Å) along the ⟨110⟩ direction as the rows of arsenic atoms with a vacation row in between (see Fig. 1). Second, (4 × 2) cells are indeed the main element of the structure; they can statistically form surface areas with the c(8 × 2) structure. In Fig. 3b, to distinguish between two types of domains, we introduced (4 × 2)a and (4 × 2)b cells, one shifted relative to the other by one atomic distance along the ⟨110⟩ direction. When the cells of both types are arranged periodically along the $\langle \bar{1}10 \rangle$ direction, the structure formed is usually identified as c(8 × 2). Third, it is clear that the atomic rows of arsenic with a row of gallium dimers inside are shifted along the $\langle \bar{1}10 \rangle$ direction from the positions specified in the ζ model. The measured displacements were 0.60 ± 0.25 Å. This asymmetry is apparently due to the asymmetric position of rows of gallium dimers between rows of gallium atoms (*p*-position) presented in Fig. 4b and in images obtained by other authors [4–7]. The asymmetry might be related to the interaction of gallium dimers in the upper atomic layer with the underlying atoms, which is not taken into account in the ζ model.

Let us determine the adsorption sites of iodine atoms on GaAs(001)-c(8 × 2). As is seen in Fig. 3, bright atomic-size features are observed in more intensive arsenic rows with a vacation row inside. We identified these features as iodine atoms, because their number correlates with the intensity of an iodine Auger peak, which proves that iodine atoms are adsorbed above vacation rows and occupy positions between arsenic atoms. As a rule, iodine atoms seem "smeared" along the atomic rows of the substrate, which is apparently due to the motion of iodine atoms along channels formed by arsenic atoms. This motion corresponds to STM tip motion (horizontal scan from left to right, frame scan from bottom to top). It is seen that atoms can occupy quantized states in the process of motion (for example, the iodine atoms marked "A" in Fig. 3a). Taking into account that the dangling bonds of arsenic atoms are filled [3, 11], the high electron density above these atoms could lead to a situation typical for a metal surface on which the most favorable adsorption sites are fully symmetric positions between substrate atoms.

To see the surface (atomic) structure of GaAs(001)-c(8 × 2) in more detail, we found STM imaging conditions for (U_s) in which all the features calculated according to the ζ model [3] could be observed. We present the results in Figs. 4a and 4b, and the STM images calculated in [3] in Figs. 4c and 4d, to demonstrate that all calculated features were observed in the experiment. For reference, we took the positions of iodine atoms above the vacation rows, because within ±3.5 V the intensity of iodine atoms in the STM frame weakly depends on the tunnel voltage. Comparing the experimental and calculated patterns for the filled states, we see that the intensity "switching" of the images of the arsenic rows corresponding to different positions of arsenic atoms in the lattice occurs at different tunnel voltages. The switching is observed at $U_s \approx$ –(2.6–2.8) V for the experimental frames and between –0.4 and –1.5 V for the calculated STM images. Similarly, for the empty states, the corresponding transition between the observed patterns occurs at $U_s \approx$ +2.8 V and between +1.5 and +1.8 V in the calculations.

According to the tunnel spectroscopy data obtained in our experiments, the quasi-Fermi level (which automatically sets the reference point for the tunnel voltage) lies near the middle of the GaAs bandgap (1.42 eV), whereas the calculated images [3] had the top of the valence band as a reference point U_s. However, even if the thus established 0.7-V difference between the experimental and calculated U_s reference points is taken into account, the switching tunnel voltages for the same experimental and calculated images are still different. Although it might be caused by insufficient accuracy of calculation, since to take into account the effect of the local electron density in the STM tip is hardly possible, what counts here is the correspondence between experimental and calculated images.

It is seen in Fig. 4 that in STM images of filled states, iodine atoms are located in light stripes at $U_s \approx -2.3$ V and in dark stripes at $U_s \approx -3.5$ V. In addition to iodine atoms, we detected point objects designated as "G" (ghosts) in the same stripes and found that these objects changed their intensity in antiphase with the intensity of the stripes. Such objects were repeatedly observed in other works [4, 5, 15]. Their ordering under certain conditions could lead to misinterpretation of the structure—for example, as gallium clusters composed of six–eight atoms in [4, 5]. The authors of [15] tried to interpret the "ghosts" from the viewpoint of localized surface charge, but we find their case questionable. In the images of empty states (Fig. 4b), three rows of atomic objects are seen in each light stripe in both experimental frames (2.7 and 3.0 V), in which the inner row corresponds to the rows of gallium dimmers; the two outer rows, to the rows of gallium atoms in the sp^2 state [3]. Dark stripes in the images correspond to vacation rows surrounded by arsenic rows. Similar images were observed previously in [5, 7]. In the frame with $U_s = 3.0$ V, it is seen that iodine atoms (bright spots) fill dark trenches.

Let us also discuss the interpretation of experiments for the adsorption of chlorine on GaAs(001)-c(8 × 2) [8, 9] and the calculation results [11] confirming this interpretation. In [8, 9], STM images (filled states, $U_s = -3.5$ V) of the chlorinated surface were obtained ($\theta_{Cl} \approx 0.025$) in which chlorine atoms were located in dark stripes (the substrate surface was not atomically resolved). The authors of [8, 9] argued, invoking only the β2 model [10], that chlorine was adsorbed on gallium atoms, which was later theoretically substantiated in [11] within the ζ model. In Fig. 4, the dark stripes in the calculated STM images at such high tunnel voltages should correspond to arsenic rows with vacation rows inside, and the STM images that we obtained at $U_s = -3.5$ V (see Fig. 4a) also show that the rows of arsenic atoms forming arsenic rows with vacation rows inside are dark, which leads us to believe that the chlorine atoms observed in [8, 9] occupied vacation rows. The question is, why did the authors of the ζ model fail to notice the inconsistency [11]?

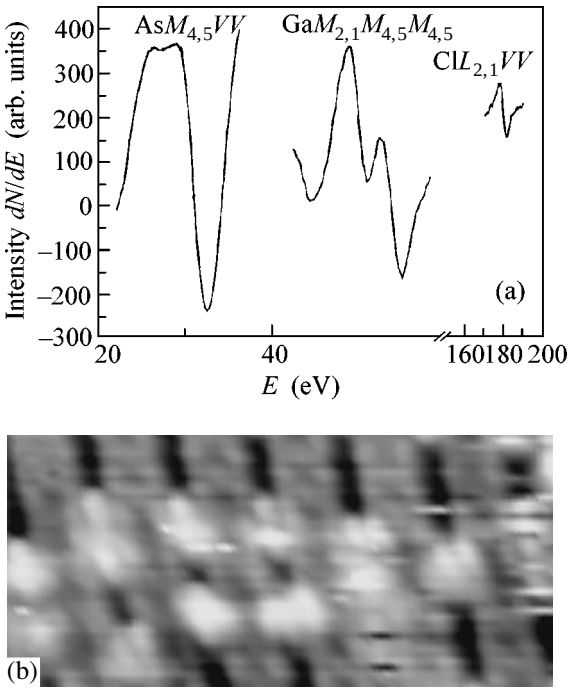

Fig. 5. (a) Auger electron spectrum and (b) STM image of the empty states of chlorinated ($\theta_{Cl} \approx 0.08$) GaAs(001)-c(8 × 2), 110 × 50 Å, $U_s = +3.5$ V, and $I_t = 0.07$ nA.

Whereas in [8, 9, 11] the suggestion that chlorine is adsorbed exactly on gallium atoms was not in doubt, photoelectron spectroscopy data of [16] demonstrated that, on the contrary, As–Cl bonds were formed at lower chlorine exposure ($D < 1.2$ L) than Ga–Cl bonds ($D = 6$ L). The sample used in [16] was gallium-rich GaAs(001)-(4 × 6) (*n*-type, Si, 1.2×10^{18} cm^{-3}), obtained by ion etching (500 eV) and annealing (580°C). We see the GaAs(001)-(4 × 6) studied in [16] as nothing but a c(8 × 2) surface reconstruction on which the ghosts ("G" objects in Fig. 4a) built a (4 × 6) superstructure [4, 5]. To confirm the conclusions made in [16], we performed special STM measurements for low coverage of GaAs(001)-c(8 × 2) by chlorine ($\theta < 0.1$, Fig. 5). At low coverage, chlorine, like iodine, occupies positions above vacation rows between arsenic atoms.

Our preliminary studies for higher surface coverage by iodine showed that the c(8 × 2) structure was destroyed at $\theta > 0.3$ and the LEED (1 × 1) pattern was diffuse. As an iodine monolayer was saturated, a surface (1 × 1)-I lattice was formed. This lattice was observed in STM as a number of small domains (50–100 Å) with distances between iodine atoms of about 4.0 Å. Chemical shifts of the Ga $M_{2,3}M_{4,5}M_{4,5}$ Auger line corresponded to the indicated structural changes on the surface. These observations do not contradict the conclusions made in [16] based on the behavior of photoelectron spectra in the process of chlorine adsorption.

Our conclusions are as follows:

1. Atomically resolved STM images of GaAs(001)-c(8 × 2) basically correspond to the ζ model of the c(8 × 2) atomic structure [3]. The asymmetry in the arrangement of the arsenic atomic rows with gallium dimers inside requires some revision of the ζ model.

2. While all the STM features calculated in [3] for the filled and empty states are observed in the STM images, the tunnel voltages at which the switching of the STM images occurs differ from the calculated ones [3].

3. At low coverage ($\theta < 0.1$) of GaAs(001)-c(8 × 2), iodine and chlorine atoms are adsorbed above vacation rows and occupy positions between arsenic atoms.

This work was supported by the Low-Dimensional Quantum Structures Program of the Presidium of the Russian Academy of Sciences, the Spin-Dependent Effects in Solids and Spintronics Program of the Section of Physical Sciences of the Russian Academy of Sciences, and partly by the Agency for Science and Innovations of the Russian Federation (contract 02.434.11.2016).

REFERENCES

1. P. R. Varecamp, M. C. Hakanson, J. Kanski, *et al.*, Phys. Rev. B **54**, 2101 (1996).
2. K. N. Eltsov, V. M. Shevlyuga, and A. A. Vedeneev, in *Proceedings of SPM-2002* (Nizhni Novgorod, 2002), p. 99.
3. S.-H. Lee, W. Moritz, and M. Scheffler, Phys. Rev. Lett. **85**, 3890 (2000).
4. Q. Xue, T. Hashizume, J. M. Zhou, *et al.*, Phys. Rev. Lett. **74**, 3177 (1995).
5. Q. Xue, T. Hashizume, and T. Sakurai, Appl. Surf. Sci. **141**, 244 (1999).
6. S. L. Scala, J. S. Hubacek, J. R. Tucker, *et al.*, Phys. Rev. B **48**, 9138 (1993).
7. H. Xu, Y. Y. Sun, Y. G. Li, *et al.*, Phys. Rev. B **70**, 081313 (2004).
8. J. G. McLean, P. Kruse, J. Guo-Ping, *et al.*, Phys. Rev. Lett. **85**, 1488 (2000).
9. J. G. McLean, P. Kruse, J. Guo-Ping, *et al.*, J. Chem. Phys. A **103**, 10364 (1999).
10. D. K. Biegelsen, R. D. Bringans, J. E. Northrup, and L.-E. Swartz, Phys. Rev. B **41**, 5701 (1990).
11. S. M. Lee, S.-H. Lee, and M. Scheffler, Phys. Rev. Lett. **89**, 239601 (2002); Phys. Rev. B **69**, 125317 (2004).
12. V. Yu. Yurov and A. N. Klimov, Rev. Sci. Instrum. **65**, 1551 (1994).
13. K. N. Eltsov, V. M. Shevlyuga, V. Yu. Yurov, *et al.*, Phys. Low-Dimens. Semicond. Struct., No. 9/10, 7 (1996).
14. *Gallium Arsenide: Production, Properties, and Application*, Ed. by F. P. Kesamanly and D. N. Nasledov (Nauka, Moscow, 1973) [in Russian].
15. P. Kruse, J. McLean, and A. C. Kummel, J. Chem. Phys. **113**, 2060 (2000).
16. W.-H. Hung, S.-L. Wu, and C.-C. Chang, J. Phys. Chem. B **102**, 1141 (1998).

Translated by the authors

JETP Letters, Vol. 82, No. 1, 2005, pp. 49–51. Translated from Pis'ma v Zhurnal Éksperimental'noĭ i Teoreticheskoĭ Fiziki, Vol. 82, No. 1, 2005, pp. 52–54.

Low-Voltage Nonstationary Electron Emission from Single-Walled Carbon Nanotubes as Exoelectron Emission

A. L. Musatov[1],* K. R. Izrael'yants[1], E. D. Obraztsova[2], S. R. Ivanova[3], and T. A. Skaballanovich[3]

[1] *Institute of Radio Engineering and Electronics, Russian Academy of Sciences, ul. Mokhovaya 11-7, Moscow, 125009 Russia*

* *e-mail: almus@mail.cplire.ru*

[2] *Natural Science Research Center, Prokhorov Institute of General Physics, Russian Academy of Sciences, Moscow, 119991 Russia*

[3] *Prokhorov Institute of General Physics, Russian Academy of Sciences, Moscow, 119991 Russia*

Received June 1, 2005

Low-voltage nonstationary electron emission from single-walled carbon nanotubes after the passage of high autoemission current has been observed. This emission is assumed to be exoelectron emission associated with mechanical stresses and defects appearing in nanotubes due to electrostatic forces acting on nanotubes in a strong electric field. © *2005 Pleiades Publishing, Inc.*

PACS numbers: 73.63.Fg, 79.70.+q, 79.75.+g

Field electron emitters based on carbon nanotubes have attracted the attention of numerous researchers due to the possibility of using them widely in vacuum electronic devices [1]. In the first approximation, the emission characteristics of such emitters are well described by the Fowler–Nordheim theory developed for metals. Deviations from this theory that are sometimes observed in the emission characteristics are attributed to adsorption states that exist at nanotube ends and increase the emission current [2].

According to the Fowler–Nordheim theory, the field electron emission current density j is related to the local electric field E near the emitter surface as

$$j \sim E^2 \exp\left(\frac{-6.8 \times 10^7 \varphi^{3/2}}{E}\right). \quad (1)$$

Here, j is measured in amperes per centimeter squared, E is measured in volts per centimeter, and φ is the emitter work function measured in electronvolts. According to Eq. (1), field electron emission is characterized by very strong dependence of the emission current on the electric field and, therefore, on the applied voltage.

Studying field electron emission from layers with single-walled carbon nanotubes, we observed the appearance of additional emission current under certain conditions, which was conserved at low voltage. As is known, the only type of emission that occurs at room temperature, low voltage, and in the absence of any additional excitations (photons, electrons, etc.) is exoelectron emission [3]. This type of emission was discovered in the 1940s by Kramer (see [3]) and is attributed to the existence of mechanical stresses and defects in solids, as well as to chemical reactions proceeding on the surfaces of solids. We believe that in our experiments we observe exoelectron emission from single-walled carbon nanotubes that is associated with mechanical stresses and defects arising in nanotubes due to electrostatic forces acting in a strong electric field.

Single-walled carbon nanotubes were synthesized by the arc method using Ni:Y_2O_3 catalyst in helium atmosphere [4]. The presence of single-walled carbon nanotubes in the synthesized material was corroborated by Raman scattering [5]. Nanotube layers were deposited by liquid electrophoresis from an alcohol suspension of nanotubes and $La(NO_3)_3$ charger. Figure 1 shows the structure of the surface of deposited films.

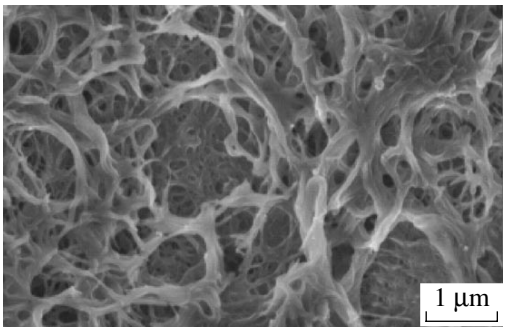

Fig. 1. Electron microscopic image of a carbon layer of single-walled nanotubes that is deposited by the liquid electrophoresis.

0021-3640/05/8201-0049$26.00

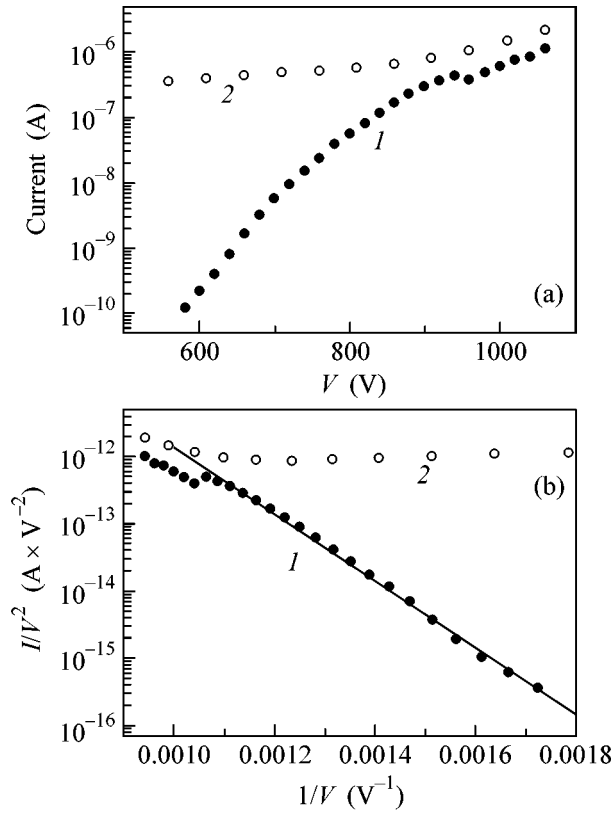

Fig. 2. (a) Current–voltage characteristics of electron emission from carbon layers with single-walled nanotubes for (*1*) an increase in the voltage and (*2*) a decrease in the voltage after a 30-min exposition in a current of $I \sim 10^{-6}$ A. (b) The same characteristics in the Fowler–Nordheim coordinates.

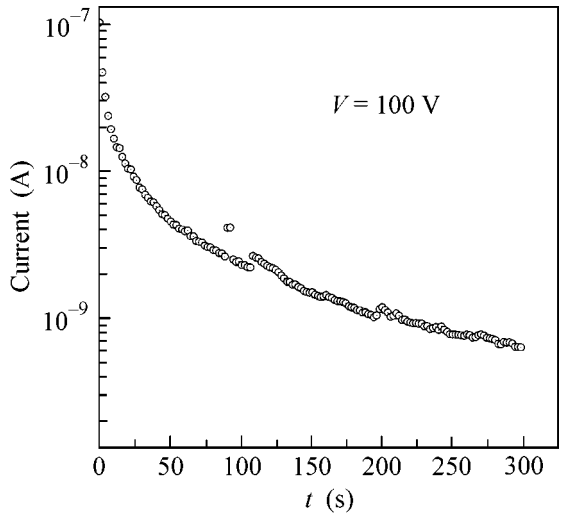

Fig. 3. Time dependence of the emission current from carbon layers with single-walled nanotubes at $V = 100$ V after 30-min exposition in a current of $I \sim 10^{-6}$ A.

Investigations of field electron emission were carried out in an ultrahigh vacuum setup at a vacuum of $p \sim 10^{-9}$ Torr. A spherical stainless steel anode 2 mm in diameter was situated at a distance of 200–400 μm from the sample surface. The sample was mounted on a universal handler. In these investigations of emission, the anode–sample distance was determined by the limb scale of the handler with respect to the handler limb at which electric contact between the anode and sample arises, i.e., when the anode touches the sample surface. Measurements of the current–voltage characteristics of field electron emission were conducted using a Keithley 248 high voltage source and a Keithley 6485 picoammeter. Emission characteristics were recorded and processed on a personal computer.

The experiment was carried out as follows. The emission current–voltage characteristics were first measured in a range of 10^{-10}–10^{-6} A as voltage between anode and sample was increased. Such a characteristic for one of the samples with single-walled carbon nanotubes is shown in Fig. 2a (points *1*). Figure 2b shows this characteristic in Fowler–Nordheim coordinates ($\log I/V^2$ vs. $1/V$). According to the Fowler–Nordheim theory, the current–voltage characteristics of field electron emission are straight lines in these coordinates. As is seen in Fig. 2b, the current–voltage characteristic measured when the voltage is increased (line *1*) in the current range $I < 4 \times 10^{-7}$ A is a straight line in the Fowler–Nordheim coordinates; i.e., field electron emission is observed. Small deviation of the characteristic from the straight line for high currents is likely attributed to a small change (blunting) in the shape of the end of the nanotube.

The sample was then exposed to an emission current of $I \sim 10^{-6}$ A for 30 min. In this case, a smooth increase in the current in time from 10^{-6} to 2×10^{-6} A was observed. Then, the current–voltage characteristic of the emission current was measured as the voltage was decreased. The voltage was decreased from 1060 to 560 V, but current decreased only from 2×10^{-6} to 3×10^{-7} A (points *2* in Fig. 2), whereas the initial current at $V = 560$ V was equal to 10^{-10} A. Moreover, even when the voltage was decreased to 100 V, the emission current first remained at a level of 10^{-7} A. Thus, we observed low-voltage electron emission from single-walled carbon nanotubes at fields that are almost an order of magnitude smaller than the field corresponding to the appearance of field electron emission of the same magnitude. We think that the observed emission is exoelectron emission and it is associated with mechanical stresses arising in single-walled carbon nanotubes due to electrostatic forces when the emission current is flowing. This emission is nonstationary and decreases rapidly in time. As is seen in Fig. 3, the emission current at $V = 100$ V decreases from 10^{-7} to 6×10^{-10} A in 5 min. A decrease in time is also characteristic of exoelectron emission.

In the strong electric field corresponding to the appearance of field electron emission, electrostatic forces act on nanotubes and extend the nanotubes to the anode [6–8]. These forces for high emission currents often lead to the break of a section of a nanotube, degradation, and a sharp decrease in the emission current [8]. To estimate the electrostatic forces applied to individual nanotubes, we use the expression

$$F = (1/2)\varepsilon_0 E^2 S, \quad (2)$$

where F is the force measured in newtons, ε_0 is the permittivity of free space measured in farads per meter, E is the electric field measured in volts per meter, and S is the area measured in meters squared. To estimate F, we calculated the force applied only to the end of the nanotube, because the electric field E is maximal near the end of the nanotube. In these calculations, we used the parameters $\varepsilon_0 = 8.85 \times 10^{12}$ F/m, $E = 3 \times 10^9$ V/m, and $S \approx 10^{-18}$ m^2 (the single-walled carbon nanotube diameter is equal to $d \approx 1$ nm) and obtained $F \approx 3 \times 10^{-11}$ N. Therefore, the mechanical stress acting in the single-walled carbon nanotube is equal to $F/S = 3 \times 10^7$ N/m^2. We believe that this mechanical stress can lead to formation of defects on the lateral surfaces of nanotubes, and these defects give rise to the appearance of exoelectrons. An additional factor responsible for the appearance of defects on surfaces of single-walled carbon nanotubes is the emission-current heating of nanotubes.

The degradation of field electron emission from carbon nanotubes is primarily determined by the break of emitting nanotubes under the action of electrostatic forces extending nanotubes to the anode [8]. Mechanical stresses likely arise in nanotubes long before the break. These stresses can lead to the appearance of exoelectron emission. We think that investigations of exoelectron emission will provide additional information on the process of nanotube degradation.

We are grateful to A.V. Garshev for scanning electron microscopy investigations. This work was supported in part by the Russian Foundation for Basic Research (project no. 04-02-17618).

REFERENCES

1. J. M. Bonard, M. Croci, C. Klinke, *et al.*, Carbon **40**, 1715 (2002).
2. K. A. Dean and B. R. Chalamala, Appl. Phys. Lett. **76**, 375 (2000).
3. É. Rabinovich, Usp. Fiz. Nauk **127**, 163 (1979).
4. E. D. Obraztsova, J.-M. Bonard, V. L. Kuznetsov, *et al.*, Nanostruct. Mater. **12**, 567 (1999).
5. A. V. Osadchiĭ, E. D. Obraztsova, S. V. Terekhov, and V. Yu. Yurov, Pis'ma Zh. Éksp. Teor. Fiz. **77**, 479 (2003) [JETP Lett. **77**, 405 (2003)].
6. A. L. Musatov, N. A. Kiselev, D. N. Zakharov, *et al.*, Appl. Surf. Sci. **183**, 111 (2001).
7. V. Semet, Vu Thien Binh, P. Vincent, *et al.*, Appl. Phys. Lett. **81**, 343 (2002).
8. Yi Wei, C. Xie, K. A. Dean, and B. F. Coll, Appl. Phys. Lett. **79**, 4527 (2001).

Translated by R. Tyapaev

JETP Letters, Vol. 82, No. 1, 2005, pp. 7–13. From Pis'ma v Zhurnal Éksperimental'noĭ i Teoreticheskoĭ Fiziki, Vol. 82, No. 1, 2005, pp. 8–14.

Moduli Integrals and Ground Ring in Minimal Liouville Gravity¶

A. A. Belavin[1] and A. B. Zamolodchikov[2]

[1] *Landau Institute for Theoretical Physics, Russian Academy of Sciences, Chernogolovka, Moscow region, 142432 Russia*

[2] *Laboratoire de Physique Théorique et Astroparticules, Université Montpelier II, Pl.E. Bataillon, 34095 Montpelier, France*

e-mail: belavin@itp.ac.ru

Received June 1, 2005

Straightforward evaluation of the correlation functions in 2D minimal gravity requires integration over the moduli space. For degenerate fields, the Liouville higher equations of motion allow one to turn the integrand to a derivative and, thus, to reduce it to the boundary terms plus a so-called curvature contribution. The last is directly related to the expectation value of the corresponding ground ring element. We use the operator product expansion technique to reproduce the ground ring construction explicitly in terms of the (generalized) minimal matter and Liouville degenerate fields. The action of the ground ring on the generic primary fields is evaluated explicitly. This permits us to directly construct the ground ring algebra. Detailed analysis of the ground ring mechanism is helpful in the understanding of the boundary terms and their evaluation. © *2005 Pleiades Publishing, Inc.*

PACS numbers: 11.25.Hf

1. INTRODUCTION

1. Liouville gravity (LG) is the term for the two-dimensional quantum gravity whose action is induced by a "critical" matter, i.e., the matter described by a conformal field theory (CFT) $\mathcal{M}_c$ with central charge c. This induced action is universal and is called the Liouville action, because its variation with respect to the metric is proportional to the Liouville (or constant curvature) equation [1]. Let us denote $\{\Phi_i, \Delta_i\}$ be the set of primary fields and their dimensions in $\mathcal{M}_c$.

2. Liouville field theory (LFT) is constructed as the quantized version of the classical theory based on the Liouville action. LFT is again a conformal field theory with central charge $c_{\rm L}$. It is convenient to parametrize it in terms of variable b or $Q = b^{-1} + b$ as

$$c_{\rm L} = 1 + 6Q^2. \tag{1}$$

Parameter b enters the local Lagrangian

$$\mathcal{L}_{\rm L} = \frac{1}{4\pi}(\partial_a\phi)^2 + \mu e^{2b\phi}, \tag{2}$$

where ϕ is the dynamical variable for the quantized metric $ds^2 = \exp(2b\phi)\hat{g}_{ab}\,dx^a dx^b$ is interpreted as the metric in isothermal coordinate system[1] and μ is a scale parameter called the cosmological constant. Basic primary fields are the exponential operators $V_a = \exp(2a\phi)$, parametrized by a continuous (in general, complex) parameter a in a way such that the corresponding conformal dimension is $\Delta_a^{(\rm L)} = a(Q-a)$. Liouville field theory is exactly solvable [2]. In particular, the three-point function $C^{(\rm L)}_{a_1,a_2,a_3} = \langle V_{a_1}(x_1)V_{a_2}(x_2)V_{a_3}(x_3)\rangle_{\rm L}$ is known explicitly for arbitrary exponential fields (see, e.g., [3]). In LG, the parameter b is chosen in such a way that, together with $\mathcal{M}_c$, LFT forms a joint conformal field theory with central charge $c + c_{\rm L} = 26$. Technically, it is also convenient to include the

3. Reparametrization ghost field theory. This is the standard fermionic BC system of spin (2, –1)

$$A_{\rm gh} = \frac{1}{\pi}\int(C\bar{\partial}B + \bar{C}\partial\bar{B})d^2x \tag{3}$$

with central charge –26, which corresponds to the gauge-fixing Faddeev–Popov determinant. The matter + the Liouville stress tensor T generates a Virasoro algebra with central charge 26. Together with the ghost field theory, this allows a BRST complex to be formed with respect to the nilpotent BRST charge

$$\mathcal{Q} = \oint(CT + C\partial CB)\frac{dz}{2\pi i}. \tag{4}$$

4. Correlation functions are some of the most important problems in the LG. In gravitational correlation functions, the matter operators Φ_i are "dressed" by

¶ This article was submitted by the authors in English.

[1] $\hat{g}_{ab}$ is the "reference metric," a technical tool needed to give LFT a covariant form.

appropriate exponential Liouville fields V_{a_i} to form either the (1, 1) form $U_i = \Phi_i V_{a_i}$ of ghost number 0 or the dimension (0, 0) operator $W_i = C\bar{C}U_i$ of ghost number 1. In both cases, this requires

$$\Delta_i + a_i(Q - a_i) = 1. \quad (5)$$

Invariant (or integrated) correlation functions are independent of any coordinates and are better called the correlation numbers. In the field-theoretic framework, a (genus 0) correlation number $\langle U_1 \ldots U_n \rangle_{\mathrm{G}}$ at $n \geq 3$ is constructed as the integral

$$\langle U_1 \ldots U_n \rangle_{\mathrm{G}} = \int\limits_{M_n} \langle W_1(x_1) \ldots W(x_n) \rangle$$
$$= \int \langle W_1(x_1) W_2(x_2) W_3(x_3) U_4(x_4) d^2x_4 \ldots U(x_n) d^2x_n \rangle. \quad (6)$$

The integration here is over the moduli space M_n of the sphere with n punctures. Technically, it is equivalent to choose any three of W_i at arbitrary fixed positions x_1, x_2, and x_3 and integrate the (1, 1) forms $U_i(x_i)d^2x_i$ inserted instead of W_i at $i = 4, \ldots, n$. At $n < 3$, the definition is slightly different. This is because of nontrivial conformal symmetries of the sphere with two and zero punctures.

The simplest case of (6) is the three-point function, where the moduli space is trivial and the result is factorized in a product of the matter, Liouville, and ghost three-point functions:

$$\langle U_1 U_2 U_3 \rangle_{\mathrm{G}} = x_{12}\bar{x}_{12}x_{23}\bar{x}_{23}x_{31}\bar{x}_{31}$$
$$\times \langle \Phi_1(x_1)\Phi_2(x_2)\Phi_3(x_3) \rangle_{\mathrm{CFT}} \langle V_1(x_1)V_2(x_2)V_3(x_3) \rangle_{\mathrm{L}}. \quad (7)$$

The three-point functions $\langle \Phi_1(x_1)\Phi_2(x_2)\Phi_3(x_3) \rangle_{\mathrm{CFT}}$, or the structure constants of the OPE algebra, are known explicitly in solvable matter CFTs. Thus, Eq. (7) gives the LG three-point function in the explicit form. The two-point function and the zero-point function (the partition sum) are simply read off from this expression of the three-point function.

5. The four-point function is the next step in the order of complexity:

$$\langle U_1 U_2 U_3 U_4 \rangle_{\mathrm{G}} = x_{12}\bar{x}_{12}x_{23}\bar{x}_{23}x_{31}\bar{x}_{31}$$
$$\times \int \langle \Phi_1(x_1) \ldots \Phi_4(x_4) \rangle_{\mathrm{CFT}} \langle V_1(x_1) \ldots V_4(x_4) \rangle_{\mathrm{L}} d^2x_4. \quad (8)$$

This expression is much less explicit. First, it involves the integration over x_4. Then, even if the matter four-point function is known in any convenient form, general representations for the Liouville four-point function are more complicated; e.g., the "conformal block" decomposition [3] involves the so-called general conformal block [4], which is by itself a complicated function of its arguments, to say nothing about the integration over the "intermediate momentum" P in [3]. In the present paper, we take a preliminary step towards the evaluation of the four-point integral in the special case of

6. Minimal gravity (MG). If the conformal matter $\mathcal{M}_c$ is represented by a minimal CFT model (more precisely, a "generalized minimal model" (GMM); see below) $\mathcal{M}_{b^2}$, we talk about the "minimal gravity" (MG) (respectively, generalized minimal gravity (GMG)). In GMG, the evaluation of the four-point integral is dramatically simplified in the case when one of the matter operators Φ_i on the right-hand side of (6) is a degenerate field $\Phi_{m,n}$. This is due to the so-called "higher equations of motion" (HEM), which hold for the operator fields in LFT [5]. If $U_4 = U_{m,n} = \Phi_{m,n}\tilde{V}_{m,n}$ ($\tilde{V}_{m,n}$ is an appropriate dressing for $\Phi_{m,n}$), HEM allows one to rewrite the integrand as a derivative and, thus, to reduce the problem to boundary terms plus the so-called curvature term. The last is directly expressed in terms of the expectation value $\langle O_{m,n}W_1W_2W_3 \rangle$ of the

7. Ground ring (GR) element $O_{m,n}$ related to the field $\Phi_{m,n}$. Therefore, we want to learn to handle the ground ring algebra and the correlation functions of its elements. This knowledge will also prove instructive in the subsequent calculations of the boundary terms.

2. GENERALIZED MINIMAL MODELS

Strictly speaking, minimal models of CFT $\mathcal{M}_{p/p'}$ [4] are consistently defined as field-theoretic constructions only if the "parameter" p/p' is an irreducible rational number, so that p and p' are coprime integers. In this case, the finite set of $(p-1)(p'-1)/2$ degenerate primary fields $\Phi_{m,n}$ with $1 \leq m < p$ and $1 \leq n < p'$ (modulo the identification $\Phi_{m,n} = \Phi_{p-m,p'-n}$) form, together with their irreducible representations, the whole space of $\mathcal{M}_{p/p'}$. "Canonical" minimal models $\mathcal{M}_{p/p'}$ are believed to be a completely consistent CFT, i.e., to satisfy all standard requirements of quantum field theory, except for unitarity. They are also considered to be exactly solvable, since the structure of their operator product expansion (OPE) algebra is known explicitly [6].

There are many ways to relax some of the requirements leading to the set of $\mathcal{M}_{p/p'}$ as unique CFT structures. For example, in the literature, the "parameter" p/p' is often taken as an arbitrary number (e.g., [6]). The algebra of the degenerate primary fields does not close any more within any finite subset; rather, the whole set $\{\Phi_{m,n}\}$ with (m, n) any natural numbers forms a closed algebra. Moreover, other authors include local fields with dimensions different from the Kac values or even a continuous spectrum of dimensions. Although the consistency of such constructions from the field-theoretic point of view remains to be clarified, these extensions prove to be a convenient technical tool. Moreover, statistical mechanics offers a number of examples where either a generalization of $\mathcal{M}_{p/p'}$ for noninteger

p/p' is essentially necessary or nondegenerate primary operators appear as observables (or both).

In this paper, we denote by b^2 the parameter p/p' and admit the notion of GMM in the widest sense as a conformal field theory with a central charge

$$c = 1 - 6(b^{-1} - b)^2 \tag{9}$$

which may involve fields Φ_α of any dimension. A continuous parameter α is introduced to parametrize a continuous family of primary fields with dimensions $\Delta_\alpha = \alpha(\alpha - q)$, where $q = b^{-1} - b$. Also, we always use the "canonical" CFT normalization of the primary fields Φ_α through the two-point functions $\langle\Phi_\alpha\Phi_\alpha\rangle_{\mathrm{GMM}} = (x\bar{x})^{-2\Delta_\alpha}$.

Degenerate fields $\Phi_{m,n}$ have dimensions $\Delta^{(\mathrm{M})}_{m,n} = -q^2/4 + \lambda^2_{m,-n}$, where a convenient notation

$$\lambda_{m,n} = mb^{-1}/2 + nb/2 \tag{10}$$

is introduced. They correspond to either $\alpha = \alpha_{m,n}$ or $\alpha = q - \alpha_{m,n}$ with $\alpha_{m,n} = q/2 + \lambda_{-m,n}$. The main restriction, which singles out this apparently loose construction, is that the

1. Degenerate fields $\Phi_{1,2}$ and $\Phi_{2,1}$ (and, therefore, in general, the whole set $\{\Phi_{m,n}\}$) are in the spectrum.

2. The null vectors in the degenerate representations $\Phi_{m,n}$ vanish

$$D^{(\mathrm{M})}_{m,n}\Phi_{m,n} = \bar{D}^{(\mathrm{M})}_{m,n}\Phi_{m,n} = 0. \tag{11}$$

Here, $D^{(\mathrm{M})}_{m,n}$ ($\bar{D}^{(\mathrm{M})}_{m,n}$) are the operators made of the right Virasoro generators M_n[2] (respectively, left $\bar{M}_n$), which create the level mn singular vector in the Virasoro module of $\Phi_{m,n}$. For definiteness, we normalize these operators through the M_{-1}^{mn} term as $D^{(\mathrm{M})}_{m,n} = M_{-1}^{mn} + \ldots$. The first examples read explicitly

$$\begin{aligned} D^{(\mathrm{M})}_{1,2} &= M_{-1}^2 - b^2 M_{-2} \\ D^{(\mathrm{M})}_{1,3} &= M_{-1}^3 - 2b^2(M_{-2}M_{-1} + M_{-1}M_{-2}) + 4b^4 M_{-3}. \end{aligned} \tag{12}$$

It turns out that this set of definitions imposes important restrictions on the structure of this formal construction. The three-point function $C_{\mathrm{M}}(\alpha_1, \alpha_2, \alpha_3) = \langle\Phi_{\alpha_1}\Phi_{\alpha_2}\Phi_{\alpha_3}\rangle_{\mathrm{GMM}}$ of "generic" primary fields can be restored uniquely from the above requirements [7]. At the degenerate values of the parameters $\alpha_i = \alpha_{m_i,n_i}$ (and if the standard "fusion" relations are satisfied), the known degenerate structure constants [6] are recovered.

[2] The unusual notations M_n for the Virasoro generators of the matter conformal symmetry are chosen to save L_n for the generators of the Liouville Virasoro.

The explicit form of the OPE of $\Phi_{1,2}$ and a generic primary field Φ_α

$$\begin{aligned} \Phi_{1,2}(x)\Phi_\alpha(0) &= C^{(\mathrm{M})}_+(\alpha)(x\bar{x})^{ab}[\Phi_{\alpha+b/2}] \\ &+ C^{(\mathrm{M})}_-(\alpha)(x\bar{x})^{1-\alpha b-b^2}[\Phi_{\alpha-b/2}] \end{aligned}$$

($[\Phi_\alpha]$ stands for a primary field Φ_α and all of its conformal descendants) will be of use below. In our normalization,

$$\begin{aligned} C^{(\mathrm{M})}_+(\alpha) &= \left[\frac{\gamma(b^2)\gamma(2\alpha b + 2b^2 - 1)}{\gamma(2b^2-1)\gamma(b^2 + 2\alpha b)}\right]^{1/2}, \\ C^{(\mathrm{M})}_-(\alpha) &= \left[\frac{\gamma(b^2)\gamma(2\alpha b + b^2 - 1)}{\gamma(2b^2-1)\gamma(2\alpha b)}\right]^{1/2}. \end{aligned} \tag{13}$$

Other exact results in GMM form a somewhat miscellaneous collection. What is important for our program is the construction of the four-point function $\langle\Phi_{m,n}(x)\Phi_{\alpha_1}(x_1)\Phi_{\alpha_2}(x_2)\Phi_{\alpha_3}(x_3)\rangle_{\mathrm{GMM}}$ with one degenerate field $\Phi_{m,n}$ and three generic primaries Φ_α [4]. Null-vector decoupling conditions (11) entail, in general, a system of partial differential equations. In the four-point case, it reads as an ordinary linear differential equation of order mn, whose independent solutions are the conformal blocks $\mathcal{F}_{r,s}(x)$ appearing in this correlation function. The four-point function is then combined as

$$\begin{aligned} G^{(\mathrm{GMM})}_{(m,n),\alpha_1,\alpha_2,\alpha_3}(x) &= \sum_{r,s}^{(m,n)} C_{\mathrm{M}}(\alpha_{m,n}, \alpha_1, \alpha_1 + \lambda_{r,-s}) \\ &\times C_{\mathrm{M}}(\alpha_1 + \lambda_{r,-s}, \alpha_2, \alpha_3)\mathcal{F}_{r,s}(x)\mathcal{F}_{r,s}(\bar{x}), \end{aligned} \tag{14}$$

where $\lambda_{r,s}$ are as in Eq. (10) and the sign $\sum_{r,s}^{(m,n)}$ stands for the sum over the following set of integers (we use the notation $\{n_1 : d : n_1 + nd\} = \{n_1, n_1 + d, \ldots, n_1 + nd\}$):

$$\begin{aligned} &(r,s) \\ &= (\{-m+1 : 2 : m-1\}, \{-n+1 : 2 : n-1\}). \end{aligned} \tag{15}$$

Presently, when considering the GMG, we restrict ourselves only to the four-point function with one degenerate matter field $\Phi_{m,n}$, leaving the other three to be formal generics Φ_α. In particular, expression (14) is the relevant construction for the matter part of the integrand in Eq. (8).

When dealing with GMM, it is important to keep in mind that there are objects of different natures. Some are continuous in the parameter b^2, like the central charge, degenerate dimensions, or certain correlation functions. Others may be highly discontinuous and dependent on the arithmetic nature of the numbers p and p'. The simplest example is the number of irreducible Virasoro representations entering into the theory. This warns us to be careful when trying to reproduce

the results of $\mathcal{M}_{p/p'}$ as a naive limit of $\mathcal{M}_{b^2}$ as $b^2 \longrightarrow p/p'$ and $\alpha \longrightarrow \alpha_{m,n}$ in the formal primary fields. This is why we stress that the three matter fields Φ_α in the matter function have generic nondegenerate values of the parameters α_1, α_2, and α_3.

3. HIGHER EQUATIONS OF MOTION

Let $a_{m,n} = Q/2 - \lambda_{m,n}$ with (m, n) as a pair of positive integers, so that $V_{m,n} = V_{a_{m,n}}$ are the Liouville exponentials corresponding to degenerate representations of the Liouville Virasoro algebra. Let also $D^{(\mathrm{L})}_{m,n}$ be the corresponding "singular vector creating" operators made of the Liouville Virasoro generators L_n, similar to the operators $D^{(\mathrm{M})}_{m,n}$ introduced above. In fact, $D^{(\mathrm{L})}_{m,n}$ is obtained from $D^{(\mathrm{M})}_{m,n}$ through the substitution $M_n \longrightarrow L_n$ and $b^2 \longrightarrow -b^2$. Like in GMM, in LFT, the corresponding singular states vanish:

$$D^{(\mathrm{L})}_{m,n} V_{m,n} = \bar{D}^{(\mathrm{L})}_{m,n} V_{m,n} = 0. \tag{16}$$

Let $D^{(\mathrm{L})}_{m,n}$ be normalized similarly to (12) as $D^{(\mathrm{L})}_{m,n} = L_{-1}^{mn} + \ldots$.

Define also the "logarithmic degenerate" fields

$$V'_{m,n} = \frac{1}{2}\frac{\partial}{\partial a} V_a\big|_{a = a_{m,n}} \tag{17}$$

for every pair (m, n) of natural numbers. These fields are not primary. Under conformal transformations $x \longrightarrow y$, they transform as

$$\begin{aligned} &|y_x|^{2\Delta_{m,n}} V'_{m,n}(y) \\ &= V'_{m,n}(x) - \Delta'_{m,n} V_{m,n}(x) \log|y_x|, \end{aligned} \tag{18}$$

where (y_x) stands for $\partial y/\partial x$. Nevertheless, as is shown in [5], $D^{(\mathrm{L})}_{m,n}\bar{D}^{(\mathrm{L})}_{m,n} V'_{m,n}$ is a primary field, and, moreover, the following identity holds for the LFT operators:

$$D^{(\mathrm{L})}_{m,n}\bar{D}^{(\mathrm{L})}_{m,n} V'_{m,n} = B_{m,n}\tilde{V}_{m,n}, \tag{19}$$

where $\tilde{V}_{m,n} = V_a\big|_{a = a_{m,-n}}$ is the Liouville exponential of dimension $\Delta^{(\mathrm{L})}_{m,n} + mn$. The numerical constant $B_{m,n}$ reads

$$B_{m,n} = \frac{(\pi\mu\gamma(b^2))^n b^{1+2n-2m\{m,n\}}}{\gamma(1-m+nb^2)} \prod_{k,l} 2\lambda_{k,l}, \tag{20}$$

where $\prod_{k,l}^{\{m,n\}}$ stands for the product over $(k, l) = (\{-m+1:1:m-1\} \otimes \{-n+1:1:n-1\})\backslash(0,0)$. It is important to observe that, in GMG, the exponential $\tilde{V}_{m,n}$ is naturally combined with the corresponding minimal matter field $\Phi_{m,n}$ to form the dressed (1, 1) form

$$U_{m,n} = \Phi_{m,n}\tilde{V}_{m,n}. \tag{21}$$

This fact makes HEM crucial for the integrability of (8) in MG.

4. GENERALIZED MINIMAL GRAVITY

Here, we quote some known results in GMG. It is repeatedly observed in the literature that, in GMG, the matter GMM parameter b coincides with that of the corresponding LFT. This is why we keep the same notation throughout this paper. For the dressed matter fields $U_a = \Phi_\alpha V_a$, Eq. (5) allows two solutions. For definiteness, let us take

$$U_a = \Phi_{a-b} V_a. \tag{22}$$

The GMG problem is to evaluate gravitational correlation functions (6) with the matter part given by the GMM expressions. Thus, in GMG we are restricted to the cases where the GMM correlation function is unambiguously determined.

The three-point function is easily calculated by multiplying $C_{\mathrm{M}}(a_1 - b, a_2 - b, a_3 - b)$ by the corresponding Liouville three-point function $C^{(\mathrm{L})}_{a_1,a_2,a_3}$. The resulting product can be written in the form

$$\langle W_{a_1} W_{a_2} W_{a_2}\rangle_{\mathrm{GMG}} = \Omega N(a_1) N(a_2) N(a_3), \tag{23}$$

where $W_a = C\bar{C}U_a$[3]

$$\Omega = [\pi\mu\gamma(b^2)]^{Q/b}[\gamma(b^2)\gamma(b^{-2}-1)b^{-2}]^{1/2} \tag{24}$$

and the "leg factors" $N(a)$ read

$$\begin{aligned} N(a) &= [\pi\mu\gamma(b^2)]^{-a/b} \\ &\times [\gamma(2ab - b^2)\gamma(2ab^{-1} - b^{-2})]^{1/2}. \end{aligned} \tag{25}$$

The two-point function $\langle U_a U_a\rangle_{\mathrm{GMG}}$ and the partition sum Z_{L} can be restored from this expression as

$$\langle U_a U_a\rangle_{\mathrm{GMG}} = [\pi\mu\gamma(b^2)]^{Q/b}\frac{N^2(a)}{\pi(2a-Q)} \tag{26}$$

and

$$Z_{\mathrm{L}} = [\pi\mu\gamma(b^2)]^{Q/b}\frac{1-b^2}{\pi^3 Q\gamma(b^2)\gamma(b^{-2})}. \tag{27}$$

For the normalized correlation functions $\langle\langle W_{a_1} W_{a_2} W_{a_2}\rangle\rangle = Z_{\mathrm{L}}^{-1}\langle W_{a_1} W_{a_2} W_{a_2}\rangle_{\mathrm{GMG}}$ and

[3] Later on, we will use sometimes less compact notations $U(a) = U_a$ and $W(a) = W_a$.

$\langle\langle U_a U_a\rangle\rangle = Z_{\rm L}^{-1}\langle U_a U_a\rangle_{\rm GMG}$, it is convenient to use slightly different leg factors

$$\mathcal{N}(a) = \pi N(a)\left[\frac{\gamma(b^2)\gamma(b^{-2})}{-(b^{-2}-1)^2}\right]^{1/2}, \quad (28)$$

so that

$$\langle\langle W_{a_1} W_{a_2} W_{a_2}\rangle\rangle = (1+b^{-2})b^{-2}(b^{-2}-1)\prod_{i=1}^{3}\mathcal{N}(a_i),$$
$$\langle\langle U_a U_a\rangle\rangle = \frac{(b^{-2}+1)b^{-2}(b^{-2}-1)}{(2ab^{-1}-b^{-2}-1)}\mathcal{N}^2(a). \quad (29)$$

At the generic values of a, it will prove convenient to define renormalized fields

$$\mathcal{U}(a) = \mathcal{N}^{-1}(a)U_a; \quad \mathcal{W}(a) = \mathcal{N}^{-1}(a)W_a, \quad (30)$$

for which (29) is reduced to

$$\langle\langle \mathcal{U}(a)\mathcal{U}(a)\rangle\rangle = \frac{(g+1)g(g-1)}{(2s-g-1)},$$
$$\langle\langle \mathcal{W}(a_1)\mathcal{W}(a_2)\mathcal{W}(a_3)\rangle\rangle = (g+1)g(g-1), \quad (31)$$

where $g = b^{-2}$ and $s = ab^{-1}$. It is readily verified that, formally, $\mathcal{W}(a) = \mathcal{W}(Q-a)$; i.e., in this normalization, the dressed matter operators are independent of the choice of the dressing. This might seem an important advantage. The price to pay is that leg factors (25) are sometimes singular and, in any case, depend on the cosmological constant μ.

5. DISCRETE STATES AND THE FOUR-POINT INTEGRAL

The next level of difficulty is the four-point correlation number $\langle U_{a_1} U_{a_2} U_{a_3} U_{a_4}\rangle_{\rm GMG}$ given by integral (8). If one of the four matter operators, e.g., $\Phi_{\alpha_4} = \Phi_{m,n}$, the matter four-point function is constructed through (14). Let the remaining three fields stay generic formal primaries of GMM.[4] Our purpose is to evaluate the integral

$$\langle U_{m,n} U_{a_1} U_{a_2} U_{a_3}\rangle_{\rm GMG} = \int\langle U_{m,n}(x) W_{a_1}(x_1) W_{a_2}(x_2) W_{a_3}(x_3)\rangle d^2x, \quad (32)$$

where $U_{m,n}$ is the dressed degenerate field $\Phi_{m,n}$ defined in (21). We denote by

$$\Theta_{m,n} = \Phi_{m,n} V_{m,n} \quad (33)$$

the direct product of the matter and Liouville degenerate fields and introduce the operators

$$\mathcal{D}_{m,n} = D^{(\rm M)}_{m,n} + (-)^{mn} D^{(\rm L)}_{m,n} \quad (34)$$

(and, similarly, $\bar{\mathcal{D}}_{m,n}$), where $D^{(\rm M)}_{m,n}$ and $D^{(\rm L)}_{m,n}$ are the matter and Liouville "singular vector creating" operators introduced above.

Proposition 1. For every pair (m, n) of positive integers, there exists an operator $H_{m,n}$ made of the Virasoro generators M_n, L_n and the ghost fields B and C as a graded polynomial of order $mn-1$ and ghost number 0, such that $H_{m,n}\Theta_{m,n}$ is closed but nontrivial. Operator $H_{m,n}$ is unique modulo exact terms.

Statement 1 can be verified by explicit calculations on the first levels. One finds

$$H_{1,2} = M_{-1} - L_{-1} + b^2 CB,$$
$$H_{1,3} = M_{-1}^2 - M_{-1}L_{-1} + L_{-1}^2 - 2b^2(M_{-2}+L_{-2}) + 2b^2(M_{-1}-L_{-1})CB - 4b^4 C\partial B. \quad (35)$$

For the series $(1, n)$, a proof is given in [8]. At general (m, n), the statement is most certainly also true (B. Feigin, private communication). Cohomology classes of $H_{m,n}\Theta_{m,n}$ were discovered in [9, 10] and are called the "discrete states." Although the generic form of the operators $H_{m,n}$ is not known to us, the normalization is supposed to be fixed as $H_{m,n} = \sum_{k=0}^{mn-1}(M_{-1})^{mn-1-k}(-L_{-1})^k + \ldots$. Apparently,

$$(\partial H_{m,n} - \mathcal{Q}R_{m,n})\Theta_{m,n} = (\bar\partial\bar H_{m,n} - \bar{\mathcal{Q}}\bar R_{m,n})\Theta_{m,n} = 0, \quad (36)$$

where $R_{m,n}$ is again a graded polynomial in M_n, L_n, and ghosts.

Proposition 2.

$$\mathcal{D}_{m,n}\bar{\mathcal{D}}_{m,n}\Theta'_{m,n} = (\partial H_{m,n} - \mathcal{Q}R_{m,n})(\bar\partial\bar H_{m,n} - \bar{\mathcal{Q}}\bar R_{m,n})\Theta'_{m,n}, \quad (37)$$

where $\Theta'_{m,n} = \Phi_{m,n}V'_{m,n}$ and $V'_{m,n}$ is from Eq. (17).

We verified Statement 2 directly for $(m, n) = (1, 2)$ and $(1, 3)$. Thus, general case might require modifications. Combined with HEM (19), it permits us to replace Eq. (32) by

$$B^{-1}_{m,n}\int\partial\bar\partial\langle O'_{m,n}(x) W_{a_1}(x_1) W_{a_2}(x_2) W_{a_3}(x_3)\rangle d^2x, \quad (38)$$

where $O'_{m,n} = H_{m,n}\bar H_{m,n}\Theta'_{m,n}$. This is, hence, reduced to the boundary integral and the so-called curvature contribution. The boundary consists of small circles $\partial\Gamma_i$ around the W insertions. To evaluate the boundary terms, we need to understand better the short-distance

[4] As we will discuss at the end of the paper, the last requirement is essential, because sometimes correlation functions with degenerate fields are not straightforward limits of those with generic ones with the appropriate specialization of the parameter.

behavior of the operator product $O'_{m,n}(x)W_a(x_1)$. Presently, we discuss only the curvature term.

6. CURVATURE TERM

The curvature term comes from the fact that the operator $O'_{m,n}$ is not exactly a scalar ((0, 0) form) but rather a logarithmic field. Under conformal coordinate transformations $x \longrightarrow y$, it acquires an inhomogeneous part

$$O'_{m,n}(y) = O'_{m,n}(x) - \Delta'_{m,n}O_{m,n}(x)\log|y_x|, \qquad (39)$$

where

$$O_{m,n} = H_{m,n}\bar{H}_{m,n}\Theta_{m,n} \qquad (40)$$

is the ground ring element (see below) and

$$\Delta'_{m,n} = \frac{d}{da}\Delta_a^{(\mathrm{L})}\Big|_{a=a_{m,n}} = mb^{-1} + nb. \qquad (41)$$

This subtlety can be treated in two ways. First, it is easy to show that, on the sphere, transformation (39) leads to the following behavior of the correlation function with $O'_{m,n}(x)$ at $x \longrightarrow \infty$:

$$\langle O'_{m,n}(x)W_{a_1}(x_1)W_{a_2}(x_2)W_{a_3}(x_3)\rangle$$
$$\sim -\Delta'_{m,n}\log(x\bar{x})\langle O_{m,n}W_{a_1}W_{a_2}W_{a_3}\rangle.$$

Therefore, the curvature contribution can be included as a boundary term $\partial\Gamma_\infty$ at ∞. It is evaluated as

$$\frac{1}{2i}\int_{\partial\Gamma_\infty}\partial\langle O'_{m,n}(x)W_{a_1}(x_1)W_{a_2}(x_2)W_{a_3}(x_3)\rangle dx \qquad (42)$$
$$= \pi\Delta'_{m,n}\langle O_{m,n}W_{a_1}W_{a_2}W_{a_3}\rangle.$$

Another trick, which is more easily generalized for more complicated surfaces, is to keep track of the background metric $\hat{g}_{ab} = e^{\sigma}\delta_{ab}$. Since the scale factor $\sigma(x)$ transforms as

$$\sigma(y) = \sigma(x) - 2\log|y_x|$$

under conformal maps, the combination

$$\tilde{O}'_{m,n}(x) = O'_{m,n}(x) - \Delta'_{m,n}\sigma(x)O_{m,n}(x)/2 \qquad (43)$$

is a scalar (the dependence on the background metric is the price to pay). Thus, in the BRST invariant environment, Eq. (37) can be rewritten as

$$B_{m,n}U_{m,n} = \sqrt{\hat{g}}\left(\frac{1}{4}\hat{\Delta}\tilde{O}'_{m,n} - \frac{\Delta'_{m,n}}{8}\hat{R}O_{m,n}\right) + \text{exact},$$

where $\hat{\Delta}$ is the covariant Laplace operator with respect to $\hat{g}_{ab}$ and $\hat{R}$ is the corresponding scalar curvature. On a sphere, the contribution of the second term apparently reduces to (42).

At this step, it is clear that better understanding of the ground ring structure in GMG, in particular, the evaluation of the expectation value in the right-hand side of Eq. (42), is of importance in the program.

7. GROUND RING IN GMG

It has been discovered in [9, 10] that, in MG, the degenerate fields $\Phi_{m,n}$ of GMM, when combined with the degenerate exponentials $V_{m,n}$ of the corresponding LFT, give rise to nontrivial BRST closed operators (40) with ghost number 0 and conformal dimension (0, 0). Some of these operators were evaluated explicitly in [8]. The spatial derivatives $\partial O_{m,n}$ and $\bar{\partial}O_{m,n}$ are exact (Eq. (36)), and, therefore, the correlation functions of these discrete states in the BRST closed environment do not depend on their positions. Moreover, as the BRST cohomology classes, they form a closed ring under an operator product expansion called the ground ring. This observation led Witten [10] to conclude that this structure plays a crucial role in the structure of MG, and, probably, the whole algebraic structure of the theory is in fact that of the ground ring. In this section, we present few explicit calculations revealing the GR properties. Cohomology properties of $O_{m,n}$ are relevant only in a $\mathfrak{Q}$-invariant environment. The simplest invariant state on a sphere is created by three operators W_a. For this reason, we perform the actual calculation of the correlation function of $\langle O_{m,n}W_{a_1}W_{a_2}W_{a_3}\rangle$ on a sphere with three generic W_a insertions.

Modulo exact forms of the discrete states $O_{m,n}$ act in the space of classes W_a. This is because their action does not change the ghost number and, generically, all nontrivial classes are exhausted by the composite fields W_a with different a. Moreover, due to the decoupling restrictions in the OPE of the degenerate fields $\Phi_{m,n}$ and $V_{m,n}$ with the primaries Φ_α and V_a, respectively, the general structure of the operator product $O_{m,n}(x)W(a)$ is doomed to have the form

$$O_{m,n}W(a) = \sum_{r,s}^{(m,n)} A_{r,s}^{(m,n)}W(a + \lambda_{r,s}) + \text{exact}, \qquad (44)$$

with some numerical coefficients $A_{r,s}^{(m,n)}$. Our first aim is to evaluate them.

It is instructive to perform explicit calculations in the simplest case $(m, n) = (1, 2)$. The special operator product expansions we need in this case are (13) and

$$V_{1,2}(y)V_a(0) = C_+^{(\mathrm{L})}(a)(y\bar{y})^{ab}[V_{a-b/2}]$$
$$+ C_-^{(\mathrm{L})}(a)(y\bar{y})^{1-ab+b^2}[V_{a+b/2}],$$

where

$$C_+^{(\mathrm{L})}(a) = 1;$$

$$C_-^{(\mathrm{L})}(a) = -\frac{\pi\mu}{\gamma(-b^2)}\frac{\gamma(2ab-b^2-1)}{\gamma(2ab)}.$$

It is easy to verify by explicit calculation (at least at the primary field level) that, in the product $U_a = \Phi_{a-b}V_a$, the action of $H_{1,2}$ and $\bar{H}_{1,2}$ eliminates the "wrong terms" with the combinations $\Phi_{a-b/2}V_{a-b/2}$ and $\Phi_{a-3b/2}V_{a+b/2}$, and we are left with

$$\begin{aligned} O_{1,2}W(a) &= A_{0,-1}^{(1,2)}W(a-b/2) \\ &+ A_{0,1}^{(1,2)}W(a+b/2) + \text{exact}, \end{aligned} \tag{45}$$

with

$$\begin{aligned} A_{0,-1}^{(1,2)} &= (1-2ab+b^2)^2 C_-^{(\mathrm{M})}(a-b)C_+^{(\mathrm{L})}(a), \\ A_{0,1}^{(1,2)} &= (1-2ab+b^2)^2 C_+^{(\mathrm{M})}(a-b)C_-^{(\mathrm{L})}(a). \end{aligned} \tag{46}$$

The polynomial multipliers in the coefficients are the result of the action of $H_{1,2}$ on the corresponding terms in the expansion of $\Theta_{1,2}(x)W_a(0)$. A similar calculation can be directly performed for the action of every $\Phi_{m,n}$. We calculated these polynomials also for the case $(m, n) = (1, 3)$ and verified that the result is summarized as follows:

$$N(a+\lambda_{r,s})A_{r,s}^{(m,n)} = \Lambda_{m,n}N(a), \tag{47}$$

where

$$\Lambda_{m,n} = (\gamma(b^2)\gamma(b^{-2})(b-b^{-1})^{-2})^{1/2}B_{m,n}N(a_{m,-n}) \tag{48}$$

and $B_{m,n}$ are the same as in Eq. (20).

It seems tempting to simplify these relations by introducing the renormalized fields $\mathcal{W}(a)$ as in Eq. (30) and $\mathbb{O}_{m,n} = \Lambda_{m,n}^{-1}O_{m,n}$, so that (44) is reduced to

$$\mathbb{O}_{m,n}\mathcal{W}(a) = \sum_{r,s}^{(m,n)}\mathcal{W}(a+\Lambda_{r,s}). \tag{49}$$

8. DISCUSSION

This is basically what has been figured out previously on the basis of more general arguments [11]. Here, we arrive at this expression by a direct calculation. Another important difference is that we considered the action of $O_{m,n}$ on a cohomology W_a with generic a. It is natural to expect that relations (49) are modified when specialized to the degenerate fields $W_{m,n} = C\bar{C}\Phi_{m,n}\tilde{V}_{m,n}$ with a vanishing null vector in the degenerate matter sector. Although the effect most probably might be simply the proper truncation of the sum in Eq. (49) implied by the fusion algebra of the degenerate fields, technically the limit $a \longrightarrow a_{m,-n}$ in this expression turns out to be subtle and requires a more careful analysis. Therefore, in this article, we restrict ourselves with the case of generic values of a, leaving the degenerate cases for further study. This is basically sufficient for our subsequent treatment of integral (32) with generic nondegenerate values of a_1, a_2, and a_3.

Simple action (49) naturally implies the following structure of the ground ring algebra:

$$\mathbb{O}_{m,n}\mathbb{O}_{m',n'} = \sum_{l}^{[m,m'][n,n']}\sum_{k}\mathbb{O}_{l,k}, \tag{50}$$

where the symbol $\sum_k^{[n,n']}$ implies the sum over $k = \{\min(|n-n'|, 0) : 2 : n+n'\}$. Or, if you prefer to follow [11] and introduce $X = \mathbb{O}_{1,2}/2$ and $Y = \mathbb{O}_{2,1}/2$,

$$\mathbb{O}_{m,n} = U_{m-1}(Y)U_{n-1}(X), \tag{51}$$

where $U_n(x)$ are the Chebyshev polynomials of the second kind.

We are grateful to B. Feigin, I. Kostov, A. Litvinov, V. Petkova, and A. Zamolodchikov for useful discussions. Our collaboration was supported by INTAS (grant no. INTAS-OPEN-03-51-3350). A.B. was supported by the Russian Foundation for Basic Research (project no. 04-02-16027) and by the Spanish Ministerio de Educasion y Ciencia (project no. BFM 2002-03610). A.Z. acknowledges the hospitality and stimulating scientific atmosphere of the Theoretical Physics Laboratory at RIKEN, where the work was finished. His efforts are supported also by the European Committee under contract no. EUCLID HRPN-CT-2002-00325.

REFERENCES

1. A. Polyakov, Phys. Lett. B **103B**, 207 (1981).
2. H. Dorn and H.-J. Otto, Phys. Lett. B **291**, 39 (1992); Nucl. Phys. B **429**, 375 (1994).
3. A. Zamolodchikov and Al. Zamolodchikov, Nucl. Phys. B **477**, 577 (1996).
4. A. Belavin, A. Polyakov, and A. Zamolodchikov, Nucl. Phys. B **241**, 333 (1984).
5. Al. Zamolodchikov, Int. J. Mod. Phys. A **19S2**, 510 (2004).
6. V. Dotsenko and V. Fateev, Phys. Lett. B **154B**, 291 (1985).
7. Al. Zamolodchikov, Theor. Math. Phys. **142**, 183 (2005).
8. C. Imbimbo, S. Mahapatra, and S. Mukhi, Nucl. Phys. B **375**, 399 (1992).
9. I. Klebanov and A. Polyakov, Mod. Phys. Lett. A **6**, 3273 (1991).
10. E. Witten, Nucl. Phys. B **373**, 187 (1992).
11. N. Seiberg and D. Shih, J. High Energy Phys. **0402**, 021 (2004).